The modeling of a cold storage with metal foam enhanced phase change material.

André Paulsen

Supervisor: Prof. dr. ir. Michel De Paepe
Counsellors: Ir. Wim Beyne, Dr. Özer Bagci

Master's dissertation submitted in order to obtain the academic degree of
Master of Science in Electromechanical Engineering

Vakgroep Mechanica van Stroming, Warmte en Verbranding
Chair: Prof. dr. ir. Jan Vierendeels
Faculty of Engineering and Architecture
Academic year 2017-2018

GHENT
UNIVERSITY

The modeling of a cold storage with metal foam enhanced phase change material.

André Paulsen

Supervisor: Prof. dr. ir. Michel De Paepe
Counsellors: Ir. Wim Beyne, Dr. Özer Bagci

Master's dissertation submitted in order to obtain the academic degree of
Master of Science in Electromechanical Engineering

Vakgroep Mechanica van Stroming, Warmte en Verbranding
Chair: Prof. dr. ir. Jan Vierendeels
Faculty of Engineering and Architecture
Academic year 2017-2018

Acknowledgements

First of all I would like to thank prof. dr. ir. Michel De Paepe for giving me the opportunity of writing this thesis wihtin his research group. Further thanks go out to my supervisor ir. Wim Beyne for his guidance, useful comments and encouragement. A completed book would not have been possible without him.

I would also like to thank my girlfriend for putting up with my moodiness these last few weeks.

Lastly, I would like to express my gratitude to my parents for their moral and financial support throughout my studies.

Ghent, June 2018 André Paulsen

MASTER THESIS 2017-2018
Research group Applied Thermodynamics and Heat Transfer
Department of Flow, Heat and Combustion Mechanics - UGent
Paper number: AP

THE MODELLING OF A COLD STORAGE WITH METAL FOAM ENHANCED PHASE CHANGE MATERIAL

André Paulsen, Ir. Wim Beyne, Dr. Özer Bagci, Prof. dr. ir. Michel De Paepe
Department of Flow, Heat and Combustion Mechanics
Ghent University
Sint-Pietersnieuwstraat 41 – B9000 Gent – Belgium
E-mail: bengt.paulsen@ugent.be

ABSTRACT

The charging of a cold storage with metal foam enhanced PCM is modelled with an enthalpy-based method in this study. The metal foam enhanced PCM is modelled by a one-temperature model, where PCM and foam are assumed to be in thermal equilibrium. The effects of the metal foam on the heat transfer rate is implemented by the calculation of an increased thermal conductivity.

The numerically calculated results are compared with experimental data. Similar trends are observed, but they are less pronounced in the numerical calculations. This is appointed to an exclusion of the aluminum profile of the thermal battery in the model. The influence of the aluminum sensitive heat cannot be neglected, especially in the early stages of charging.

The one-temperature model with an increased effective thermal conductivity results overestimates the charging effectivity since the contact resistance between wall and metal foam is not modelled.

NOMENCLATURE

a	[-]	Discretization parameter
b	[-]	Discretization parameter
c	[J/kgK]	Specific heat capacity
d_{pcm}	[m]	Distance to phase change front
f	[-]	Liquid fraction
H	[J/m^3]	Total volumetric enthalpy
k	[W/mK]	Thermal conductivity
m	[kg]	Mass
$\dot{m}$	[kg/s]	Mass flow rate
Q	[J]	Heat stored
q	[W]	Heat transfer rate
R	[m^{2}K/W]	Thermal resistance
T	[K]	Temperature
t	[s]	Time
Special characters		
ρ	[kg/m^3]	Density
Δh_m	[J/kg]	Latent heat of fusion
Subscripts		
$conv$		Convective
eff		Effective
f		Foam
in		Inlet
pcm		Phase change material
htf		Heat transfer fluid
l		Liquid
max		Maximum
nb		Neighboring point
out		Outlet
p		Node point
$prev$		Previous
ref		Reference
s		Solid
tot		Total
Supscripts		
old		Old value

INTRODUCTION

Cold storage and cold transport is amongst other used in the food and pharmaceutical industry. A predetermined temperature range needs to be maintained to avoid product waste. Maintaining this cold chain requires energy. It is estimated that the cold chain is responsible for 2.5% of the global greenhouse gas [1]. Improvements in this field has thus positive environmental implications.

An active cooling system can be used to maintain the predetermined temperature range by adding a refrigerating cycle to the transport. Mobile active coolers however comes with some disadvantages. The weight and dimension requirements results in a lower efficiency compared to their stationary counter parts. They also need a constant power supply and regular maintenance.

The use of a passive cooling system can be advantageous during transport, which is done by placing a pre-chilled mass in an insulated container. The absence of an active cooler makes it cheaper, lighter and vibration free. The temperature can however not be controlled actively. The pre-chilled mass will absorb the heat entering the container to maintain the desired temperature.

The main disadvantage of a passive cooling system is that it needs to be chilled prior to each transport and cannot operate continuously. A material is needed that can absorb heat during the entire shipment and be charged effectively.

Two widely used techniques for thermal energy storage are sensible and latent energy storage. Sensible heat is stored by changing the temperature of a material from an initial temperature T_{init} to a final one T_f. The sensible heat is then expressed using the specific heat capacity c and the mass m of the material [2].

$$Q = \int_{T_{init}}^{T_f} \rho c dT \tag{1}$$

Energy is also stored or released during the phase change of a material. This is referred to as latent heat. An extra term is added to incorporate this. The latent heat is defined the mass m, the melted fraction a_m and the latent heat of fusion Δh_m [2].

$$Q = \int_{T_{init}}^{T_m} mcdT + ma_m\Delta h_m + \int_{T_{init}}^{T_m} mcdT \tag{2}$$

Latent thermal energy offers a high density storage at a nearly constant temperature, which is the phase change temperature of the material. Latent thermal storage density is 5 to 14 times higher than for sensitive storage energy [3].

Phase change materials (PCM) are used for latent thermal energy storage. They are divided into three groups: organic, inorganic and eutectic [4]. PCMs have a high latent heat of fusion (125 – 400 MJ/m^3), which offers the possibility to achieve high energy storage density. They however have a low thermal conductivity (0.1 – 0.6 W/mK). This leads to a low heat transfer rate during the charging and discharging process.

Several methods can be used to achieve a conductivity enhancement. An example is by enhancing the PCM with an open cell metal foam. This is material with a high conductivity, a high surface to volume ratio and a high porosity. This makes it an effective way to increase the heat transfer in PCMs [5].

The subject of this study is to model a cold storage with metal foam enhanced phase change material.

LITERATURE SURVEY

Studying cold storages numerically has the advantages that various conditions can be simulated by changing the variables in the model [6].

A material undergoing a phase transition has a moving phase change front. The non-linear nature of the phase change at the transition front and the different thermos-physical properties of the phases makes it difficult to predict the behavior of the phase change [7].

Analytical models can be used to make a first order approximation. A way of formulating this moving boundary problem is called the Stefan problem [8]. This however only models the latent heat. Inclusion of the sensible heat offers a better representation of the process and can be done using numerical models.

A numerical enthalpy-based method can be used by considering a one-dimensional phase transformation controlled by heat conduction k. The energy conservation can be expressed using the total volumetric enthalpy H as function of temperature. An isothermal phase change can be expressed using following equation [9]

$$\frac{\partial H}{\partial t} = \nabla[k(\nabla T)] \tag{3}$$

The total volumetric enthalpy consists of the sensible and latent heat of the PCM.

$$H = \int_{T_{ref}}^{T} \rho c dT + \rho_l f \Delta h_m \tag{4}$$

The sensible heat h is obtained by changing the temperature of the PCM (Equation (1)). The latent heat is as a function of the latent heat of fusion Δh_m the liquid density ρ_l and the liquid fraction f.

The liquid fraction is 0 to 1. The solid and liquid states correspond to the lower and upper value, respectively. A mushy state is present in between.

A second numerical method is the effective heat capacity method. The latent heat is modelled by assuming a large heat capacity in the melting range ($T_s - T_l$) [10]. This effective heat capacity c is a function of the latent heat of fusion, the difference between liquid and solid temperature and the solid specific heat capacity. This results in following equation.

$$c_{eff} = \frac{\Delta h_m}{T_l - T_s} + c_s \tag{5}$$

This energy conservation can then be expressed as a function of temperature.

$$\rho c_{eff} \frac{\partial T}{\partial t} = \nabla[k(\nabla T)] \tag{6}$$

Both the enthalpy and effective heat capacity method can be used to model the phase change. They however have some disadvantages. The enthalpy method has problems with super-cooling and temperature oscillations. On the other hand, the effective heat capacity method is difficult to use for small phase change temperature ranges and cannot be applied for a fixed phase change temperature [6].

There will be buoyancy effects present during the phase in the liquid PCM. This is especially the case for the melting process, due to a larger temperature gradient between the transition front and the heat transfer fluid (HTF). This temperature gradient is small during the solidification process since the solid PCM is situated farther away from the HTF. The effects of natural convection in the liquid PCM can thus be neglected during the solidification process [11].

Introducing an open cell metal foam in the PCM, increases the effective thermal conductivity of the compound. Two materials with different thermos-physical properties are now however present, which makes the modelling more difficult.

A local thermal non-equilibrium will be present between foam and PCM. This can be modelled using a two-temperature model [12]. Two energy conservation equations are needed and an interstitial heat transfer coefficient between the two materials is needed to couple their equations.

A simpler way to model a metal foam enhanced PCM is by the use of a one-temperature model [12]. The metal foam and PCM are considered as a homogeneous material with an equal temperature. A single energy conservation equation can thus describe the problem.

An effective conductivity however needs to be calculated, which is defined by the conductivity of the PCM k_{pcm}, the conductivity of the foam k_f and the foam porosity γ. A first order approximation is possible

$$k_{eff} = \gamma k_f + (1-\gamma) k_{pcm} \tag{7}$$

This first order approximation however overestimates the effective conductivity [12]. Boomsma and Poulikos [13] presented a correlation based on a three-dimensionally structured model of the foam, which is a better estimate.

THERMAL BATTERY

The goal of this study is to model a cold storage with metal foam enhanced PCM. Two thermal batteries were constructed and experimentally investigated by Corryn [14]. One battery was enhanced with metal foam. These batteries will be modelled to allow comparison with the experimental data.

A schematic of the battery can be seen in Figure 1. It consists of four aluminum profiles with lengths of 806 mm. They are placed next to each other and welded together. HTF flows through the battery to charge it. Collectors are added at the extremities to connect them in series and guide the HTF flow to the downstream profiles.

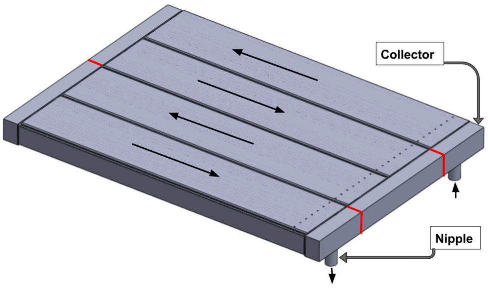

Figure 1 Schematic of thermal battery [14]

The cross-section of the profiles is illustrated in Figure 2. Two types of channels are present. The open B channels which allow through flow of the HTF. The charging is done by cooling the PCM enclosed in the A channels. The enhanced PCM is obtained by adding open cell aluminium metal pieces in the A channels of one battery. The aluminium foam is produced by Alhedron and has a porosity of 93%. The A and B channels have dimensions of 50 x 10 mm^2 and 50 x 8.3 mm^2.

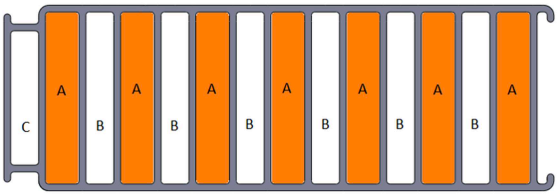

Figure 2 Schematic of thermal battery [14]

The used HTF fluid is TEMPER -30 by Climalife and the organic RT5HC PCM by Rubitherm is used. Temperature measurements are performed inside the PCM of the four profiles. The inlet and outlet temperature of the HTF is also measured.

MODEL GEOMETRY

The geometry of the thermal battery is simplified to perform the numerical calculations. The aluminium profiles have six HTF channels and seven PCM channels (Figure 2). First an assumption about the HTF flow distribution is made. An even flow distribution over the channels considered. Secondly, a symmetrical heat transfer process is presumed. This makes it possible to model the phase change process in one profile by modelling one half PCM channel and one half HTF channel.

The thermal battery consists of four profiles connected by collector bends (Figure 1). These collectors are neglected and the entire thermal battery is modelled as four channels placed in-line after each other.

ENTHALPY MODEL

The enthalpy model expresses the energy conservation as a function of total volumetric enthalpy and temperature (Equation (3)). The model geometry is discretized to form a two-dimensional grid (Figure 3). Applying the conservation of energy on the control volumes of this will result in a system of equations which is solved for each time step using a numerical scheme.

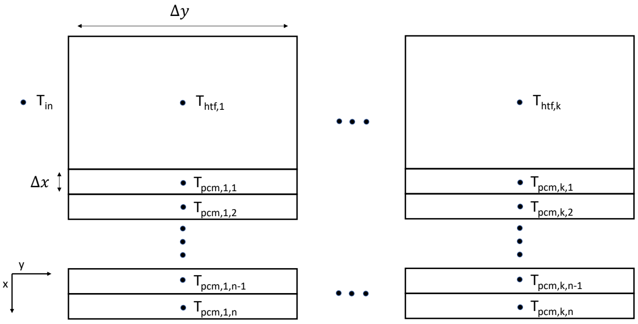

Figure 3 Schematic of control volumes.

Generic PCM control volumes

The phase change problem is governed by the conduction in the PCM. The effects of natural convection in the liquid PCM are neglected. The PCM is assumed to have a constant specific heat capacity and density. By substituting Equation (4) in Equation (3) the conservation of energy is expressed as a function of temperature [15]. The reference temperature T_{ref} is set to 0 K and equal thermo-physical properties of the liquid and solid PCM are assumed. The heat transfer in the PCM in the flow direction (y-direction) is neglected. This results in following one-dimensional energy conservation.

$$\rho c \frac{\partial T}{\partial x} = \frac{\partial}{\partial x}\left(k \frac{\partial T}{\partial x}\right) - \rho \Delta h_m \frac{\partial f}{\partial t} \tag{8}$$

The above equation is discretized using a fully implicit finite volume method by integrating over each control volume. This results in following point form.

$$a_p T_p = \textstyle\sum_{nb} a_{nb} T_{nb} + b_p T_p^{old} + V \rho \Delta h_m (f_p^{old} - f_{p)}$$

$$a_{nb} = \frac{A\,k}{\Delta x},\ b_p = \frac{V\,\rho\,c}{\Delta t},\ a_p = \textstyle\sum_{nb} a_{nb} + b_p \tag{9}$$

The temperature of a node point T_p is expressed as a function of its old value $T_p{}^{old}$, its liquid fraction f_p and its old liquid fraction f_p^{old} and the temperatures of the neighboring points T_{nb}. The discretization parameters a_{nb}, a_p and b_p are determined by the heat transferring area A between CVs, the volume V of the CVs, the thermal conductivity k of the PCM and the dimension in the x-direction Δx of the CVs.

The phase change occurs in a temperature range between 5 °C and 6 °C. A mushy zone is present in this range with a liquid fraction f between 1 and 0. This liquid fraction is written as a linear function of temperature.

$$f(T) = \frac{T - T_s}{T_l - T_s} \qquad (10)$$

In order to have a correct representation of the phase change problem an appropriate liquid fraction update in the mushy zone is necessary. The source-based method of Voller and Swaminathan [16] is used.

Heat transfer fluid control volumes

The HTF flow is assumed to be inviscid, incompressible and one-dimensional. This makes it possible to decouple the equations of motion from the energy equations. The momentum equations can also be ignored. The conduction in the flow direction is ignored. The conservation of energy in a HTF CV can be written as.

$$V_{htf}\rho_{htf}c_{htf}\frac{\partial T_{htf}}{\partial t} = -c_{htf}\frac{\dot{m}_{htf}}{2}\frac{\partial T_{htf}}{\partial y}\Delta y + q_{htf} \qquad (11)$$

Heat is transferred in two directions. The mass flow $\dot{m}_{htf}$ through the channel and the HTF specific heat capacity c_{htf} determine the heat transfer in the flow direction. The factor ½ stems from the symmetry assumption. The heat transfer rate to the PCM q_{htf} is defined by the convective heat transfer of the HTF and the conduction through the PCM. It defined by dividing the temperature difference between PCM and HTF T_{pcm}-T_{htf} by the convective R_{conv} and the conductive resistance R_{pcm}.

$$q_{htf} = \frac{T_{pcm} - T_{htf}}{R_{conv} + R_{pcm}} \qquad (12)$$

A discretization of Equation (11) results in following point form.

$$a_{p,htf}T_{htf} = a_{nb,pcm}T_{pcm} + b_{p,htf}T_{htf}^{old} + a_{nb,htf}T_{htf,prev}$$

$$a_{nb,htf} = \frac{\dot{m}_{htf}c_{htf}}{2},\ a_{nb,pcm} = (R_{conv} + R_{pcm})^{-1}$$

$$b_{p,htf} = \frac{V_{htf}\,\rho_{htf}c_{htf}}{\Delta t}$$

$$a_{p,htf} = a_{nb,pcm} + a_{nb,htf} + b_{p,htf} \qquad (13)$$

The HTF temperature T_{htf} is determined by the temperature of the upstream HTF $T_{htf,prev}$, the temperature of the adjacent PCM T_{pcm} and its old value T_{htf}^{old}. The heat extracted from the PCM in the x-direction results in an increase of the HTF flowing in the y-direction.

Calculation procedure

The point forms of the PCM (Equation (9)) and the HTF (Equation (13)) result in a system of equations that determines the temperature field in the direction perpendicular to the flow.

The first time step is initiated by setting the upstream HTF temperature equal to the inlet temperature T_{in} of the thermal battery. The first system of equations is solved. The HTF temperature T_{htf} is used to initiate the calculations of the second system of equations. This procedure continues until the temperatures in all CVs are determined and the outlet temperature T_{out} is obtained. This corresponds to one time step and calculations are started for the second time step and so on.

Grid and time convergence

The convergence of the outlet temperature of the HTF in a fixed time frame is used to determine the dimensions of the grid and the time step. A maximum difference in temperature of 0.1 K is used as convergence criteria. This results in a grid of 15 and 7 control volumes in the x- and y-direction, respectively. A time step of 0.5 seconds is chosen.

MODEL VALIDATION AND COMPARISON

Model validation

The model is validated by comparison with experimental data [14]. The variable inlet conditions of temperature and mass flow rate are taken into account. The HTF inlet temperature rises during the charging process and the pump circulating the fluid does not immediately operate at full capacity. The comparison is done is Figure 4. The HTF fluid flowing through the thermal battery extracts energy from the PCM to charge the thermal battery. This results in a decreased PCM temperature while the HTF fluid heats up. The higher temperature throughout the PCM at the beginning of the charging process results in the observed outlet temperature peak. The effect is less pronounced for the numerical calculations. After the peak, the numerical outlet temperature gradually rises due to the higher inlet temperature and approaches the experimental results. The solidification has started and occurs in a fixed temperature range. This leads to a nearly constant temperature difference between inlet and outlet. The final numerical outlet temperature approaches the experimental value.

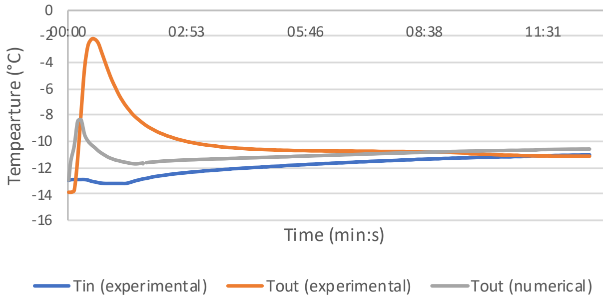

Figure 4 Comparison between numerical and experimental HTF outlet temperatures.

The difference in peak temperature between the numerical and experimental results is however 9.12 °C. The use of correct inlet conditions is necessary but does not allow validation of the model. A heat transfer process is not included at the start of charging.

Sensitive heat aluminum

Only the HTF and the PCM are included in the model. These two materials are however enclosed in aluminum profiles. This aluminum mass is also cooled down during the real charging process. This results in an extra sensible heat storage.

The influence of the aluminum sensible heat is investigated by calculating the ratio of aluminum sensible heat to the total heat stored in aluminum and PCM throughout the charging process. This ratio is plotted in Figure 5. Most of the aluminum is situated adjacent to the HTF and will have a lower temperature than most of the PCM at the start of the charging process, which results in the maximum ratio of 0.82. The ratio then decreases with time since parts of the PCM undergo a phase change with the accompanied high latent heat. The ratio converges to a fixed value towards the end of charging. The PCM is solidified and only extra sensible heat is stored.

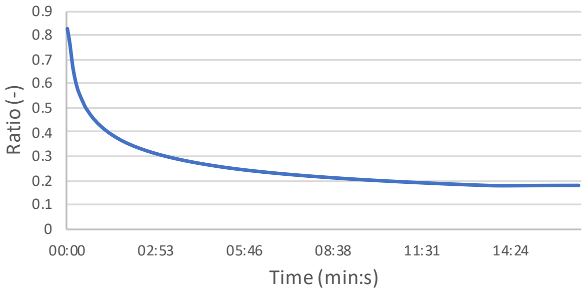

Figure 5 Ratio of sensible heat stored in the aluminium to the total stored heat in the aluminium and PCM during charging.

The collector bends were also not included in this investigation. Sensible heat will also be stored herein. It can thus be concluded that the sensible heat of the aluminum is not negligible in the early stages of charging, especially before solidification has started. Including this in the model should result in a better resemblance of the HTF outlet temperature.

PCM temperatures

The numerical PCM temperatures are also compared with experiments [14]. Three numerical temperatures are considered along the direction perpendicular to the flow (Figure 3). One is located next to the HTF, one at the end of the grid and one in between. One experimental measurement is taken at the center of each profile. This corresponds to the temperature at the end of the grid. These temperatures are plotted in Figure 6.

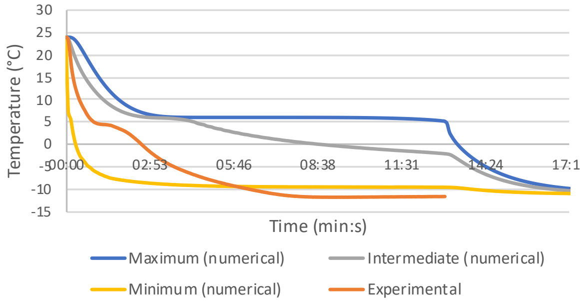

Figure 6 Comparison between numerical and experimental PCM temperatures

The evolution of the PCM temperature is as follows. The PCM is first cooled to the solidification temperature. It is in a mushy state during the phase change process and cools further down when it is completed. This process happens faster closer to the HTF.

The experimental temperature does not correspond with the numerically calculated temperature at the end of the grid, which should be the case. It is better approximated by the intermediate temperature. A reason for this could be the aluminium thermowells used to measure the temperatures. They are placed inside the PCM. They will act as fins due to their high thermal conductivity. This influences the phase change front propagation. A solid layer will form on the thermowells before the surrounding PCM is solidified. The temperature of a layer closer to the HTF is thus measured. It is thus hard to compare with experimental data, since the phase change front is influenced by the thermowell.

The numerical PCM temperatures of the four profiles are illustrated in Figure 7. The phase change starts at the same moment in all the profiles. This is not the case in the experimental results [14]. There is a small delay in solidification completion. This implicates a nearly homogeneous phase change in all four profiles. This is explained by the low temperature peak in HTF at the start of charging (Figure (4)), which implicates a nearly constant heat transfer rate along the channels. Including the aluminium sensible heat should however result in a less homogenous phase change. It has a large influence at the beginning of charging prior to solidification.

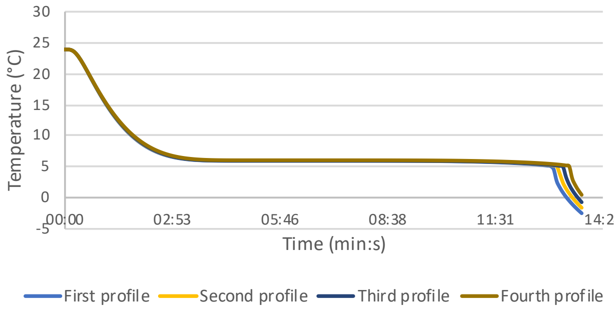

Figure 5 Maximum temperature profiles of the PCM in four profiles.

Metal foam enhanced PCM

The metal foam enhanced PCM is modelled by a one-temperature model. The effective thermal conductivity is calculated with the correlation of Boomsma and Poulikos [13]. Increasing the conductivity results in a solidification time of two minutes compared to twelve when no foam is used. The metal foam has thus a significant positive effect of the charging process.

The HTF outlet temperature is compared with experiments [14] in Figure 8. A similar trend is perceived. The temperature peak at the beginning of charging is lower than in the experiments. This was accounted to the exclusion of aluminium sensible heat in the model. The temperature rises later in the experiments. This could be explained by the fact that the first HTF that is measured at the outlet has not passed through the thermal battery, that there is a measurement lag and that the pump does not immediately operate at full capacity.

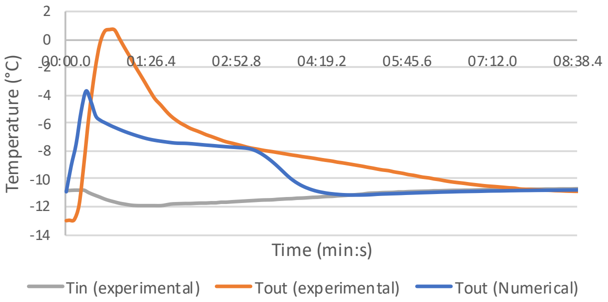

Figure 6 Comparison between numerical and experimental HTF temperatures for a metal foam enhanced PCM

A temperature plateau is observed after the peak in the numerical calculations. This indicates that the temperatures inside the PCM are close to each other during charging. The temperature rapidly decreases after this plateau. The solidification is completed and the extra sensible energy storage requires less energy.

The simulated metal foam enhanced PCM is solidified faster than in the experiments. The heat transfer rate is thus overestimated in the numerical calculations. The metal foam was placed inside the PCM channels without a bonding method. This implicates a thermal contact resistance between the metal foam and the channel wall. This has a negative effect on the heat transfer rate. An extra thermal resistance could be added in Equation (12) to calculate a lower heat transfer rate between HTF and PCM.

CONCLUSIONS

It is not possible to validate the enthalpy model of the PCM with experimental results. A lower increase in HTF temperature flowing through the channel is observed. The influence of the sensible heat of the excluded aluminum mass was investigated. It was concluded that it has a significant effect during the early stages of charging, especially before solidification. Including this should offer a better resemblance with the experimental results.

Comparison of the PCM temperatures with experimental data is difficult to perform. The thermowells used in the experiments have an influence on the phase change front. It is not one-dimensional as assumed in the model.

A homogenous phase change is perceived in the simulations, which is not the case in reality. Including the aluminum mass should eliminate this due to the higher temperature gradient between inlet and outlet of the HTF during the early stages of charging.

The one-temperature model of the metal foam enhanced PCM overestimates the heat transfer rate. A thermal contact resistance exists between the metal foam and the channel wall due to the lack of a bonding method. Including an extra thermal resistance to calculate the heat transfer rate between HTF and PCM could model this phenomenon.

REFERENCES

[1] Improving cold storage equipment in europe – intelligent energy europe – European commission. https://ec.europa.eu/energy/intelligent/ projects/en/projects/ice-e#results. Accessed: 2018-05-20

[2] George A Lane. *Solar heat storage: latent heat materials.* CRC Press, Boco Raton, FL, 1983.

[3] K.K. Pillai and B.J Brinkworth. The storage of low grade thermal energy using phase change materials, *Applied Energy,* 2(3):205-216, 1976.

[4] A. Abhat. Low temperature latent heat thermal energy storage: Heat storage materials. *Solar Energy*, 30(4):313-320, 1983.

[5] Jianqing Chen, Donghui Yang, Jinghua Jiang, Aibin Ma, and DanSong. Research progress of phase change materials (pcms) embedded with metal foam (a review). *Procedia Materials Science*, 4(Supplement C):389-394, 2014. 8th International Conference on Porous Metals and Metallic Foams.

[6] Shuli Liu, Yongcay Li, and Yaqin Zhang. Mathematical solutions and numerical models employed for the investigations of PCMs phase transformations. *Renewable and Sustainable energy reviews*, 33:659-674, 2014.

[7] Yvan Dutil, Daniel R Rousse, Nizar Ben Salah, Stéphane Lassue, and Laurent Zalewski. A review on phase-change material: mathematical modelling and simulations. *Renewable and sustainable Energy review*, 15(1):112-130, 2011.

[8] Jozef Stefan, Uber einige probleme der theorie der warmeletung. *Sitzer. Wien. Akad. Math. Naturw.*, 98:473-484, 1889.

[9] Atul Sharma, V.V. Tyagi, C.R. Chen, and D. Buddhi. Review on thermal energy storage with phase change materials and applications. *Renewable and sustainable Energy Reviews*, 13(2):318-345, 2009.

[10] Piia Lamberg, Rejo Lehtiniemi, and Anna-Maria Henell. Numerical and experimental investigation of melting and freezing process in phase change material storage. *International Journal of Thermal Sciences*, 43(3): 277-287, 2004.

[11] P.G. Kroeger and S. Ostrach. The solution of a two-dimensional freezing problem including convection in the liquid region. *International Journal of Heat and Mass Transfer*, 68(Supplement C):677-682, 2014.

[12] Xin Hu and Soumya S. Patnaik. Modelling phase change material in micro-foam under constant temperature condition. *International Journal of Heat and Mass Transfer*, 68(Supplement C):677-682, 2014.

[12] K. Boomsma and D. Poulikakos. On the effective thermal conductivity of a three-dimensionally structured fluid-saturated metal foam. *Journal of Heat and Mass Transfer*, 44(4):827-836, 2001.

[14] Michiel Corryn. Charging and discharging behavior of a thermal storage for passive cold chain transport based on phase change material enhanced with metal foam, Ghent University, June 2017

[15] VR Voller, CR Swaminathan, and Brian G Thomas. Fixed grid techniques for phase change problems: a review. *International Journal for Numerical Methods in Engineering*, 30(4):875-898, 1990.

[16] V. R., and C. R. Swaminathan. "General Source-based method for solidification phase change." *Numerical Heat Transfer, Part B Fundamentals* 19.2 (1991): 175-189.

Contents

List of Figures

List of Tables

Nomenclature

Greek symbols

β	thermal expansion	[1/K]
Δ	liquid fraction correction	[-]
Δh_m	latent heat of fusion	[J/kg]
$\Delta h_{m,v}$	volumetrice latent heat of fusion	[J/m^3]
Δh_r	endorthermic heat of reaction	[J/kg]
Δt	time step	[s]
Δx	space step	[m]
δH	difference solid and liquid enthalpies	[J/m^3]
δ	phase change fraction	[-]
ε	effectiveness	[-]
λ	under-relaxation paramter	[-]
μ	dynamic viscosity	[mPas]
ρ	density	[kg/m^3]
σ	surface-to-volume ratio	[m^2/m^3]
γ	porosity	[-]
$\partial/\partial t$	partial time derivative	[1/s]
$\partial/\partial t$	partial space derivative	[1/m]
∇	del operator	[-]

Abreviations

CV	Control Volume
DNS	Direct Numerical Simulations
HTF	Heat Transfer Fluid
LTES	Latent Thermal Energy Storage
LTNE	Local Thermal Non-Equilibrium
NTU	Number of Transfer Units
ODE	Ordinary Differential Equation
PCM	Phase Change Material
PPI	Thermal Storage Unit
STES	Sensible Thermal Energy Storage
TC	Thermocouple
TSU	Thermal Storage Unit

Symbols

A	surface area	[m^{-1}]
A_R	heat transferring area	[m^2]
A_{sf}	specific surface area	[m^{-1}
a_m	fraction melted	[-]
a_r	fraction reacted	[-]
c	specific heat capacity	[J/kgK]
D_h	hydraulic diameter	[m]
d_f	fibre diameter	[m]
d_{pcm}	thickness solid PCM layer	[m]
df/dT	derivative of liquid fraction	[1/K]
E	energy	[J]
f	liquid fraction	[-]
g	acceleration of gravity	[m/s^2]
H	total volumetric enthlapy	[J/m^3]
h	height channels	[m]
h_{conv}	convection coefficient	[W/m^2]
h_{in}	enthalpy inlet	[J/kg]

h_{sf}	interstitial heat transfer coefficient	[]
h_{out}	enthalpy outlet	[J/kg]
k	thermal conductivity	[W/mK]
L	length channels	[m]
m	mass	[kg]
$\dot{m}$	total mass flow rate	[kg/s]
$\dot{m}_{htf}$	mass flow rate one HTF channel	[kg/s]
Nu	Nusselt number	[-]
n	number of channels	[-]
P	perimeter	[m^2]
P	power	[W]
Pr	Prandtl number	[-]
Q	stored heat	[J]
Q_{htf}	heat transfer rate between HTF and PCM	[W]
Q_{losses}	heat losses to the environment	[W]
q	heat transfer rate	[W]
$\dot{q}$	heat flux density	[W/m^2]
R	thermal resistance	[K/W]
Re	Reynolds number	[-]
X	error	[%]
T	temperature	[°C]
T_m	melting temperature	[°C]
t	time	[s]
S	source term	[-]
S_c	constant term of source term	[-]
S_p	linear term of source term	[-]
V	volume	[m^3]
v	speed	[m/s]
U	Internal energy	[J]
w	width	[m]

Subscripts

al	aluminium
amb	ambient
cond	conductive
conv	convective
f	final
htf	heat transfer fluid
in	inlet
init	initial
ins	insulation
k	number of CVs in the y-direction
l	liquid
max	maximum
n	number of CVs in the x-direction
nb	neighbour point
out	outlet
p	node point
p-1	west neighbour point
p+1	east neighbour point
pcm	phase change material
s	solid
tot	total
w	wall

Supscripts

old	value previous time step
m	iteration level

Chapter 1

Introduction

Cold storage is amongst other used in the food and pharmaceutical industry. An elevated temperature results in spillage of the products. Freezing of products results in damaged goods. The products thus needs to be kept at a predetermined temperature range to avoid waste. Maintaining this cold chain requires energy. The cold chain also needs to be maintained during the transport of products, where cooling energy is required on top of the transport energy. It is estimated that the cold chain is responsible for 2.5% of the global greenhouse gas [1]. Improvements in this field has thus positive environmental implications.

An active system can be used to maintain the predetermined temperature range. Active cooling is obtained with the use of a refrigerating cycle. The use of mobile active coolers during transport has some disadvantages. It has to be small and light. This results in a lower efficiency when compared to stationary coolers [2]. They also require a continuous power and regular maintenance to ensure proper functioning. The added mass and vibrations are also drawbacks.

A passive cooling system could be used instead during transport. This is done by placing a pre-chilled mass in an insulated container. The absence of an active cooler makes this way of cooling cheaper, lighter and vibration free. The drawback is that the temperature cannot be controlled actively. A thermal mass is needed to absorb the heat entering the container and keeping it in the predetermined temperature range. The duration and conditions of the transport needs to be taken into account during design to allow this for the entire shipment.

The main disadvantage of the thermal mass is that it needs to be chilled again prior to each transport and cannot operate continuously.

The material used as a thermal mass has some requirements. First, it needs to have a high energy storage density to maintain its weight at a minimum. Secondly, the energy absorption needs to happen in the predetermined temperature range. Finally, the pre-chilling process has to be has short as possible.

1.1 Heat storage methods

The most widely used techniques for thermal energy storage are sensible, latent and thermochemical storage. Sensible thermal energy storage (STES) is achieved by changing the temperature of the storage material from an initial temperature T_{init} to a final temperature T_f. No phase change occurs during this process. The energy required for this action is a function of temperature difference and specific heat capacity c of the material used in the sensible storage system. Following equation gives the amount of stored stored sensible heat [3].

$$Q_{sens} = \int_{T_{init}}^{T_f} mcdT \tag{1.1}$$

Energy is also stored or released during the phase change of a material, which is referred to as latent thermal storage (LTES). The high energy storage density makes it a more interesting [4] storage method. This density is 5 to 14 times higher than for sensible heat storage materials [5]. The LTES is based on the latent heat of fusion Δh_m and the melted fraction a_m of the material. Sensible energy is also stored by increasing the temperature from the initial temperature T_{init} to a final temperature T_f. The stored heat of a medium undergoin a phase change is given by following equation [3].

$$Q_{sens,latent} = \int_{T_{init}}^{T_m} mC_p dT + m a_m \Delta h_m + \int_{T_m}^{T_f} mC_p dT \tag{1.2}$$

LTES has two advantages compared to STES mentioned above. It offers a high density storage at nearly constant temperature, which is the phase change temperature of the material. The transition can be solid-solid, solid-liquid, solid-gas, liquid-gas and vice-versa. Liquid-gas and solid-gas have a higher latent heat of fusion than the solid-liquid ones, but a large change in volume occurs. This makes the implementation of these systems impractical [6] and its storage density is lower. Solid-solid transitions are associated with small volume changes and thus higher design flexibility [7]. but their latent heat of fusion is lower than for solid-liquid transitions. This makes solid-liquid transitions most attractive due to their small volume change and their high energy storage density. Their use in thermal energy storage systems has the potential of being economically viable [5]. The advantages and disadvantages of different types of phase change materials (PCM) will be discussed in next section.

Thermal energy can also be stored in the form of thermochemical energy. These systems are based on the energy absorbed or released during breaking and reforming of the molecular structure. This process has to be reversible. The amount of storage Q_{chem} is based on the endothermic heat of reaction Δh_r and the fraction reacted a_r.

$$Q = a_r m \Delta h_r \tag{1.3}$$

1.2 Phase change materials

Phase change materials (PCM) are used for latent thermal energy storage. Abhat [6] classified the different types of solid-liquid PCMs, which can be seen in Figure 1.1. They are divided into three groups: organic, inorganic and eutectic. Carbon based materials are organic and are further subdivided into paraffins and non-paraffins. Inorganic materials are divided into salt hydrates and metallics. By mixing two or more PCMs, the eutectic type is formed. The mixing is done to attain a specified melting temperature, which is the main selection criterium of a PCM [8].

The PCMs need favourable thermo-physical properties. These include, amongst other, a melting temperature that fits the application, a high latent heat of fusion, a high thermal conductivity, a high density, a low volume change during phase change, long term chemical stability and a low degree of supercooling [6, 9]. Supercooling is the phenomenon where crystallisation starts at a temper-

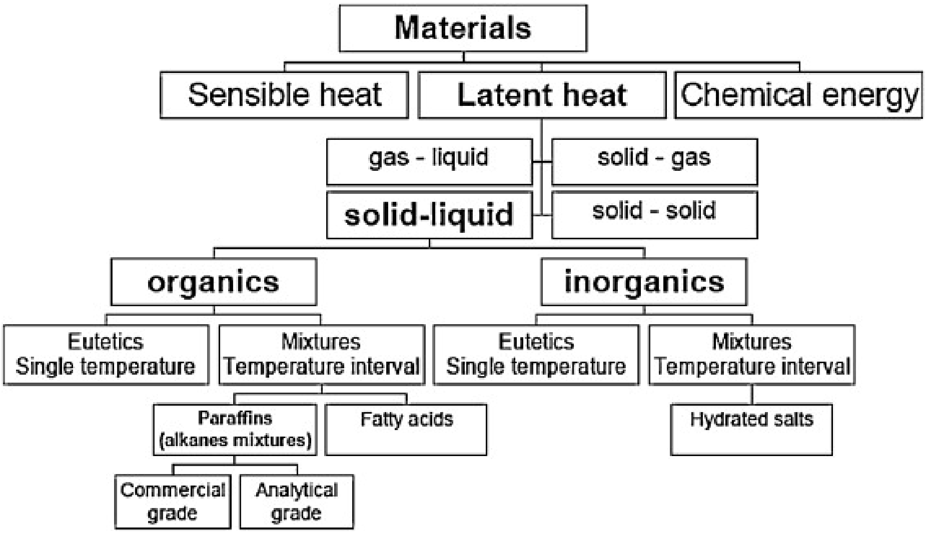

Figure 1.1: Classification of PCMs. [6]

ature below the freezing temperature. This means that the PCM does not start solidifying upon reaching the freezing temperature. It is even possible that no nucleation at all occurs and only sensible energy is stored [4]. Since no material satisfies all the above mentioned criteria a trade-off has to be considered.

Inorganic PCMs have a high latent heat of fusion (250 - 400 MJ/m^3), a higher thermal conductivity (0.6 W/mK) compared to organic PCMs (0.2 W/mK) and are cheap. They are also corrosive to metals and suffer from supercooling and phase separation. These drawbacks limits their application [10]. Adding suitable thickening and nucleating agents can lower the degree of supercooling [11]. Phase separation occurs when the PCM with several component does not melt homogeneously. This is referred to as congruent melting. Due to the difference in mass density of these components, the phase separation will occur under influence of gravity. This leads to a low cycling stability of the PCM.

Organic PCMs have a high latent heat of fusion (125 - 200 MJ/m^3), are non-corrosive and do not suffer from phase separation. Paraffin waxes freeze without supercooling and non-paraffin or fatty acids with none or little supercooling [6]. Non-paraffins have excellent melting and freezing properties, but are approximately three times more expensive than paraffins [12]. The major drawback of organic PCMs is their low thermal conductivity of around 0.2 W/mK, which limits their application [10].

PCMs have a high latent heat of fusion, which offer the possibility to achieve a high energy storage density. Their low thermal conductivity (0.1 to 0.6 W/mK [13]) however is a drawback. It is especially the case for organic PCMs. This leads to a low heat transfer rate during the charging and discharging processes.

Several methods can be used to achieve a conductivity enhancement. Extended metal surfaces [14], conductive powders [13] or conductive matrices [15] are examples of effective ways to increase the charge and discharging effectiveness. An open cell metal foam has a high conductivity, a high surface to volume ratio and high porosity. This makes it an effective way to increase the heat transfer in PCMs [16].

In conclusion, PCMs offer the possibility to store thermal energy with a high density. Organic PCMs are preferred over inorganic due to the absence of supercooling, phase separation and corrosion. This ensures the performance of the thermal storage unit (TSU) over time. They however have a low thermal conductivity and thus low heat transfer rates for charging in discharging. This conductivity can be enhanced by embedding open cell metal foam in the PCM, which results in an increased effective conductivity and accompanying heat transfer rates.

Studying TSUs with PCM can be done either experimentally or numerically. Experimental investigation offers a better indication of the actual PCM behaviour and performance [17]. However, experiments are time and cost consuming. A test rig needs to be constructed for each specific application. They are also prone to testing errors.

From a design point of view, a numerical approach is preferred. The major advantage is that various conditions can be simulated by changing the variables in a numerical model [17]. The phase change process is however a complex mechanism. Correctly modelling this process is necessary to allow an accurate design of TSUs. This brings us to the focus of this master dissertation, which is the modelling of a cold storage with metal foam enhanced PCM. An overview of available models in literature will be given in the following chapter.

Chapter 2

Literature survey

2.1 Analytical models

2.1.1 One phase Stefan problem

A material undergoing a phase transition has a moving phase change front. This type of boundary value problem for partial differential equations is referred to as a Stefan or moving boundary problem. Stefan [18] applied this problem on the freezing of the ground. He formulated the energy equation at the solid-liquid interface with the following equation.

$$\rho \Delta h_m \left(\frac{ds(t)}{dt} \right) = k_s \left(\frac{\partial T_s}{\partial t} \right) - k_l \left(\frac{\partial T_l}{\delta t} \right) \tag{2.1}$$

This is referred to as the Stefan condition, where $s(t)$ is the position of the solid-liquid interface, Δh_m is the latent heat of fusion and ρ is the density. The movement of the solid-liquid interface $\frac{ds(t)}{dt}$ is driven by the change in temperature $\frac{\partial T}{\partial t}$ and conductivities k of the solid (s) and liquid (l) material.

The non-linear nature of the phase change at the boundary and the different thermo-physical properties of the phases makes it difficult to predict the behaviour of the phase change [19]. An analytical solution in closed form can however be obtained for a one-dimensional semi-infinite material [4]. Four thermal restrictions are made in this model.

- Only latent heat storage is considered.

- Heat is only transferred by conduction and the convection inside the PCM is ignored.
- The initial state of the PCM is liquid and at its phase change temperature T_{pcm}.
- The temperature at the boundary is set at T_{init} and is kept constant.

Since the sensible heat is ignored, the heat $dQ(t)$ that is extracted to move the interface over a distance $ds(t)$ is equal to the heat that leaves the surface. $\Delta h_{m,v}$ is volumetric latent heat of fusion. The heat flux density $\dot{q}$ at the surface is then obtained by dividing by the area A and taking the derivative.

$$dQ(t) = \Delta h_{m,v} A ds(t) \tag{2.2}$$

$$\dot{q}(t) = \Delta h_{m,v} \frac{ds(t)}{dt} \tag{2.3}$$

The sensible heat is negligible and the only heat transfer mode is conduction. This results in a linear temperature change as function of distance s, defined by the conduction k and temperature difference between the initial temperature T_{init} and the phase change temperature T_{pcm}.

$$\dot{q}(s) = k \frac{T_{pcm} - T_{init}}{s} \tag{2.4}$$

The heat flux is set to Equation 2.3 and Equation 2.4.

$$\Delta h_{m,v} \frac{ds}{dt} = k \frac{T_{pcm} - T_{init}}{s} \tag{2.5}$$

Time and space variables are separated and the former equation is integrated with respect to time.

$$\frac{k(T_{pcm} - T_{init})}{\Delta h_m} t = \frac{1}{2} s(t)^2 \tag{2.6}$$

This results in following expression for the phase interface location as a function of time.

$$s(t) = \sqrt{2 \frac{k(T_{pcm} - T_{init})}{\Delta h_{m,v}} t} \tag{2.7}$$

The heat flux density as a function of time is then obtained by substituting the former in Equation 2.3.

$$\dot{q}(t) = \sqrt{\frac{(T_{pcm} - T_{init}) k \Delta h_{m,v}}{2t}} \tag{2.8}$$

Previous derivation assumes a temperature change directly at the surface of the PCM. In a real design there will be a HTF at the boundary. This introduces an extra thermal resistance and leads to a slightly different solution of the one phase Stefan problem.

Closed form equations can be valuable to get a first order approximation but they have important geometrical and thermal restrictions. They only include latent heat. A uniform melting temperature at the beginning of the phase change. A single melting temperature is also assumed, although most PCMs have a melting temperature range. The natural convection in the PCM is ignored. This is valid for a solidification process. During melting the temperature gradients inside the liquid PCM are larger and thus resulting in buoyancy effects. More detailed and realistic models are thus needed which will be discussed in Section 2.2.

2.1.2 Effectiveness-NTU method

The effectiveness ε of a heat exchanger is the ratio of the actual heat transfer rate q to the maximum theoretical one q_{max}, which is obtained for an infinitely long counter flow heat exchanger. It is a performance parameter of a heat exchanger. It is expressed with following equation.

$$\varepsilon = \frac{q}{q_{max}} \tag{2.9}$$

The effectiveness can also be expressed as a function of the number of transfer units (NTU) between the heat exchanging materials. A material undergoing a phase change, appears to have a large specific heat capacity. This leads to the following simplified correlation of the effectiveness [20].

$$\varepsilon = 1 - e^{-NTU} \tag{2.10}$$

The NTU is a function of mass flow rate $\dot{m}$, specific heat capacity c and total thermal resistance R_{tot} of the heat exchanger.

$$NTU = \frac{1}{R_{tot}\,\dot{m}\,c} \tag{2.11}$$

The effectiveness-NTU method calculates the effectiveness of a heat exchanger operating in steady state. Equation 2.13 is valid for a material undergoing a phase change. A thermal storage unit (TSU) can be modelled as a heat exchanger, where the PCM acts a fixed heat source at its phase change temperature T_{pcm}. The effectiveness-NTU method could be used to calculate its effectiveness. A TSU however never operates in steady state as seen in Section 2.1.1. An instantaneous effectiveness can however be calculated and from this an average value.

To calculate the instantaneous effectiveness with Equation 2.13, the NTU needs to be determined. The total thermal resistance between HTF and phase change front R_{tot} is needed for this. It is series of three resistance. These are the convective resistance of the HTF R_{conv}, the conductive resistance of the container wall R_{wall} and the conductive resistance of the solid part of the PCM R_{pcm}. This results in following equation.

$$R_{tot} = R_{conv} + R_{wall} + R_{pcm} \tag{2.12}$$

The conductive PCM resistance will be time dependent due to the growth of the solid PCM layer. A TSU thus will never operate in steady state. The time dependent heat transfer rate q can however still be calculated. The maximum heat transfer rate q_{max} occurs when the outlet temperature of the HTF T_{out} is equal to the PCM temperature T_{pcm}. If a constant specific heat capacity is assumed, this results in following expression of the effectiveness.

$$\varepsilon = \frac{q}{q_{max}} = \frac{T_{in} - T_{out}}{T_{in} - T_{pcm}} \tag{2.13}$$

Effectiveness can be a useful design parameter for PCM TSUs [21]. The charging and discharging process can be described using the effectiveness. For a discharging process, the outlet temperature of the HTF has to meet certain specifications, which results in a minimum required effectiveness for proper functioning of the TSU. For the charging process no restrictions are set for the outlet temperature. Effectiveness should however be maximised for both cases to minimise exergy losses. This type of analysis only considers the latent energy storage. Disregarding the sensible heat can be justified by the fact that for a small temperature change of the PCM the latent heat is a multitude of the sensible part [22].

For a classical effectiveness analysis, the NTU of the heat exchanger is constant with mass flow rate, due to the constant R_{tot} (Equation 2.11). For a PCM TSU the phase change front will propagate with time. This changes the value of R_{pcm} and thus also the total thermal resistance (Equation 2.12). This then results in a varying NTU between the HTF and the liquid PCM. This results in a quasi-steady approach, where an equilibrium exists at every time step between the HTF and the PCM.

Tay et al. [23] characterised a coil-in-tank phase change thermal energy storage using the above mentioned effectiveness-NTU method. They defined a one-dimensional NTU correlation by ignoring the heat transfer in the HTF flow direction. They formulated a total thermal resistance where the phase change front is defined by a shape factor. A round and a square one (Figure 2.1) was used.

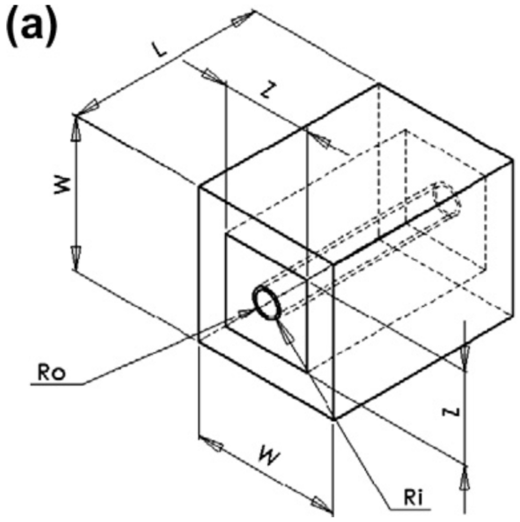

Figure 2.1: Square shape of the PCM phase change front. [23]

It was concluded that the two shape factors results in a similar R_{pcm} with an average difference of 3%. Both factors can thus be used for calculating the effectiveness using Equation 2.13. The shape factor is time dependent, but the resistance of the solid PCM is calculated using the phase change fraction δ as an independent variable. To obtain a single performance parameter they calculated the average effectiveness with following equation.

$$\bar{\varepsilon} = \int_{\delta=0}^{\delta=1} \varepsilon d\delta = \int_{\delta=0}^{\delta=1} (1 - e^{\frac{1}{R_T \dot{m} C_p}}) d\delta \tag{2.14}$$

Comparison of this average value for different $\dot{m}/A$ ratios with experimental data shows good agreement. The average absolute error is 13%. Larger errors occur for the melting process due to the natural convection inside the liquid PCM following from large temperature differences, which results in a lower calculated average effectiveness. The difference between melting and freezing process is that for melting the resistance of the PCM is determined by the PCM in liquid state. Temperature differences in this liquid state will result in buoyancy effects which lowers the resistance. This effect is neglected in the effectiveness-NTU method since it is temperature independent.

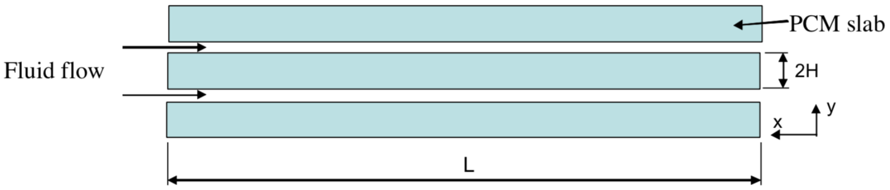

Figure 2.2: PCM slabs with fluid flow through. [21]

Belusko et al. [21] performed an effectiveness-NTU analysis for a different geometry, which consists of PCM slabs with gaps in between where the HTF can pass through. Another difference with the model of Tao et al. [23], is a two-dimensional phase change propagation. The heat transfer rate will be larger at the HTF inlet where larger temperature differences are present. The schematic representation of the phase change front can be seen in Figure 2.3. They also ignored the natural convection inside the PCM due to the small slab thickness [24].

Above mentioned authors [21, 23] performed the effecitveness-NTU analysis on the entire length of the TSU. Browne and Bansal [25] divided a TSU in several elements before performing the analysis for The temperature of the HTF varies throughout the chiller, which alters the local heat transfer coefficients. By di-

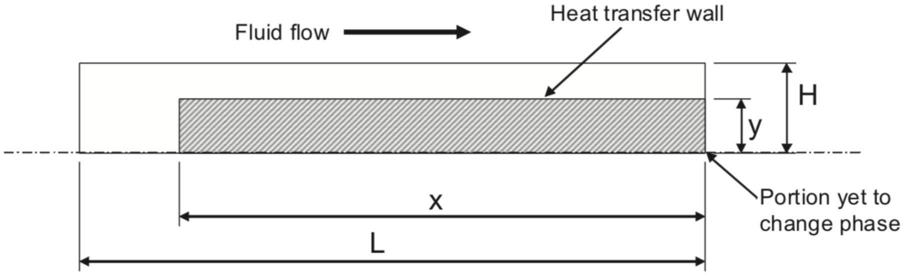

Figure 2.3: Approximation of solid-liquid phase change front. [21]

viding the chillers in several elements, a more accurate modelling of this effect is obtained.

It was discussed that that the effectiveness can be a useful design parameter for PCM TSUs [21]. Only latent heat is however considered since the PCM is acting as a heat source at fixed temperature. Including the sensible heat would increase the accuracy of phase change problem. Models which include this sensible heat will be discussed in next section.

2.2 Numerical models

The moving boundary problem has a non-linear structure and the behaviour of the phase change is difficult to predict and analytical solutions are only valid for highly simplified cases as explained in previous section. Two numerical solutions are the enthalpy method and effective heat capacity method which will be explained hereunder.

2.2.1 Enthalpy formulation

To simplify the solution of the phase change problem an enthalpy method is introduced. An enthalpy as function of temperature is defined. The conservation of energy for a phase change problem can then be expressed as follows [26].

$$\frac{\partial H}{\partial t} = \nabla(k_k(\nabla T)) \tag{2.15}$$

The total volumetric enthalpy H consists of the sensible and latent heat stored in the PCM.

$$H(T) = h_{sens}(T) + \rho_l f(T) \Delta h_m \tag{2.16}$$

The sensible enthalpy h_{sens} is the integral of the mass density ρ_k and specific heat capacity c_k over temperature.

$$h_{sens} = \int_{T_m}^{T} \rho_k c_k dT \tag{2.17}$$

The liquid fraction f for a single melting temperature T_m is expressed as follows for isothermal phase change.

$$f = \begin{cases} 0 & , T < T_m \text{ (solid)} \\ 0-1 & , T = T_m \text{ (mushy)} \\ 1 & , T > T_m \text{ (liquid)} \end{cases} \tag{2.18}$$

From the total volumetric enthalpy the PCM temperature can be calculated. For PCMs with a single melting temperature this results in following expressions.

$$T = \begin{cases} \frac{T_m + H}{\rho_s c_s} & , T < T_m \text{ (solid)} \\ T_m & , T = T_m \text{ (mushy)} \\ T = \frac{T_m + (H - \rho_l \Delta h_m)}{\rho_l c_l} & , T > T_m \text{ (liquid)} \end{cases} \tag{2.19}$$

With the definition of the total volumetric enthalpy (Equation 2.16) and the sensible enthalpy (Equation 2.17), the energy conservation (equation 2.15) can be rewritten. The equation is as follows for two-dimensional heat transfer.

$$\frac{\partial h}{\partial t} = \frac{\partial h}{\partial x}\left(\alpha \frac{\partial h}{\partial x}\right) + \frac{\partial h}{\partial y}\left(\alpha \frac{\partial h}{\partial y}\right) - \rho_l \Delta h_m \frac{\partial f}{\partial t} \tag{2.20}$$

The liquid fraction of the mushy zone can also be defined for a melting range between T_s and T_l. According to the research of Tittelein et al. [27] this is a better representation of the phase change process since most PCMs are not pure substances with a single melting temperature. The liquid fraction is defined as a linear function of temperature by several authors [28, 29, 30, 31].

$$f = \begin{cases} 0 & , T < T_s \text{ (solid)} \\ (T - T_s)/(T_l - T_s) & , T_s \leq T \leq T_l \text{ (mushy)} \\ 1 & , T > T_l \text{ (liquid)} \end{cases} \tag{2.21}$$

The method has the following advantages.

- The general heat transfer equation is similar to the single phase equation.
- The solid-liquid interface condition is automatically obeyed.
- The mushy zone can be properly modelled.

In order to solve the enthalpy formulation an adequate liquid fraction update needs to be done in the mushy zone. Voller and Swaminathan [32] have proposed a numerical scheme to solve this update for solidification processes. This method is discussed in Section 4.3.2.

2.2.2 Effective heat capacity formulation

Another way to model the phase change problem is by expressing the latent heat storage with a temperature dependent specific heat capacity. Three different heat capacities will be present: the solid, liquid and melting one. The latent heat is aprroximated by a large heat capacity. The effective specific heat c_{eff} occurs during the phase change over a fixed temperature range which is the melting range of the PCM ($\mathrm{T_s}$ to $\mathrm{T_l}$) [33]. It is directly proportional to the latent heat of fusion Δh_m.

$$c_{eff} = \frac{\Delta h_m}{T_l - T_s} + c_s \tag{2.22}$$

This results in a energy conservation equation dependent on temperature.

$$\rho c_{eff} \frac{\partial T}{\partial t} = \nabla(k(\nabla T)) \tag{2.23}$$

The disadvantages of the the effective heat capacity formulation are the difficulty of solving phase change problems for a narrow melting range and its inapplicability for isothermal phase changes [17].

2.2.3 Modelling of convection in the PCM

The buoyancy effects during phase change in the liquid PCM cannot always be ignored. This is especially the case for the melting process. There is a larger temperature gradient in the liquid PCM which is situated between the HTF and the liquid-solid interface. The natural convection following from this temperature difference will have a positive effect on the melting rate. Several ways of including this is now discussed.

Several authors [34, 35, 36, 37] included the effects of natural convection by introducing an effective thermal conductivity of the liquid state k_l. They used following empirical correlation [38], where the constants C and n are determined experimentally and Ra is the Rayleigh number.

$$\frac{k_{eff}}{k_l} = CRa^n \tag{2.24}$$

The thermal conductivity of the PCM k_{pcm} is then represented by the mean value of the PCM in liquid k_{eff} and in solid k_s state.

$$k_{pcm} = fk_{eff} + (1-f)k_s \tag{2.25}$$

Tao and He [39] and Qarnia et al. [40] also included the effects of the melt thickness δ of the liquid PCM. This simulation was done for a circular HTF tube. The constant C is dependent of the inlet temperature of the HTF.

$$\frac{k_{eff}}{k_l} = CRa^n \left(\frac{\delta}{R - R_i} \right)^m \tag{2.26}$$

All above mentioned authors integrated their effective thermal conductivity of the liquid PCM in the enthalpy model with single melting temperature explained in Section 2.2.1.

Lamberg et al. [33] expressed the natural convection during melting by a heat transfer coefficient h_c [41] based on the temperature difference of the wall T_w and the melting temperature T_m, gravity g and thermal expansion β.

$$\rho\frac{\partial H}{\partial t} + h_c\nabla T = \nabla(k\nabla T) \tag{2.27}$$

$$h_c = 0.072\left(\frac{g((T_w - T_m)/2)\rho_l^2 c_{pl} k_l^2 \beta}{\mu}\right)^{1/3} \tag{2.28}$$

During solidification of the PCM, the main heat transfer mode is conduction due to the lower temperature gradient in the liquid PCM [42]. This means that the positive effect of convection in the PCM is negligible during solidification, which is not the case for the melting process.

2.2.4 Modelling of porous material in PCM

Introducing a high conductivity porous material, such as metal foam, in the PCM will increase the effective thermal conductivity, but two material with different thermo-physical properties are now present. This makes the numerical modelling more complex due to the complicated pore structure.

One-temperature model

Hu and Patnaik [43] performed a one-temperature simulation of the phase change problem. The metal foam and PCM act as a homogeneous material and they have the same temperature. The phase problem can thus be described by a single energy equation.

$$(\gamma\rho_f c_{p,f} + (1-\gamma)\rho_s c_{p,s})\frac{\partial T}{\partial t} = \nabla(k_{eff}\nabla T) - \rho_f\gamma\Delta h_m\frac{\partial f_l}{\partial t} \tag{2.29}$$

The porosity of the foam γ, the conductivity of the PCM k_f, the conductivity of the foam k_s and the structure of the foam will determine the effective conductivity k_{eff} of the composite material [43]. A first order approximation based on the conductivities and the porosity γ is possible.

$$k_{eff} = \gamma k_f + (1-\gamma)k_s \tag{2.30}$$

The first order approximation however overestimates k_{eff} [43]. The Progelhof model [44] can also be used, where a power law (α) of the porosity is added. It consequently results in a lower k_{eff}. Hu and Patnaik [43] obtained a correlation in agreement with this model by performing direct numerical simulation (DNS) on a unit cell level.

$$k_{eff} = \gamma k_f + (1-\gamma)^{\alpha} k_s \tag{2.31}$$

Boomsma and Poulikakos [45] presented a correlation of k_{eff} based on a three-dimensionally structured model of the metal foam. It is a tetrakaidecahedron with cylindrical ligaments and cubic nodes. This structure with the unit cell used in the approximation can be seen in Figure 2.4. This leads to following equations, where k_s and k_f are the conductivities of the foam and the PCM, respectively. Several authors [46, 47] used these correlations in their calculation of the effective conductivity.

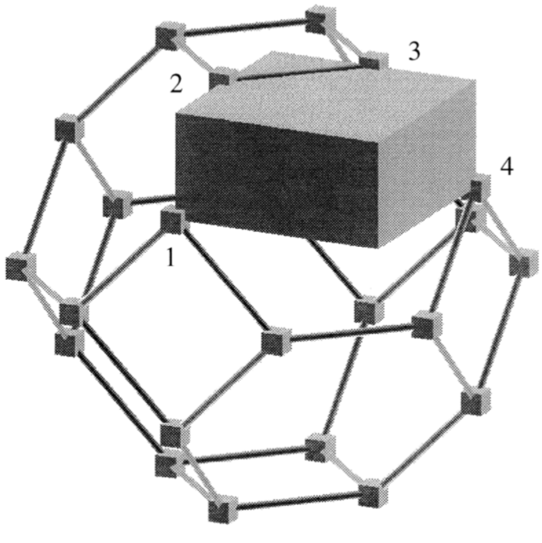

Figure 2.4: Approximated three-dimensional structure of metal foam. [45]

$$k_{eff} = \frac{\sqrt{2}}{2(R_A + R_B + R_C + R_D)} \tag{2.32a}$$

$$R_A = \frac{4\lambda}{(2e^2 + \pi\lambda(1-e))k_s + (4 - 2e^2 - \pi\lambda(1-e))k_f} \tag{2.32b}$$

$$R_B = \frac{(e-2\lambda)^2}{(e-2\lambda)e^2 k_s + (2e - 4\lambda - (e-2\lambda)e^2)k_f} \tag{2.32c}$$

$$R_C = \frac{(\sqrt{2}-2e)^2}{2\pi\lambda^2(1-2e\sqrt{2})k_s + 2(\sqrt{2}-2e-\pi\lambda^2(1-2e\sqrt{2}))k_f} \tag{2.32d}$$

$$R_D = \frac{2e}{e^2 k_s + (4-e^2)k_f} \tag{2.32e}$$

$$\lambda = \sqrt{\frac{\sqrt{2}(2-(5/8)e^3\sqrt{2}-2\gamma)}{\pi(3-4e\sqrt{2}-e)}} \tag{2.32f}$$

$$e = 0.339 \tag{2.32g}$$

Two-temperature model

A local thermal non-equilibrium will be present by introducing a metal foam which has a higher thermal conductivity than the PCM. Hu and Patnaik [43] performed a two-temperature simulation. Two separate energy equations are used to account for the local non-thermal equilibrium (LTNE) between the metal foam and the PCM. The local heat transfer is represented by the interstitial heat transfer coefficient h_{sf} across the specific surface area A_{sf}.

$$\gamma \rho_f c_{p,f} \frac{\partial T_f}{\partial t} = \nabla(k_{f,eff} \nabla T_f) - \rho_f \gamma \Delta h_m \frac{\partial f_l}{\partial t} - h_{sf} A_{sf}(T_f - T_s) \tag{2.33a}$$

$$(1-\gamma)\rho_s c_{p,s} \frac{\partial T_s}{\partial t} = \nabla(k_{s,eff} \nabla T_s) - h_{sf} A_{sf}(T_s - T_f) \tag{2.33b}$$

Effective conductivities must be calculated for the foam $k_{s,eff}$ and the PCM $k_{f,eff}$. Hu and Patnaik [43] defined them by using the first order approximation (Equation 2.30) and the Progelhoff model (Equation 2.31). The calculation of $k_{f,eff}$ and $k_{s,eff}$ can also be done by setting $k_s = 0$ and $k_f = 0$ in Equation 2.32, respectively [47].

The determination of the interstitial heat transfer is important to estimate the heat transfer performance of the composite material. It is however difficult due to the complicated structure of the metal foam and the complex flow at pore scale

[47]. A simplification of the foam structure can be made, where the ligaments are considered as cylinders. The empirical correlations of Zhukauska for flow around a cylinder can then be used.

$$h_{sf} = \begin{cases} 0.76 Re^{0.4} Pr^{0.37} k_f/d_f & , 0 < Re \leq 40 \\ 0.52 Re^{0.5} Pr^{0.37} k_f/d_f & , 40 < Re \leq 1000 \\ 0.26 Re^{0.6} Pr^{0.37} k_f/d_f & , 1000 < Re \leq 20000 \end{cases} \tag{2.34}$$

Krishnan et al. [48] on the other hand, simplified the geometry to a packed bed of spherical particles. They used the forced convection correlation of Wakao and Kaguei [49], but assumed it to be approximately valid for the natural convection in the melting PCM. It is a correlation for the interstitial Nusselt number $Nu_{i,d}$, which uses the foam pore diameter as characteristic length. It covers a large range of Reynold numbers and it becomes a constant value for the case where only diffusion occurs ($Re \rightarrow 0$).

$$Nu_{i,d} = 6(1-\gamma)[2 + 1.1 Re^{0.6} Pr^{1/3}] \tag{2.35}$$

Another way to estimate h_{sf} is by performing DNS. Hu and Patnaik [43] did this on the unit-cell level. The heat flux across the interface q_{fs} and the average temperatures of the foam $\overline{T_s}$ and PCM $\overline{T_f}$ were calculated. An interstitial heat transfer of 9.09 kW/m^{2}K was then obtained from these parameters.

$$h_{fs} = \frac{q_{fs}}{\overline{T_s} - \overline{T_f}} \tag{2.36}$$

Hu and Patnaik [43] compared volume averaged one-temperature and two-temperature simulations with direct simulations. They concluded that both volume averaged simulations results in reasonable predictions of the heat transfer during phase change. This prediction is however only valid when the effective thermal conductivity was calculated with the Progelhoff model (Equation 2.31), since the first order approximation results in an overestimation. Both volume averaged simulations have approximately the same results. If only the charging and/or discharging time is needed, a one-temperature simulation could be preferred due to its higher simplicity.

In conclusion, to model a porous material impregnated in PCM the effective thermal conductivity is a key parameter. Several correlations are listed in Section 2.2.4. If however a two-temperature simulation is performed to incorporate the LTNE, the interstitial heat transfer between foam and PCM is also needed. This however increases the complexity of the model.

Chapter 3

Thermal battery

The goal of this master dissertation is to model a cold storage with metal foam enhanced PCM. Two thermal batteries have previously been constructed by a master student within the framework of his master dissertation [50]. One with metal foam in the PCM channels and one without metal foam. These thermal batteries are modelled and compared with experimental results. A description of the construction of the thermal batteries and the employed measurement procedure follows.

3.1 Construction

A schematic of the thermal battery is shown in Figure 3.1a. It consists of four aluminium profiles with lengths of 806 mm. They are placed next to each other and welded together. HTF flows through the profiles to cool down the PCM. Collectors are added at the extremities of the profiles to connect them in series. Walls are placed inside the placed inside the collectors to guide the HTF flow to the next profile. The flow direction in each profile is depicted in Figure 3.1a. Two nipples are added to allow entrance and exit of the HTF.

The cross-section of the aluminium profiles is illustrated in Figure 3.1b. Two types of channels are present. The open B channels which allow through flow of a HTF to charge the thermal battery. The charging is done by cooling the PCM enclosed in the A channels. Open cell aluminium metal foam pieces are placed in the A channels of one thermal battery before adding the PCM. This is the

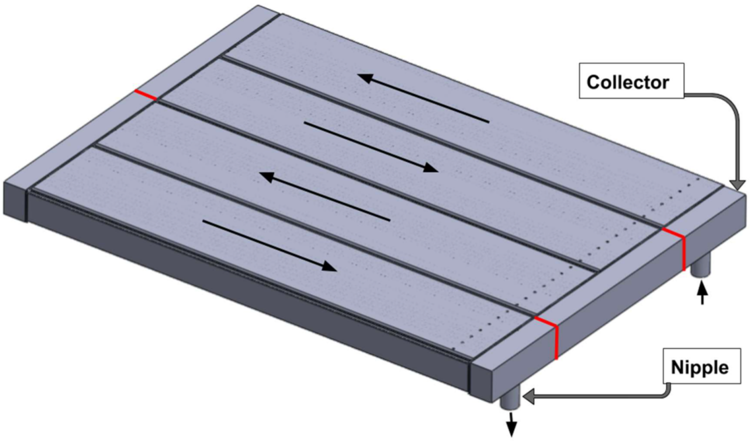

(a) Schematic of the thermal battery.

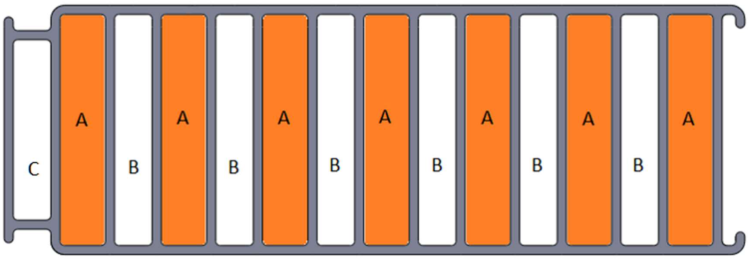

(b) Cross-section of the aluminium profiles used in the thermal battery.

Figure 3.1: Thermal battery constructed by Michiel Corryn [50].

difference between the two produced thermal batteries. The aluminium foam is produced by Alhedron and has a porosity of 93 %. The A and B channels have dimensions of 50 x 10 mm^2 and 50 x 8.3 mm^2, respectively. The geometrical dimensions are summarised in Table 3.1.

Table 3.1: Geometrical dimensions of the aluminium profiles used in the thermal batteries [50].

Dimension	Symbol	value
Length channels [mm]	L	806
Height channels [mm]	h_{htf}	50
Width HTF channels [mm]	w_{htf}	8.3
Width PCM channels [mm]	w_{pcm}	10

As mentioned in the previous paragraph, a HTF fluid is used during the charging process of the thermal batteries. The liquid has to possess a low freezing temperature to avoid solidification of the HTF, which would clog the HTF channels. The chosen fluid is TEMPER -30 by Climalife. The full specifications of this material can be found in Appendix C.

Finally, a PCM is needed to fill the PCM channels. The organic PCM RT5HC by Rubitherm is chosen. Its melting range is situated between 5 °C and 6 °C. The heat storage capacity is 250 kJ/kg. This is a combination of latent and sensible heat in a temperature range of -2 °C to 13 °C. The sensible heat is stored by lowering the temperature from 13 °C to -2 °C and the latent heat is stored by the phase change. By extracting the sensible part, a latent heat of fusion of 220 kJ/kg is obtained. The full specifications of the PCM is listed in Appendix C. This concludes the description of the main parts of the thermal batteries.

3.2 Measurement procedure

Experiments were performed on the thermal batteries described in the previous section [50]. The experimental setup and the locations of the temperature measurements are described.

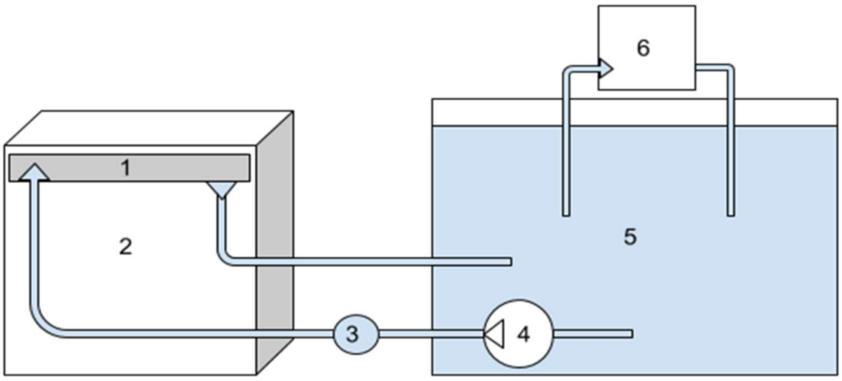

Figure 3.2: Schematic representation of the experimental setup [50].

The experimental setup is presented schematically in Figure 3.2. The thermal battery (1) is placed in an insulated container (2). The HTF is contained in a reservoir (5) and pre-chilled to -15 °C by the cooling cycle (6). The HTF in the hoses is pre-chilled by short circuiting them. After connection of the hoses to the thermal battery, the pump (4) is started to enable HTF flow through the battery. A flowmeter (3) is used to measure the mass flow rate during during the charging process.

Temperature measurements are done at several locations to evaluate the charging process. The HTF temperature is measured before leaving the reservoir. This is also the case for the HTF returning to the reservoir. This gives us the inlet and outlet HTF temperatures. Two additional temperature measurements are performed inside the reservoir.

The phase change process is estimated by measuring the temperatures inside the PCM channels. This is done by installing aluminium thermowells in the thermal battery. They are placed in the middle of the central PCM of each aluminium profile, which is illustrated in Figure 3.3. A centrally located PCM temperature is thus measured.

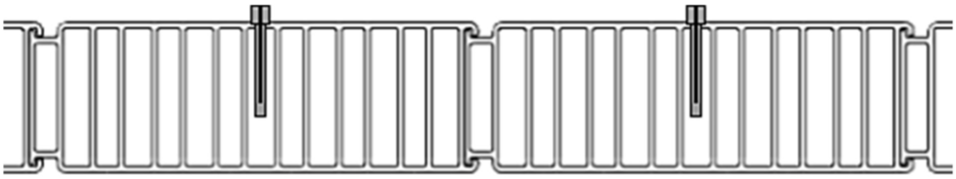

Figure 3.3: Cross-section of the profiles illustrating the positions of the thermowells [50].

Chapter 4

Models

4.1 Modelled geometry

The geometry of the thermal battery described in Chapter 3.1a is simplified to perform the numerical calculations. The aluminium profiles have six HTF channels and seven PCM channels (Figure 3.1b). First an assumption about the HTF flow distribution is made. An evenly distributed flow is considered. Secondly, a symmetrical heat transfer process is presumed. This makes it possible to represent the total heat transfer process in one profile by modelling one half PCM channel and one half HTF channel. This results in the geometry depicted in the Figure 4.1, which will be used to model one aluminium profile.

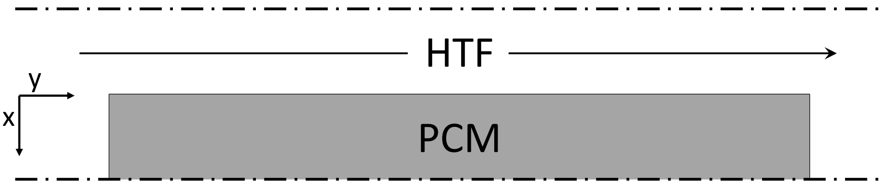

Figure 4.1: Geometry used to model the charging process in one aluminium profile.

The thermal battery consists of four profiles connected in series by collector bends (Figure 3.1a). A third assumption is done to model the complete thermal battery. The collector bends are neglected and the entire battery is modelled as four channels placed in-line after each other. The used models are described in the following sections.

4.2 Effectiveness-NTU model

The profiles in the thermal battery contain HTF and PCM. A convective heat transfer between the HTF and PCM container is present which drives the charging process in the thermal battery. Sensible and latent heat will be stored in the PCM. The Stefan problem [18] offers a first order approximation of the phase change problem. It however only incorporates the latent energy storage. A model similar to the Stefan problem [18] is first derived.

During the solidification process, the distance between the HTF and the phase change front d_{pcm} grows. The growth rate $\frac{d_{pcm}}{dt}$ of the solid PCM layer is expressed using following equation.

$$\frac{d\,d_{pcm}}{dt} = \frac{q}{\Delta h_m \rho_{l,pcm} A_R} \tag{4.1}$$

It is a function of the heat transfer rate q, the latent heat of fusion Δh_m, the liquid density $\rho_{l,pcm}$ and the heat transferring area A_R. The heat transfer rate q needs to be determined.

The thermal battery can be modelled as a a heat exchanger with the PCM acting as a fixed heat source at its phase change temperature T_{pcm}. The effectiveness-NTU method explained in Appendix B can be used to calculate the heat transfer rate between HTF and PCM. The calculated heat transfer rate is constant throughout the profile. The number of transfer units (NTU) are needed, which are a function of the total thermal resistance R_{tot} between the HTF and the phase change front.

The total thermal resistance R_{tot} is a series of thermal resistances. These are the convective resistance of the HTF R_{conv} and the conductive resistance of the solid PCM layer R_{pcm}. The conductive resistance of the aluminium wall R_{al} is small compared to the other an it is neglected. The heat transfer area is A_R is 50 x 806 mm^2 (Table 3.1). The thermal conductivity of the PCM k_{pcm} is 0.2 W/mK.

The calculation of the convection coefficient h_{conv} is depicted in Appendix A.

$$R_{tot} = R_{pcm} + R_{conv} + R_{al} \approx \frac{d_{pcm}}{k_{pcm} A_R} + \frac{1}{h_{conv} A_R} \tag{4.2}$$

The distance to the phase change front d_{pcm} grows during the solidification. This results in a time dependent total thermal resistance (Equation 4.2). The heat transfer rate is thus also time dependent. The growth rate (Equation 4.1) is thus a function of d_{pcm} and time.

$$\frac{d\, d_{pcm}}{dt} = G(d_{pcm}, t) \tag{4.3}$$

The growth rate expression is an ordinary differential equation (ODE). The equation is solved until the PCM is completely solidified. This is the case when the solid PCM layer thickness is equal to half the PCM channel width (Section 4.1).

The outlet temperature of the HTF of a profile at every time step is calculated by rearranging the effectiveness ε (Equation B.5).

$$T_{out} = T_{in} - \varepsilon(T_{in} - T_{pcm}) \tag{4.4}$$

The above derived equations are valid for one aluminium profile of the thermal battery. The calculations are repeated three times by using the outlet temperature of the previous profile as the new inlet temperature. The complete thermal battery is modelled.

$$T_{in,j} = T_{out,j-1} \quad \text{j= 2...4} \tag{4.5}$$

According to the datasheets of the RT5HC PCM (Appendix C), the phase change occurs in a range between 5 °C and 6 °C. A fixed phase change temperature is however needed in the derived model. The T_{pcm} value is fixed at 5.5 °C. The HTF inlet temperature is set to -13 °C.

The convection in the liquid part of the PCM is neglected in the model derived above. The freezing process is modelled which states a low influence of the convection in the liquid PCM due to the small temperature gradient between the solid and liquid part [42]. The convection in the PCM is thus altogether ignored in this model.

This effectiveness-NTU approach of the phase change problem is implemented numerically in Python. The code can be found in Appendix D. The convergence and the sensitivity analysis is done in the following sections.

4.2.1 Convergence

As explained in previous section, the calculations are executed with one control volume (CV) per profile. It was investigated if increasing the number of CV gives different results. The criteria for convergence is the maximum difference in outlet temperature per time step. When two CV were used instead of one, the maximum difference was 0.0016 K. This indicates that increasing the number of CV has no significant effect on the results.

The same procedure was done to determine the time convergence. This resulted in a difference of 0.0019 K when the time step was decreased from 1 s to 0.1 s. A time step of 1 second thus delivers enough accuracy.

4.2.2 Sensitivity analysis

A sensitivity analysis is performed to evaluate the influence of several parameters on the results. This allows us to determine which parameters have a significant influence on the phase change problem. An estimation of the error can also be made from this data. The influence on the total freezing time is studied to evaluate the influence on the phase change problem. The parameters were all increased by 1% to determine their sensitivity. The investigated parameters are listed in Table 4.1 together with their sensitivity. The estimated deviations and corresponding estimated errors are also listed.

Table 4.1: The sensitivity, estimated deviation and estimated error of the parameters in the sensitivity analysis of the effectiveness-NTU model.

Parameter	Symbol	Sensitivity	Estimated deviation	Estimated error
Conductivity PCM	k_{pcm}	-0.84%	5%	-4.18% (5%)
Convection HTF	h_{conv}	-0.13%	10%	-1.31% (10%)
Mass flow rate	$\dot{m}$	-0.078%	2%	-0.016% (2%)
Specific heat capacity HTF	c_{htf}	-0.078%	5%	-0.39% (5%)
Latent heat of fusion PCM	Δh_m	0.99%	7.5%	7.44% (7.5%)
Temperature inlet HTF	T_{in}	-	1K	5.72% (1 K)
Temperature PCM	T_{pcm}	-	0.5 K	-2.25% (0.5 K)

The NTU defines the effectiveness of the heat exchanger as can be seen in Equation B.3 and will thus have an influence on the total freezing time. The NTU is amongst other defined by the total thermal resistance between the HTF and the phase change front (Equation B.4). The total thermal resistance is the sum of the convective resistance R_{conv} and the conduction in the solid PCM layer R_{pcm} (Equation 4.2). Their influence will be investigated first.

Increasing the thermal conductivity and convection coefficient both results in a decrease in freezing time. This was expected since they both lower the total thermal resistance accompanied by the corresponding increase in NTU. The influence of the conductivity is about 6.5 times higher. This implicates that the conduction is the dominant heat transfer mode. This influence is however not constant in time. At the start of the heat exchange, there is no solid PCM layer and thus no conductive thermal resistance. The influence of the conductive resistance then increases during solidification due to the growing distance to the phase change front. The convective resistance stays constant during the entire process. A plot of this trend is shown in Figure 4.2. It can clearly be seen that the total resistance increases with time which results in a lower effectiveness while the PCM layer grows.

The NTU also depends on the mass flow through the HTF channel $\dot{m}_{htf}$ and the specific heat capacity of the HTF c_{htf}. From the results seen in Table 4.1, it can be concluded that they both have an insignificant effect on the heat transfer process.

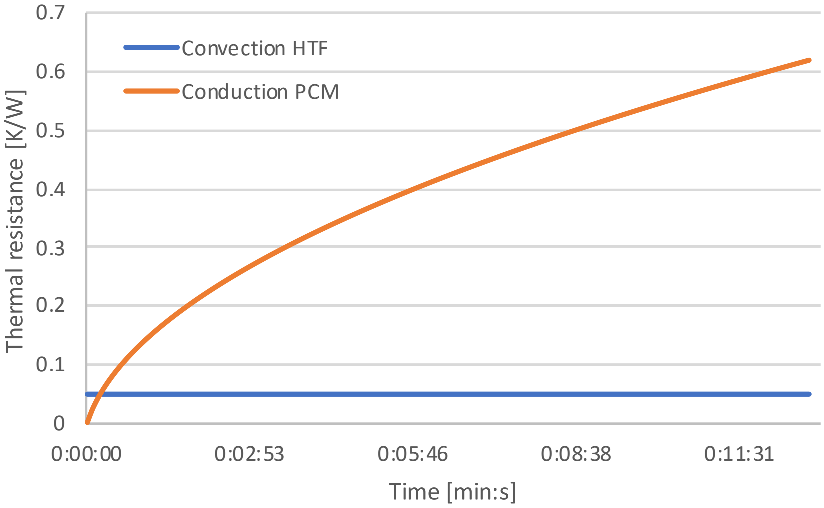

Figure 4.2: Evolution of the thermal resistances during the solidification.

The growth rate of the solid PCM layer is defined by the latent heat of fusion. A larger value states that more energy is needed to complete the solidification. This results in an increased freezing time of 0.99%. The increased freezing time is however not disadvantageous if the increased energy storage is taken into account.

The maximum heat transfer rate is proportional to the temperature difference between the PCM temperature and the HTF inlet temperature (Equation B.2). The actual heat transfer is also affected as seen in Equation B.1. By increasing T_{in} by 1 K the freezing time is increased by 5.72%. The increment is expected since a lower temperature difference is applied. The PCM temperature is increased by 0.5 K which is the top of the congealing area stipulated in the technical datasheet (Appendix C). The resulting solidification time is decreased by 2.2%, due to the larger temperature difference.This is appointed to the uncertainty of the phase change temperature and cannot be adapted in real life. It can thus be concluded that decreasing the HTF temperature is favourable for the charging efficiency of the thermal battery.

An estimation of the error of the effectiveness-NTU model is done by estimating the deviations of the different parameters to the assumed or measured values. The Gnielinski correlation [51] of the convection coefficient has an error margin of 10%. A measuring error of 5% is assumed for the thermal conductivity of the PCM and for the specific heat capacity of the HTF. The accuracy of the mass flow rate measurement is 0.2%. An error of 7.5% on the latent heat of fusion is stated in the datasheets (Appendix C). The different parameters are independent of each other. The total error X_{tot} can be expressed with the equation below. This results in an error of 11% of the effectiveness-NTU model.

$$X_{tot} = \sqrt{\sum X_i^2} \tag{4.6}$$

The model derived above uses several simplifications. Firstly, the phase change process in the PCM occurs at a fixed solidification temperature. The RT5HC PCM however has a congealing range of 1 °C (Appendix C). Using a single solidification temperatures results in an estimated error of 2.25 % (Table 4.1). Including the solidification range should thus improve the accuracy of the model. Secondly, only the latent energy storage is modelled by assuming a constant temperature in the PCM. The solid parts of the PCM however experience a temperature drop after solidification. This stores sensible heat and the PCM closer to the HTF will have a lower temperature than in the middle. In thermal storage applications, the PCM will not be at the phase change temperature prior to charging and sensible heat is also stored before the solidification process. The solidification range and sensible heat should be included to have a better representation of the charging process.

4.3 Enthalpy model

To have a more accurate representation of the phase change process, the sensible heat transfer needs to be taken into account. This can be done by using the enthalpy method [26]. A conduction governed heat transfer is considered. The energy conservation can be expressed in terms of total volumetric enthalpy temperature.

$$\frac{\partial H}{\partial t} = \nabla(k\nabla T) \tag{4.7}$$

4.3.1 Discretisation heat transfer equations

The geometry seen in Figure 4.1 is discretised to form a two-dimensional grid. A schematic of the resulting grid is illustrated in Figure 4.3. This discretisation will result in a system of equations which then is solved for each time step using a numerical scheme. A detailed derivation of the different types of CVs follows hereunder.

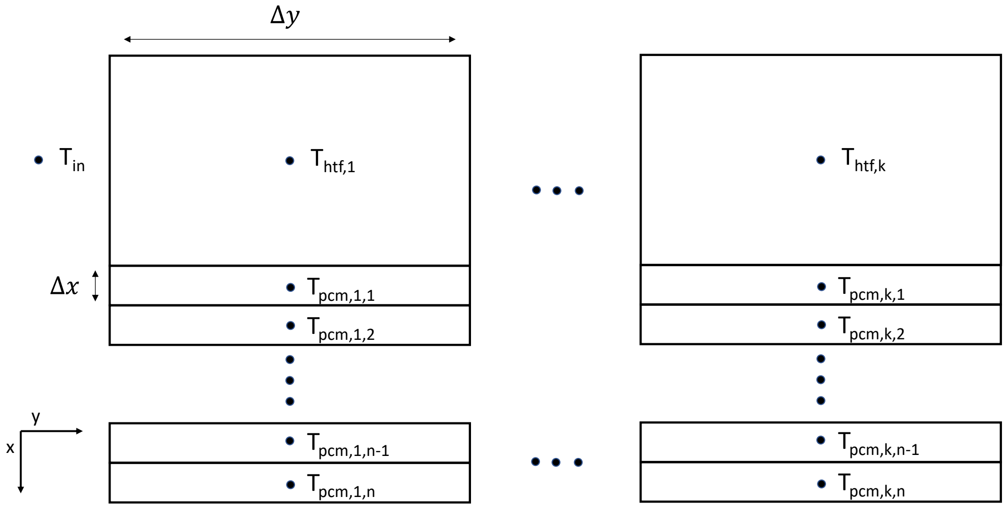

Figure 4.3: Schematic of control volumes used in the enthalpy model.

Generic PCM control volumes

The phase change problem is governed by the conduction in the PCM. The effects of convection in the liquid part of the PCM are neglected. During the solidification process this is an appropriate assumption, due to the small temperature gradients in the liquid PCM [42]. The conservation of energy can then be written as follows.

$$\frac{\partial H}{\partial t} = \nabla(k\nabla T) \tag{4.8}$$

The total enthalpy H consists of the sensible and latent enthalpy. Δh_m is the latent heat of fusion and f the liquid fraction. Together with the density ρ it represents the latent enthalpy.

$$H = \int_{T_{ref}}^{T} \rho c dT + \rho f \Delta h_m \tag{4.9}$$

The density and specific heat capacity are assumed constant. Substituting the above in Equation 4.8 results in a conservation of energy expression as a function of temperature [26].

$$\rho c \frac{\partial T}{\partial t} = \nabla(k \nabla T) + S \tag{4.10}$$

The source term S is defined as the change in latent enthalpy with respect to time.

$$S = -\delta H \frac{\partial f}{\partial t} \tag{4.11}$$

The reference temperature T_{ref} is set to 0 K and constant thermo-physical properties for both phases are assumed. This leads to following difference between solid and liquid enthalpies.

$$\delta H = \rho \Delta h_m \tag{4.12}$$

The heat transfer is in the PCM is assumed to be one-dimensional, which results in following expression.

$$\rho_{pcm} c_{pcm} \frac{\partial T_{pcm}}{\partial t} = \frac{\partial}{\partial x}\left(k_{pcm} \frac{\partial T_{pcm}}{\partial x}\right) - \delta H \frac{\partial f}{\partial t} \tag{4.13}$$

This one-dimensional conservation of energy is then discretised using a fully implicit finite volume method. The finite volume equations are obtained by integrating Equation 4.13 over each control volume [52]. A detailed schematic of the control volumes of three neighbouring points is shown in Figure 4.4 The PCM subscripts are dropped in the rest of the derivations.

First the left hand side is discretised in time and space. T_p and T_{old} represent the new and old temperature values, respectively.

$$\rho c \int_{p-1}^{p+1} \int_{t}^{t+\Delta t} \frac{\partial T}{\partial t} dt dx = \rho c \Delta x (T_p - T_{old}) \tag{4.14}$$

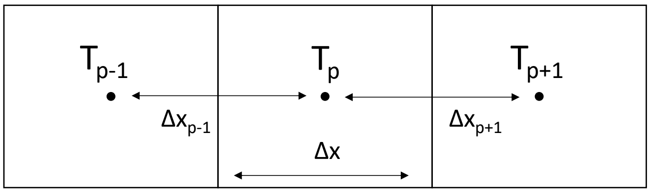

Figure 4.4: Three neighbouring control volumes of the PCM.

The first term of the right hand side is integrated over the control volumes. Finite difference is used to approximate the gradient $k\frac{\partial T}{\partial x}$.

$$\int_{t}^{t+\Delta t}\int_{p-1}^{p+1}\frac{\partial}{\partial x}\left(k\frac{\partial T}{\partial x}\right)dxdt = \int_{t}^{t+\Delta t}\left[\frac{k_{p+1}(T_{p+1}-T_p)}{\Delta x_{p+1}}-\frac{k_{p-1}(T_p-T_{p-1})}{\Delta x_{p-1}}\right]dt \quad (4.15)$$

An assumption about the evolution of the temperature in the three nodes (p-1, p and p+1) is needed to perform the integration from t to $t+\Delta t$. By using a fully implicit discretisation scheme each node temperature is equal to the new node temperature value for t to $t+\Delta t$.

$$\int_{t}^{t+\Delta t} T_{p-1,\,p,\,p+1}dt = T_{p-1,\,p,\,p+1}\Delta t \quad (4.16)$$

By substituting this temperature evolution in Equation 4.15 the finite difference time discretisation is expressed as follows.

$$\int_{t}^{t+\Delta t}\left[\frac{k_{p+1}(T_{p+1}-T_p)}{\Delta x_{p+1}}-\frac{k_{p-1}(T_p-T_{p-1})}{\Delta x_{p-1}}\right]dt = \left[\frac{k_{p+1}(T_{p+1}-T_p)}{\Delta x_{p}}-\frac{k_{p-1}(T_p-T_{p-1})}{\Delta x_{p-1}}\right]\Delta t \quad (4.17)$$

The thermo-physical properties are assumed constant and equal in both phases. Each node also has the same dimension Δx. This simplifies Equation 4.17.

$$\left[\frac{k_{p+1}(T_{p+1}-T_p)}{\Delta x_{p+1}}-\frac{k_{p-1}(T_p-T_{p-1})}{\Delta x_{p-1}}\right]\Delta t = \frac{k}{\Delta x}\left[T_{p+1}-2T_p+T_{p-1}\right]\Delta t \quad (4.18)$$

The second term of the right hand side is discretised in the same way as the left hand side.

$$-\delta H \int_{p-1}^{p+1} \int_{t}^{t+\Delta t} \frac{\partial f}{\partial t} dt dx = -\delta H \Delta x (f_p - f_p^{old}) \tag{4.19}$$

The equations above have only been integrated in the x-direction of the CVs. To perform a three dimensional integration all equations are multiplied by the height h_{htf} and the length Δy of the CVs. This is the heat transferring area between neighbouring CVs ($A_R = \Delta y \, h_{htf}$). The volume of each PCM CV is constant ($V_{pcm} = \Delta x \, \Delta y \, h_{htf}$). By combining and rearranging Equation 4.14, 4.17 and 4.19 the point form of the generic cells is obtained.

$$a_p T_p = \sum_{nb} a_{nb} T_{nb} + b_p T_p^{old} + V_{pcm} \delta H (f_p^{old} - f_p) \tag{4.20a}$$

$$a_{nb} = \frac{A_R \, k_{pcm}}{\Delta x} \tag{4.20b}$$

$$b_p = \frac{V_{pcm} \, \rho_{pcm} \, c_{pcm}}{\Delta t} \tag{4.20c}$$

$$a_p = \sum_{nb} a_{nb} + b_p \tag{4.20d}$$

Heat transfer fluid

The HTF flow is assumed inviscid, incompressible and one-dimensional. These assumptions make it possible to decouple the equations of motion from the energy equations. The momentum equations can also be ignored. The conduction in the direction perpendicular to the flow is ignored in the HTF as in the PCM.

The conservation of energy in a HTF cell can be written as.

$$V_{htf} \rho_{htf} c_{htf} \frac{\partial T_{htf}}{\partial t} = -c_{htf} \frac{\dot{m}_{htf}}{2} \frac{\partial T_{htf}}{\partial y} \Delta y + Q_{htf} \tag{4.21}$$

Heat is transferred in two directions. The HTF mass flow $\dot{m}_{htf}$ and specific heat capacity determine the heat transfer between two HTF CVs in the flow direction. Q_{htf} is the heat transfer rate between the HTF control volume and the first adjacent PCM control volume. It is defined by the convective heat transfer of the HTF and the conduction through the PCM. The calculation of the convection coefficient h_{conv} is explained in Appendix A. V_{htf} is the volume of the HTF control volume ($V_{htf} = \Delta y\, h_{htf}\, \frac{w_{htf}}{2}$).

$$Q_{htf} = \frac{T_{pcm,1} - T_{htf}}{R_{conv} + R_{pcm}} \tag{4.22a}$$

$$R_{conv} = \frac{1}{h_{conv}\, A_R} \tag{4.22b}$$

$$R_{pcm} = \frac{l_{pcm}}{k_{pcm}\, A_R} \tag{4.22c}$$

A_R is the heat transferring area between the two CVs ($A_R = \Delta y\, h_{htf}$). The length between the wall and the first PCM node l_{pcm} is equal to half of the node length $\Delta x/2$. A detailed schematic of the involved CVs is illustrated in Figure 4.5. Finite difference is then used to discretise Equation 4.21.

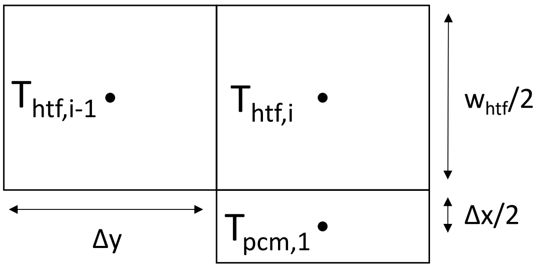

Figure 4.5: HTF control volumes with adjacent PCM control volume.

$$\rho_{htf} c_{htf} V_{htf} \frac{T_{htf,i} - T^{old}_{htf,i}}{\Delta t} = \frac{\dot{m}_{htf}}{2} c_{htf} (T_{htf,i-1} - T_{htf,i}) + \frac{T_{pcm,1} - T_{htf,i}}{R_{conv} + R_{pcm}} \tag{4.23}$$

$T_{htf,i-1}$ is the temperature of the upstream HTF node. For the first control volume $T_{htf,i-1} = T_{in}$, where T_{in} is the temperature of the HTF before entering the channel. T^{old}_{htf} is the value of the previous time step.

Rearranging the equation results in following point form.

$$a_{p,htf} T_{htf,i} = a_{nb,pcm} T_{pcm,1} + b_{p,htf} T^{old}_{htf,i} + a_{nb,htf} T_{htf,i-1} \tag{4.24a}$$

$$a_{nb,htf} = \frac{\dot{m}_{htf}\, c_{htf}}{2} \tag{4.24b}$$

$$a_{nb,pcm} = (R_{conv} + R_{pcm})^{-1} \tag{4.24c}$$

$$b_{p,htf} = \frac{\rho_{htf}\, c_{htf}\, V_{htf}}{\Delta t} \tag{4.24d}$$

$$a_{p,htf} = a_{nb,pcm} + a_{nb,htf} + b_{p,htf} \tag{4.24e}$$

First PCM control volume

The change in temperature per time step in the PCM CV adjacent to the HTF CV is written as a function of the heat transfer rates from the HTF control volume and the second PCM control volume. The discretised form is written as follows.

$$\begin{aligned} V_{pcm}\rho_{pcm}c_{pcm}(T_{pcm,1} - T^{old}_{pcm,1}) = \\ \frac{T_{pcm,2} - T_{pcm,1}}{R_{pcm,1}} + \frac{T_{htf} - T_{pcm}}{R_{conv} + R_{pcm}} + V_{pcm}\delta H(f - f^{old}) \end{aligned} \tag{4.25}$$

This equation is written in its point form.

$$a_{p,1}T_{pcm,1} = a_{nb,pcm}T_{htf} + a_{nb}T_{pcm,2} + b_pT^{old}_{pcm,1} + V_{pcm}\delta H(f_p - f^{old}_p) \tag{4.26a}$$

$$a_{nb} = \frac{k_{pcm}A_R}{\Delta x} \tag{4.26b}$$

$$b_p = \frac{\rho_{pcm}\, c_{pcm}\, V_{pcm}}{\Delta t} \tag{4.26c}$$

$$a_{p,1} = b_p + a_{nb} \tag{4.26d}$$

Last PCM control volume

Due to the symmetry assumption, no heat is transferred from the middle of the PCM channel to the last node point. This is formulated by setting $T_{p+1} = T_p$. This leads to the following point form.

$$a_{p,l}T_p = a_{p-1}T_{p-1} + b_pT^{old}_p + V_{pcm}\delta H(f_p - f^{old}_p) \tag{4.27a}$$

$$a_{nb} = \frac{k_{pcm}\, A_R}{\Delta x} \tag{4.27b}$$

$$b_p = \frac{\rho_{pcm}\, c_{pcm}\, V_{pcm}}{\Delta t} \tag{4.27c}$$

$$a_{p,l} = b_p + a_{nb} \tag{4.27d}$$

4.3.2 Liquid fraction update

In order to have a correct representation of the phase change an appropriate liquid fraction update is needed. According to the technical specifications of the PCM (Appendix C), the phase change occurs in a temperature range between 5 °C and 6 °C. A mushy zone will be present in this temperature range. The liquid fraction will be between 0 and 1. The liquid fraction is written as a linear function of temperature.

$$F(T) = \frac{T - T_s}{T_l - T_s} \tag{4.28}$$

The source base method of Voller and Swaminathan [32], which combine the advantages of the apparent heat capacity method and the source based methods, is used. The iterative scheme is written as.

$$a_p T_p^{m+1} = \sum_{nb} a_{nb} T_{nb}^{m+1} + b_p T_p^{old} + \Delta x \delta H (f_p^{old} - f_p^{m+1}) \tag{4.29}$$

All temperatures are evaluated at iteration level m+1 since a fully implicit method is used. The liquid fraction is also evaluated at iteration level m+1. By using a truncated Taylor series expansion on f_p^{m+1}, we get.

$$f_p^{m+1} = f_p^m + \frac{dF}{dT}[T_p^{m+1} - F^{-1}(f_p^m)] \tag{4.30a}$$

$$\frac{dF}{dT} = \frac{1}{T_l - T_s} = 1 \tag{4.30b}$$

$$F^{-1}(f) = f(T_l - T_s) + T_s = f + 278.15 \tag{4.30c}$$

The derivative dF/dT is evaluated at f_p^m. The source term can then be written in a linearised form.

$$S = S_p T_p^{m+1} + S_c \tag{4.31a}$$

$$S_p = -\delta H \frac{dF}{dT} \Delta x \tag{4.31b}$$

$$S_c = \delta H (f_p^{old} - f_p^m) \delta x + \delta H_p \frac{dF}{dT} F^{-1}(f_p^m) \delta x \tag{4.31c}$$

This results in following iterative scheme.

$$(a_p - S_p)T_p^{m+1} = \sum_{nb} a_{nb} T_{nb}^{m+1} + b_p T_p^{old} + S_c \tag{4.32}$$

Following solution procedure is used per time step to solve the iterative scheme.

1. Initialise each time step by setting $f^0 = f^{old}$, where f^{old} is the liquid fraction of the previous time step.
2. Calculate the discretisation coefficients, dF/dT, S_p and S_c. The temperature field T^{m+1} can then be solved using Equation 4.32.
3. Perform a liquid fraction update by using Equation 4.30a in combination with following under- and overshoot correction.

$$f^{m+1} = \begin{cases} 1 & , f^{m+1} > 1 \\ 0 & , f^{m+1} < 0 \end{cases} \tag{4.33}$$

4. Repeat steps 2 and 3 until convergence is achieved.

A smooth transition from a fully liquid state to a mushy state is acquired by using a different liquid fraction update for nodes with a liquid fraction of 1. The correction for these nodes is given by following formula. A is the linear term in the inverse function of the liquid fraction $F^{-1}(f) = Af + B$.

$$f_p^{m+1} = f_p^m + \lambda\Delta \tag{4.34a}$$

$$\Delta = \frac{a_p(T_p^{m+1} - F^{-1}(f_p^m)}{V_{pcm}\delta H_p^{m+1} + a_p A} \tag{4.34b}$$

4.3.3 Matrix form of system of equations

The system of equations derived above can be written as a tridiagonal matrix instead of its point forms. The solution of this matrix represents the temperature field at iteration level m+1 of one slice perpendicular to the direction of the HTF flow (Figure 4.3). There are one HTF and n PCM CVs. When convergence is achieved for a time step. The temperature field of the downstream slice is solved using the HTF temperature of the upstream slice $T_{htf,i-1}$. This is done for the entire profile and the procedure is repeated for next time step.

$$A \cdot T_i^{m+1} = B \cdot T_i^{old} + C$$

$$A = \begin{bmatrix} a_{p,htf} & -a_{nb,pcm} & & & & \\ -a_{nb,pcm} & a_{p,1} - S_{p,1} & -a_{nb} & & & \\ & -a_{nb} & a_{p,2} - S_{p,2} & -a_{nb} & & \\ & & \ddots & \ddots & \ddots & \\ & & & -a_{nb} & a_p - S_{p,n-1} & -a_{nb} \\ & & & & -a_{nb} & a_{p,n} \end{bmatrix} \tag{4.35}$$

$$B = \begin{bmatrix} b_{p,htf} & & & \\ & b_p & & \\ & & \ddots & \\ & & & b_p \end{bmatrix}, C = \begin{bmatrix} a_{nb,htf} T_{htf,i-1} \\ S_{c,1} \\ \vdots \\ S_{c,n} \end{bmatrix}, T_i = \begin{bmatrix} T_{htf,i} \\ T_{pcm,1,i} \\ \vdots \\ T_{pcm,n,i} \end{bmatrix}$$

This solution procedure is implemented numerically using Python. The code can be found in Appendix D

4.3.4 Conservation of energy

The enthalpy model is verified by checking the conservation of energy. The first law of thermodynamics states that the change in internal energy U of a system equals the energy E supplied to the system.

$$dU = dE \tag{4.36}$$

The energy extracted per time step due to the HTF flow through the system can be written in function of the the mass flow $\frac{m_{htf}}{2}$, the inlet enthalpy h_{in} and the outlet enthalpy h_{out}. No phase change occurs and the thermo-physical properties are constant. The HTF has constant thermo-physical properties and there is no phase change. The difference in enthalpy is thus proportional to the temperature difference between the system inlet and outlet.

$$\frac{dE}{dt} = \frac{\dot{m}_{htf}}{2}(h_{in} - h_{out}) = \frac{\dot{m}_{htf}}{2} c_{htf}(T_{in} - T_{out}) \tag{4.37}$$

The change in internal energy per time step $\frac{dU}{dt}$ of the system is equal to the change in total enthalpy $\frac{dH}{dt}$. The HTF enthalpy difference ΔH_{htf} is the change in sensible enthalpy. If a phase change takes place, the PCM enthalpy difference ΔH_{pcm} also includes latent enthalpy which is proportional to the difference in liquid fraction f.

$$\frac{dU}{dt} = \frac{dH}{dt} = \sum \frac{\Delta H_{htf}}{\Delta t} + \sum \frac{\Delta H_{pcm}}{\Delta t} \tag{4.38a}$$

$$\Delta H_{htf} = V_{htf} \rho_{htf} c_{htf} (T_{htf}^{t+\Delta t} - T_{htf}^{t}) \tag{4.38b}$$

$$\Delta H_{pcm} = V_{pcm} \rho_{pcm} \Big[c_{pcm} (T_{pcm}^{t+\Delta t} - T_{pcm}^{t}) + \Delta h_m (f_{pcm}^{t+\Delta t} - f_{pcm}^{t}) \Big] \tag{4.38c}$$

The model is then valid if following statement holds true.

$$\frac{dE}{dt} - \frac{dH}{dt} = 0 \tag{4.39}$$

The resulting order of magnitude is 10^{-14}. The conservation of energy is thus satisfied in the enthalpy model.

4.3.5 Convergence

The convergence of the results was checked to determine the size of the CVs (Δx and Δy) and the time step Δt. The criteria for convergence used to define the dimensions of the grid are the difference in freezing time and the maximum difference in outlet temperature per time step.

Firstly, the convergence in the x-direction perpendicular to the flow direction is checked. The results on the freezing time and temperature difference are shown in Table 4.2. The difference is taken between the results of $n_{\Delta x}$ and $(n_{\Delta x} - 1)$ CVs. Increasing the number of CVs has no influence on the time needed to achieve complete solidification. There is however an influence on the outlet temperature. The accuracy of the thermocouples used in the experiments is 0.2 K [50]. When a temperature difference of approximately 0.1 K with the previous step is achieved convergence is obtained.

Table 4.2: Grid convergence in the x-direction

$n_{\Delta x}$	10	11	12	13	14	15
$\Delta t_{freeze}[s]$	0	0	0	0	0	0
$\Delta T_{out,max}[K]$	0.237	0.198	0.181	0.151	0.111	0.077

Convergence is achieved for 15 CVs the x-direction. Similar simulations were performed for the number of CVs in the y-direction (Table 4.3). Seven CVs are needed to obtain grid convergence. The resulting grid is displayed in Figure 4.6. The grid is not to scale.

Table 4.3: Grid convergence in the y-direction

$n_{\Delta y}$	5	6	7
Δt_{freeze} [s]	0	0	0
$\Delta T_{out,max}$ [K]	0.132	0.121	0.011

With the determined grid, the time convergence is then checked in the same manner. The results can be seen in Table 4.4. A time step of 0.5 seconds provides enough accuracy.

Table 4.4: Time convergence

Δt	1	0.5	0.25
Δt_{freeze} [s]	0	0	0
$\Delta T_{out,max}$ [K]	0.164	0.105	0.063

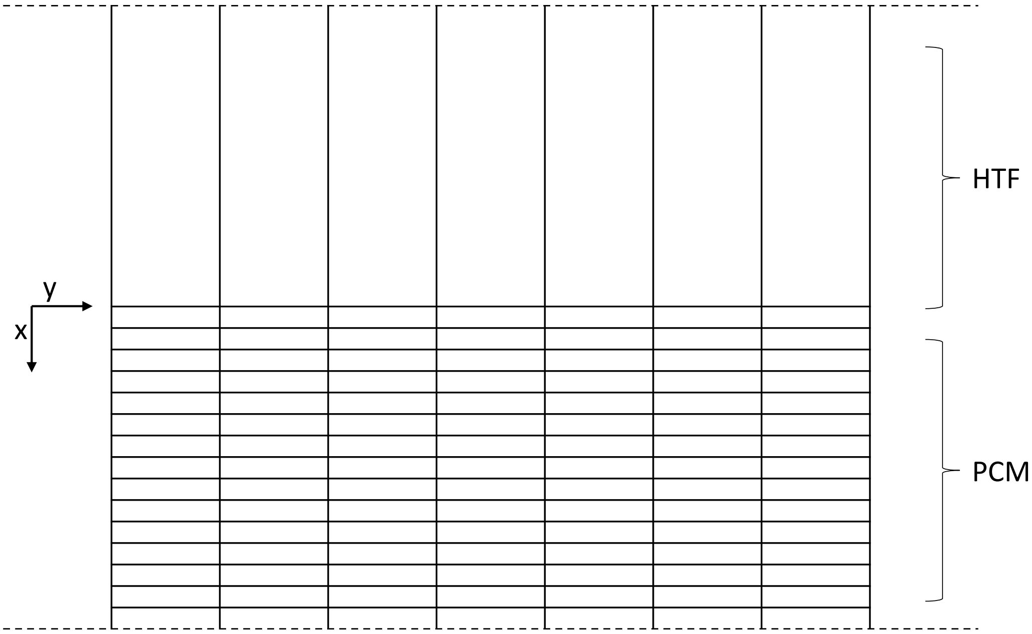

Figure 4.6: Grid used to model one channel in the enthalpy model.

4.3.6 Sensitivity analysis

A sensitivity analysis is also performed on the enthalpy model as was done for the effectiveness-NTU model (Section 4.2.2). The investigated parameters are listed in Table 4.5. The influence on the total freezing time is used to determine the sensitivities. The estimated deviations and corresponding errors are also included.

The charging process of the PCM is conduction controlled (Equation 4.8) and the heat transfer with the HTF happens through convection. The sensitivity of the PCM conductivity and the HTF convection is investigated first. Increasing them by 1% results in a decrease in freezing time. This was expected since they both increase the heat transfer. The influence of the conductivity is 6 times higher, which indicates it as the dominant heat transfer mode. This conclusion was also drawn in the previous sensitivity analysis (Section 4.2.2).

The mass flow rate and the specific heat capacity of the HTF determines the heat transfer in the flow direction. They both lower the freezing time, but the effect is insignificant. They are coupled with the convective heat transfer to the PCM, which also has an small sensitivity.

Table 4.5: Investigated parameters in sensitivity analysis enthalpy model with their errors.

Parameter	Symbol	Sensitivity	Estimated deviation	Estimated error
Conductivity PCM	k_{pcm}	-0.79%	5%	-3.94%
Convection HTF	h_{conv}	-0.13%	10%	-1.31%
Mass flow rate	$\dot{m}_{htf}$	-0.13%	0.2%	-0.026%
Specific heat capacity HTF	c_{htf}	-0.066%	5%	-0.32%
Specific heat capacity PCM	c_{pcm}	0.13%	5%	0.66%
Latent heat of fusion PCM	Δh_m	0.85%	2.5%	2.13%
Density PCM	ρ_{pcm}	0.13%	8%	1.97%
Density HTF	ρ_{pcm}	0%	5%	0%
Temperature inlet HTF	T_{in}	-	1 K	5.12%
Initial temperature PCM	T_{pcm}	-	1 K	0.26%

Sensible and latent heat is stored during the charging process (Equation 4.9). The sensible heat is a function of the PCM temperature drop and the specific heat capacity. Increasing the specific heat capacity means that more sensible heat is stored and the freezing time should increase. The freezing time is increased by 0.13%. The sensitivity of the latent heat of fusion is a factor 6.5 higher. This higher influence is expected due to the higher energy storage density of latent heat. The density of the HTF is also investigated, but it has no influence.

The sensitivity of the initial PCM temperature is low. A higher temperature means that more sensible heat is stored prior to the phase change process. It has a low influence on the freezing time since the latent energy storage density is higher as stated in previous paragraph.

Increasing the inlet temperature results in a larger temperature gradient between the HTF and the PCM. A higher heat transfer rate is accomplished and the solidification time is decreased, which was also observed for the effectiveness-NTU model (Section 4.2.2).

A constant and equal density of the PCM is assumed in both phases of the PCM. By studying the specifications (Appendix C), it can be seen that the difference between solid and liquid density is 120 kg/m^3. The difference in density between the phases could have an effect on the heat transfer process. From Table 4.5, it however can be seen that the sensitivity is low.

An estimation of the error of the enthalpy model is done by estimating the deviations of the assumed or measured parameters. The error margin of the Gnielinski correlation [51] used to calculate the convection coefficient is 10%. The accuracy of the mass flow measurements is 0.2%. Measuring errors of 5% are assumed for the PCM conductivity and specific heat capacities of the HTF and the PCM. A mean density value of 820 kg/m^3 was used for all phases. The difference between solid and liquid density (Appendix C) is however 120 kg/m^3. This results in an uncertainty of 60 kg/m^3 or 8% of the PCM density. The uncertainty of the latent heat of fusion is taken to be 2.5%, which is lower than for the previous model (Table 4.1). This smaller value is assumed due to the fact that the thermal energy storage uncertainty listed in the PCM datasheets (Appendix C) also includes sensible heat. For independent parameters (Equation 4.6), this results in a total error of 7.2%.

A increased accuracy of 3.8% is obtained compared to the effectiveness-NTU model (Section 4.2.2). The inclusion of sensible heat and the solidification range of 1 °C gives a more accurate model. The results of the enthalpy model will be discussed and validated by comparing with experimental data [50] in the next chapter.

Chapter 5

Model comparison and validation

5.1 Experimental results

Experimental measurements were performed on the thermal battery described in Chapter 3 by a previous master student [50]. The charging process was investigated for different mass flow rates. These results are used in the following sections to validate the numerical model. The trends in the experiments with the maximum mass flow rate will be discussed before performing the validation.

The temperature profiles resulting from the experiments can be seen in Figure 5.1. The HTF extracts energy from the thermal battery to charge it. This will result in a decreased PCM temperature while the HTF heats up. The heat transfer rate gets smaller further in the channels because of the smaller temperature gradient between the HTF and the PCM. The channels upstream will thus cool down more rapidly, which explains the difference in temperature between the four PCM channels. The higher temperature throughout the thermal battery at the beginning of the charging process results in the HTF temperature peak. This peak should be at the start of the measurements. There is however a starting delay on this peak. This can be appointed to a lag in the measurements, the fact that there is chilled HTF in the returning hose and that the pump does not immediately operates at full capacity. The temperature difference between inlet and outlet temperature becomes smaller while the battery cools down and has a nearly constant temperature difference. This nearly constant difference is due to the fact that the PCM is at a constant temperature during the solidification process.

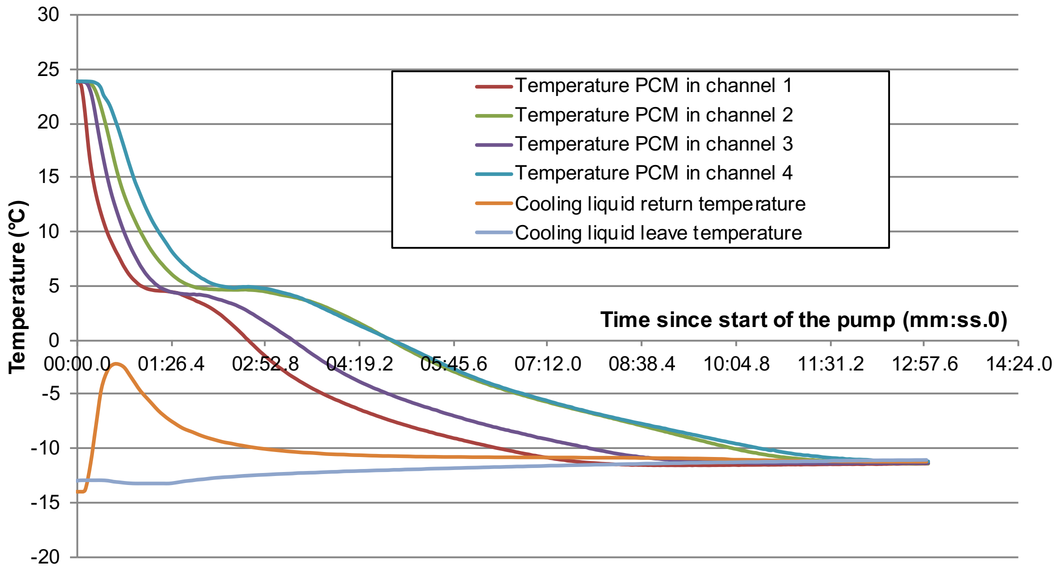

Figure 5.1: Experimental temperature profiles during the charging process of a thermal battery [50].

The state of the PCM can also be derived from Figure 5.1. The state is not the same in all the channels, but their trends are similar. At first, the liquid PCM is cooled down to the solidification temperature and sensible heat is stored. The PCM is then in a mushy state and stays approximately constant until phase change is completed. Mainly latent heat is stored since only a small temperature decrease is present. After solidification, the temperature anew starts to decrease and an extra amount of sensible heat is stored in the solid PCM. The PCM temperature reaches a final temperature which approaches the HTF temperature. The thermal battery is fully charged.

The experimental results offer a general view on the phase change process. It is however not possible to derive where the phase change front is situated in thermal battery, since only one thermowell is used per PCM channel. Solving the enthalpy model described in Section 4.3 gives the grid depicted in Figure 4.6. The temperature value of each CV determines the exact state of this CV. The location of the phase change front can be derived from this. The simulated values of this model are compared with the experimental results in the next sections.

5.2 Outlet temperature HTF

5.2.1 Model validation

The available experimental data [50] is used to validate the model. As explained in the previous section, the PCM temperature is only measured at one location in the channel and only offers a general view of the PCM temperature trend. On the other hand, the outlet temperature is measured before entering and after leaving the thermal battery. This is thus an accurate representation of the HTF temperature. The simulated outlet is thus compared with the experimental one to validate the model. Simulations with different inlet conditions are performed.

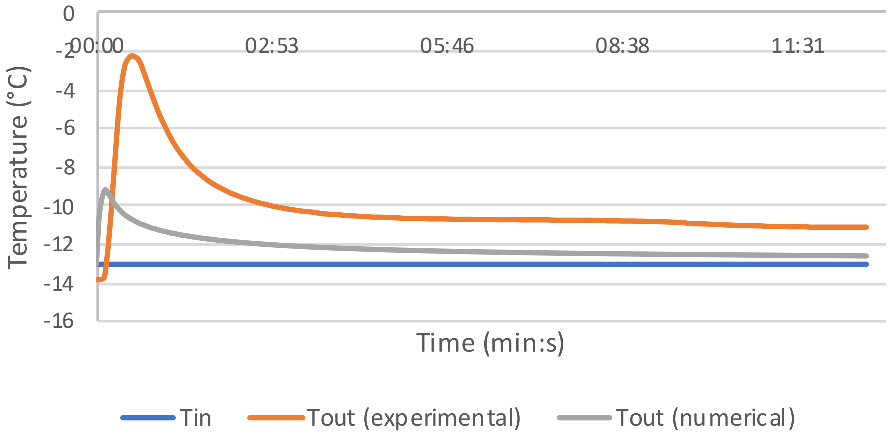

Figure 5.2: Outlet temperature HTF for constant inlet temperature HTF.

In a first step, a constant HTF inlet temperature of -13 °C is used in the simulations. The corresponding outlet temperature in function of time is plotted in Figure 5.2. The experimental results are also illustrated herein. It can be seen that a similar trend is obtained. The reasons for this trend is explained in Section 5.1. The temperature peak at the beginning of the charging process occurs immediately in the numerical temperature since no experimental errors are present. The maximum temperature of the peak is however lower. The temperature at the end of the simulation is also lower. Using a constant HTF inlet temperature does not give a correct representation of the charging process.

By having a closer look at the inlet temperature profile depicted in Figure 5.1, a temperature rise during the charging process is observed. The constant HTF inlet temperature condition imposed in the first simulation is thus not correct. The actual inlet condition will be used in a second simulation. This results in a different shape of the outlet temperature curve (Figure 5.3). The resulting temperature has approximately the same value in the starting peak. This is because the experimental inlet temperature is roughly -13 °C during the first two minutes, which is the same inlet condition as in the first simulation. It gradually rises after. This results in a higher outlet temperature. A nearly constant temperature difference between inlet and outlet is maintained since the solidification has started and the PCM temperature near the wall is approximately constant. The final temperature is higher and approximates the experimental value. The peak temperature is however still 9.12 °C lower than the experimental one.

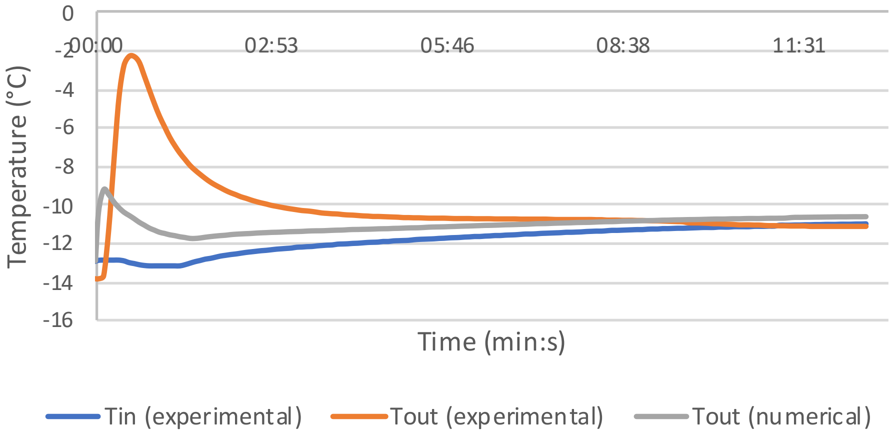

Figure 5.3: Outlet temperature HTF for varying inlet temperature HTF.

A constant HTF mass flow rate was assumed in the previous two simulations. However, the pump used in the experiments does not immediately deliver the maximum mass flow rate of 1.037 kg/s. The HTF passing through the channel has thus more time to heat up for the lower mass flow rate present at the beginning of the measurements. This variable mass flow rate is included in a third simulation and gives the results depicted in Figure 5.4. An increase of the maximum outlet temperature of 0.84 °C compared to the previous two simulations is observed. The peak is also delayed. The maximum mass flow rate is achieved after two minutes. This results in the same final temperature as the simulation with varying inlet temperature. The simulated and experimental data still do not match.

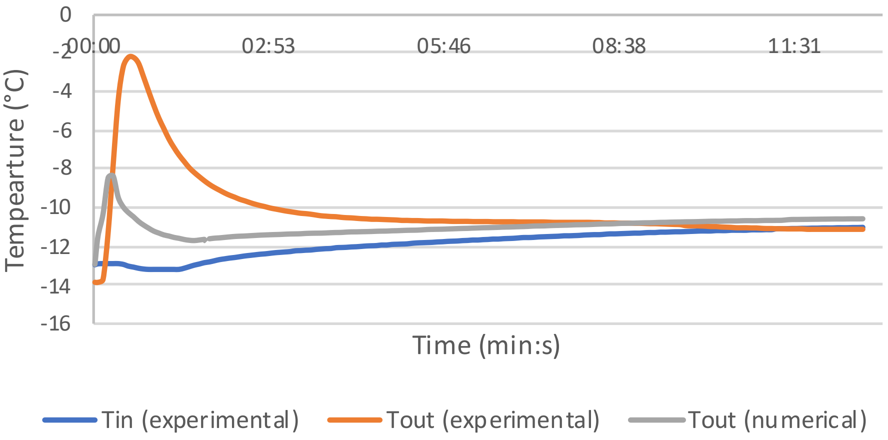

Figure 5.4: Outlet temperature HTF for varying inlet temperature HTF.

As explained in the paragraphs above, the correct inlet conditions of temperature and mass flow rate are needed to obtain a better validation of the enthalpy model. There is however still a large difference with the experimental results. A similar but less pronounced trend is observed. The difference in peak temperature is 6.13 °C. This indicates that the model is not a satisfactory representation of the charging process in the thermal battery. The remaining question is how the model can be improved to fit the data more accurately.

5.2.2 Model improvements

Sensible heat aluminium

To begin with, only the HTF and the PCM is modelled. These two materials are however enclosed in aluminium profiles. This aluminium mass is not included, although it is also cooled down during the charging process. The aluminium does not undergo a phase and no latent heat is stored. Nonetheless, there is sensible heat storage from the temperature drop in the material. The ratio of aluminium volume per total volume $\frac{V_{al}}{V_{pcm}+V_{al}}$ is 0.36. The sensible energy storage ratio $\frac{h_{sens,al}}{h_{sens,pcm}+h_{sens,al}}$ is determined using Equation 5.1. The densities ρ and specific heat capacities c listed in Table 5.1.

$$\frac{h_{sens,al}}{h_{sens,pcm}+h_{sens,al}} = \frac{V_{al}\,\rho_{al}\,c_{al}}{V_{pcm}\,\rho_{pcm}\,c_{pcm}+V_{al}\,\rho_{al}\,c_{al}} \tag{5.1}$$

Table 5.1: Thermo-physical properties and volumes used to determine sensible energy storage ratio [50].

Property	Symbol	Aluminium	PCM
Density [kg/m^3]	ρ	2700	820
Specific heat capacity [J/kgK]	c	900	2000
Volume [cm^3]	V	116.5	201.5

By substituting the values (Table 5.1), a sensible energy storage ratio of 0.46. Almost half of the sensible energy is stored in the aluminium mass which indicates a significant influence of the aluminium on the charging process. This is however only valid when the aluminium and PCM have the same temperature and no phase change occurs. The PCM undergoes a phase change. This results in a latent energy storage. The ratio of aluminium sensible energy per total stored energy $\frac{h_{al,sens}}{H_{pcm}+h_{al,sens}}$ (Equation 5.2) includes the latent heat. It is a function of volumes V specific heat capacities c, temperature differences ΔT, liquid fraction difference Δf and latent heat of fusion Δh_m.

$$\frac{h_{sens,al}}{H_{pcm}+h_{sens,al}} = \frac{V_{al}\,\rho_{al}\,c_{al}\,\Delta T_{al}}{V_{pcm}\,\rho_{pcm}(c_{pcm}\,\Delta T_{pcm}+\Delta h_m \Delta f)+V_{al}\,\rho_{al}\,c_{al}\,\Delta T_{al}} \tag{5.2}$$

To calculate this ratio an assumption about the aluminium temperature is done. The aluminium mass adjacent to the HTF has the same temperature as the first PCM CVs in the direction perpendicular to the flow. The aluminium masses at the far ends of the profiles are at the temperatures of their adjacent PCM CV. This temperature distribution assumption is illustrated in Figure 5.5.

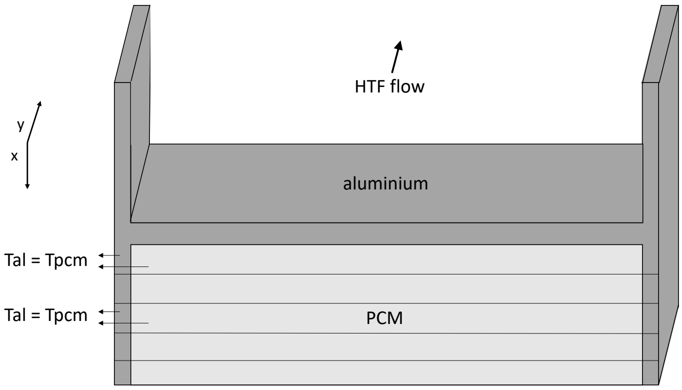

Figure 5.5: Cross-section of profile with temperature distribution in aluminium mass.

Knowledge of the aluminium temperature during the charging process makes it possible to calculate the thermal energy storage ratio $\frac{h_{al,sens}}{H_{pcm}+h_{al,sens}}$ (Figure 5.6). The value at the beginning of the cooling process is 0.82. This is as expected, since most of the aluminium mass is adjacent to the HTF and the temperature in this PCM CV is close to the solidification temperature of 6 °C. The rest of the PCM is still close to the initial temperature of 24 °C. Only sensible heat is present. With time the temperature in the whole PCM drops and solidification starts close to the HTF wall. This implicates the addition of latent heat which has a higher energy density. As a result, the ratio decreases rapidly. It converges to a fixed value of 0.18 after 14 min. The PCM is completely solidified and only extra sensible energy is stored by cooling below the low end of the solidification temperature range of 5 °C. It can thus be concluded that the sensible heat of the aluminium is not negligible during the early stages of charging, especially before solidification has started. The bends of the collectors are also not modelled and will experience the same phenomena. This sensible energy storage of the

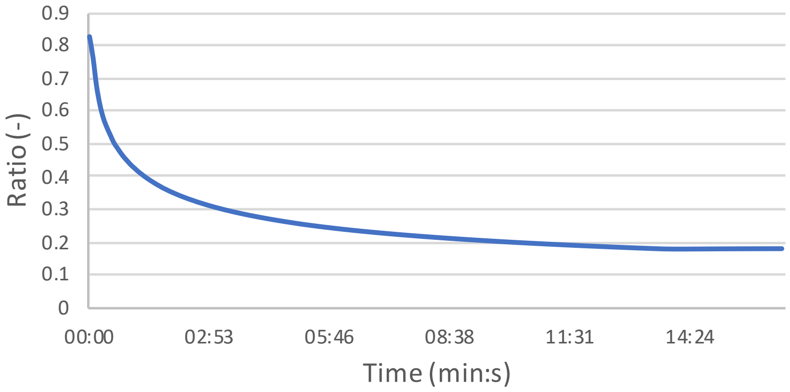

Figure 5.6: Ratio of sensible energy stored in the aluminium to the total stored energy in the aluminium and the PCM during the charging process.

neglected aluminium mass should result in a higher peak temperature of the outlet temperature, which more closely resembles the experimental results.

PCM mass

Furthermore, not all the PCM is included in the model. As explained in Chapter 3, there are six HTF and seven PCM channels. By applying the symmetry assumption on one channel, the two outermost halves of the PCM channels are not included. This results in a decrease in PCM mass of 15%. More energy needs to be extracted than modelled. The influence of the extra mass on the outlet temperature is checked by increasing the size of the PCM channels by 15%. The difference in outlet temperature is 0.02 °C. The excluded mass has thus an insignificant influence on the outlet temperature. It has however an influence on the solidification time, which increases by 30%. The solidification is increased, but extra thermal energy is stored.

Losses to the environment

Losses to the environment could also have an influence on the HTF temperature. Convective heat transfer with the aluminium walls non-adjacent to the PCM channels is also present. The thermal battery is however insulated during the charging process to prevent these heat gains from the ambient air [50]. An estimation of these losses Q_{losses} is done and compared to the heat transfer rate from the PCM to the HTF Q_{htf}. This is done by using a one-dimensional thermal network between the HTF and the ambient air. The total thermal resistance R_{tot} is calculated as a series of conductive and convective resistances with following equation.

$$R_{tot} = \frac{1}{h_{conv}A_{losses}} + \frac{d_{al}}{k_{al}A_{losses}} + \frac{d_{ins}}{k_{ins}A_{losses}} + \frac{1}{h_{amb}A_{losses}} \tag{5.3}$$

The conductive resistances of the aluminium and insulation are calculated with the material thickness d, thermal conductivity k and heat transferring area A_{losses}. A relatively high thermal conductivity of the insulation is taken to make a conservative estimation. The convective resistances are calculated with their convection coefficients h and the heat transferring area A_{losses}. The convection coefficient of the HTF is calculated as explained in Appendix A. Its value is not constant since the mass flow rate is lower at the beginning of the simulations. The natural convection coefficient of the ambient air is estimated to be 10 W/m^2. The specific values of the used parameters can be found in Table 5.2. The losses are then calculated by dividing the temperature difference between the HTF and the ambient air ΔT by R_{tot}.

$$Q_{losses} = \frac{\Delta T}{R_{tot}} \tag{5.4}$$

Table 5.2: Parameters used to determine losses to the environment during the charging process.

Property	Symbol	Aluminium	Insulation	HTF	Ambient
Thickness [mm]	d	2	50	-	-
Heat transferring area [cm^3]	A_l	36	36	36	36
Thermal conductivity [W/mK]	k	205	0.035	-	-
Convection coefficient [W/m^{2}K]	h	-	-	190-480	-

The resulting ratio of heat losses to the total heat transfer $\frac{Q_{losses}}{Q_{losses}+Q_{htf}}$ is illustrated in Figure 5.7. It has a maximum value of 2.18% at the start of the simulations. It however immediately drops to almost 0% and then steadily increases towards 0.5%. The higher value a the start of the charging process is

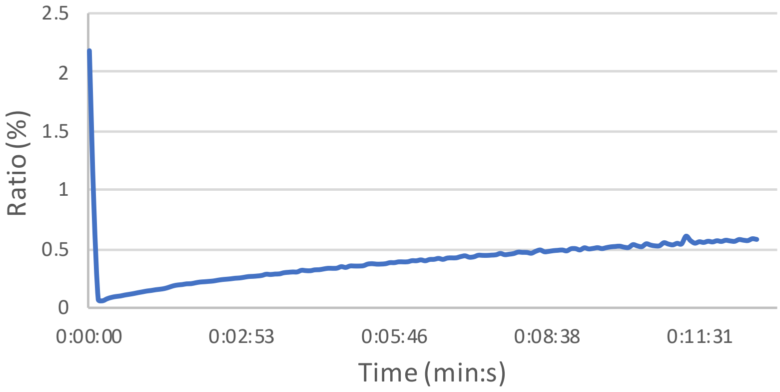

Figure 5.7: Ratio of losses to the environment to the total heat transfer from the PCM and the ambient air.

due to the low mass flow rate during the first 10 seconds. From the calculated ratio it is clear that the heat gains from the environment are very low and can be neglected. The heat losses will have no effect on the HTF outlet temperature.

HTF flow distribution

An even distribution of the mass flow over the channels is assumed in the simulations. This is however probably not the case in reality. The flow enters through a pipe and is distributed over the first collector. The mass flow rate in the middle HTF channel of the first profile would normally be higher than in the other channels. As a consequence of the bending flow in the subsequent collectors, an uneven flow distribution should also be observed in the downstream profiles. The outlet temperature of the channels with a higher mass flow rate is lower since it has less time to heat up. The opposite holds true for lower mass flow rates. Mixing then occurs in the collector bends.

An uneven mass flow distribution was incorporated in the model. This distribution is that 25% of the mass flows through the two central HTF channels, 10% through the outermost channels and 15% through the remaining two. The resulting HTF outlet temperature of the channels with the highest mass flow rate is 0.85 °C lower than for the lowest mass flow rate at the beginning of the charging process. This was expected due to the shorter time that the mass gets to heat up. The difference between an uneven and even flow distribution after mixing in the collector is however only 0.007 °C. The mixing temperature is thus independent of the flow distribution. This is due to the difference in mass entering the collectors from the channels. More low temperature HTF mixes with less high temperature HTF. This cancels the difference in outlet temperature between the channels. The flow distribution has an insignificant effect on the final outlet temperature.

A model validation was performed by comparison with experimental data [50] in this section. In a first step, three simulations with different HTF inlet temperature and mass flow rates were made. It was concluded that the actual experimental values of temperature and mass flow rates offers a better correspondence between simulations and experiments (Figure 5.2, 5.3 and 5.4). The same temperature trend is observed, but it is less pronounced in the simulations. Several model improvement possibilities were then investigated. These were the influence of sensitive heat of the aluminium profiles, the 15% excluded PCM mass, the heat losses to the environment and the flow distribution in the HTF channels. From this investigation it is concluded that only the aluminium sensible heat could have an influence on the simulated outlet temperature. It is not negligible during the early stages of charging (Figure 5.6). Including this aluminium mass in the model should result in a better resembles of the experimental measurements.

5.3 PCM temperatures

5.3.1 Model validation

The numerical results of the PCM temperatures are compared with the experimental data [50]. The enthalpy model calculates the temperatures of the PCM in the entire channel which makes it possible to, amongst other, determine the exact position of the phase change front. Only one experimental PCM temperature per PCM channels is however available. As described in Chapter 3, a thermowell is placed in the middle of the central channel of each profile to perform this measurement. The temperature at the centre of the channel is thus obtained.

The phase change front propagates from the walls to the centre during the charging process. The maximum temperature of the PCM channels is thus centrally located at the thermowell. Only half of the PCM channel is used in the enthalpy model. The simulated maximum temperature is thus located in the CVs at the end of the grid in the direction perpendicular to the HTF flow. Two other temperatures temperatures are compared with the experiments. The temperature located in the CV adjacent to the HTF, which is the minimum temperature of the PCM. The third temperature is taken in between this minimum and maximum. The location of these temperatures are illustrated in Figure 5.8.

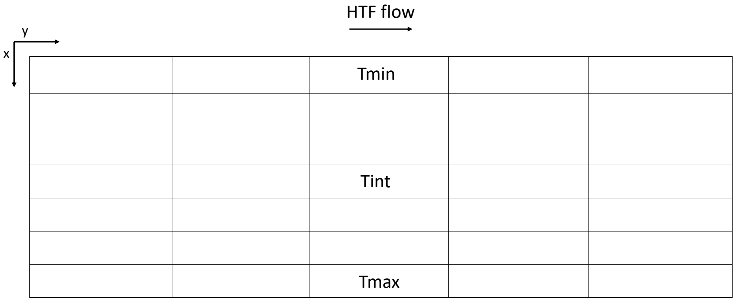

Figure 5.8: PCM temperatures of one profile on three different locations.

The numerically obtained maximum temperature should correspond with the experimental measurement, which is done at the centre of each profile. The maximum, minimum and intermediate temperatures of the first profile are compared with the corresponding experimental data in Figure 5.9. It can be seen that the maximum temperature does not correspond with the experimental results. This was not expected. The solidification starts later and has a longer duration. The intermediate temperature is a better approximation of the experiments.

A reason for the difference between simulation and experiments can be appointed to the measuring method. Aluminium thermowells are used in the experiments. Their thermal conductivity has an order of magnitude 10^3 larger than the one of the PCM. The thermowells will thus act as fins and influence the solidification

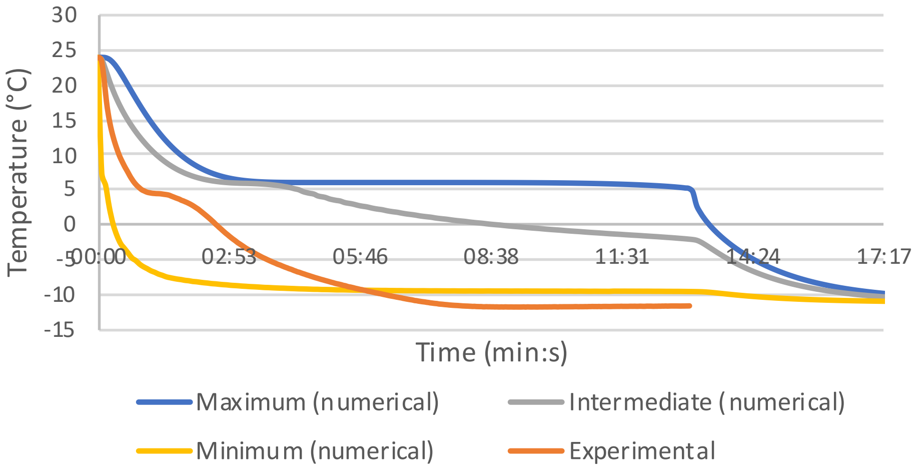

Figure 5.9: Comparison of the numerical PCM temperatures at three locations in the first profile with the experimental PCM temperature.

front. It can be expected that a solid PCM layer will form on these fins before the surrounding PCM is solidified. An approximation of this phenomenon is sketched in the cross-section in Figure 5.10a. The PCM mass adjacent to the HTF starts to solidify. The upper and lower parts of the aluminium profile will have a lower temperature than the neighbouring PCM mass, due to their higher thermal conductivity. A solid layer will build up on these extremities. The same process then occurs for the PCM at the thermowell surface. Placing thermowells in the PCM channels thus influences the charging process. As a result, the TC does not measure the maximum temperature in the PCM channel.

The assumed phase change front in the enthalpy model is sketched in Figure 5.10b. The thermowell is not included in the model. The effects of the upper and lower parts of the profile are also not included. This results in a one-dimensional phase change front propagation. The temperature will thus be lower near the HTF wall where the PCM is already solid. The maximum PCM temperature will then be located in the last CV in the direction perpendicular to the HTF flow (Figure 5.8).

It is thus not unnatural that the simulated maximum temperature does not correspond with the measured temperature. The influence of the thermowell

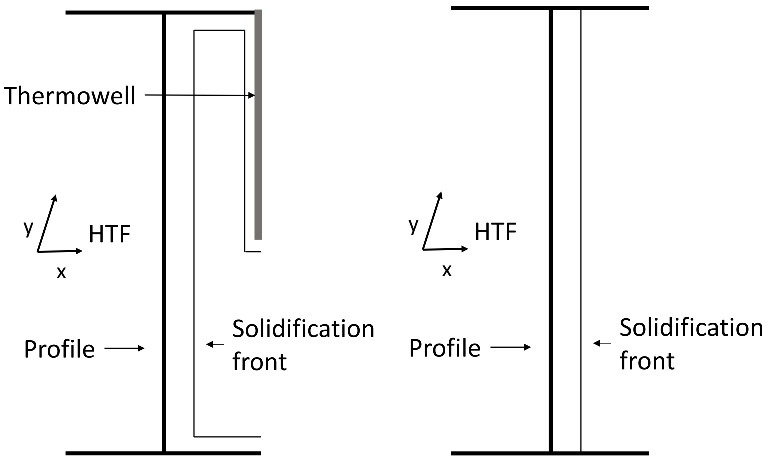

(a) Experiments. **(b)** Simulations.

Figure 5.10: Schematic of the phase change front with and without thermowell.

on the phase change front is the reason for this. The thermowell measures the temperature of a PCM layer located closer to the HTF. This explains why the intermediate temperature (Figure 5.8) more closely approaches the experiments. The solidification however still starts later and needs more time to be completed. This suggests that the measured temperature is located close to the HTF and the thermowell has a large influence on the acquired data. This faulty measurement could also mean that the thermal battery is not completely frozen, since the maximum temperature is not measured and partly explain the difference in solidification time.

It can thus be concluded that a good comparison is difficult because of two reasons. The PCM temperature is only measured at one location, while the enthalpy model calculates the entire temperature field in the channel. The second reason is that the thermowell used in the experiments affects the phase change front. A local temperature is measured which is not a good representation of the surrounding PCM. The HTF outlet temperature is a better validation parameter as explained in Section 5.2.1.

5.3.2 Phase change process

The numerically calculated PCM temperature field enables us to analyse the phase change process occurring in the thermal battery. The temperatures in the middle of a profile will first be analysed more closely. The location of the corresponding CVs are showed in Figure 5.8. This will result in a maximum, a minimum and an intermediate PCM temperature. The evolution of these three temperatures in one profile are illustrated in Figure 5.11.

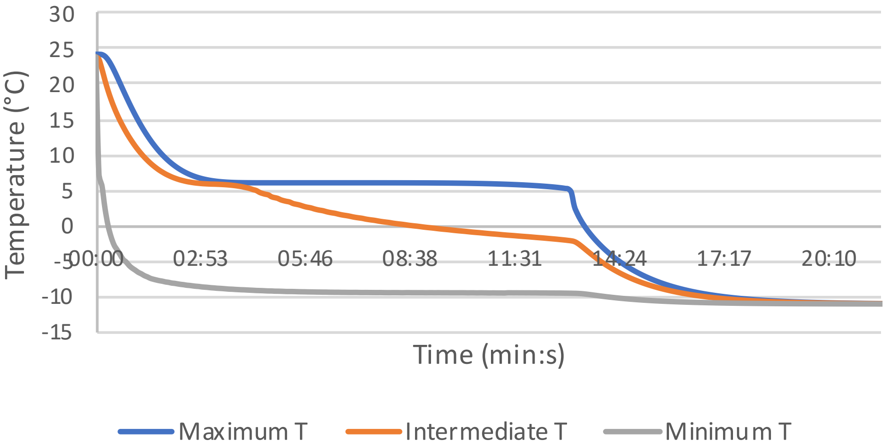

Figure 5.11: PCM temperatures of one profile on three different locations perpendicular to the HTF flow direction.

First it can be seen that the different PCM layers are at different temperatures and from their values it can be concluded in which state they are and for how long. The first layer almost immediately becomes solid and its temperature drops below the solidus temperature of 5 °C. The other two layers stay liquid for a longer period. This is as expected since the phase change front propagates away from the first layer (Figure 5.10b). The mushy zone is entered when a temperature of 6 °C is reached. This is the upper value of the solidification range. The intermediate and last layer are in the mushy state for one and eight minutes, respectively. Although the intermediate CV is located right in between the first and last one, the times needed to complete the solidification are not linearly proportional. Two mechanisms results in this non-proportionality.

First, the conductive thermal resistance of the solid PCM layer increases with time. Secondly, sensible energy is stored in the solid, when it is cooled below the solidus temperature. Energy is thus stored as sensible energy rather than latent heat in front of the phase change front. The solidification is completed after thirteen minutes.

The temperature continues to decrease after solidification. Only sensible energy is stored from now on. Sensible energy has a lower energy density compared to latent energy. This results in the faster temperature decrease, observed in Figure 5.11. The temperatures of the three layers converges towards the same value of -10.9 °C, which is close to the inlet temperature of the HTF and the battery cannot be cooled further. Continued cooling after solidification is however not necessary in practice, since the sensible heat contributes little to the total the total energy storage.

It was discussed in Section 5.1 that there is a difference in temperature evolution between the four profiles due to the heating of the HTF. The numerically calculated temperatures of the four profiles are compared with each other. The minimum and intermediate temperatures (Figure 5.8) are approximately the same in the four different profiles. The maximum temperatures deviates the most from each other and are plotted in Figure 5.12. It can be seen that the solidification starts at the same moment, which is not the case in the experiments. The completions do not occur simultaneously. The complete solidification of the last channels is however only achieved 30 seconds after the first one. This delay is larger in the experiments. This small difference in solidification time indicates that the phase change front propagates in one direction throughout the thermal battery. The HTF temperature difference calculated by the model is lower than the difference measured experimentally. Therefore, the PCM is solidified more homogeneously in the calculations. This phenomenon is explained in Section 5.2.2.

Two main conclusions can be drawn from this section. It was first discussed that an extensive comparison with the experimental data is difficult since the presence of the thermowell influences the phase change front propagation. This affects the temperature measurement that is done at one location in the PCM

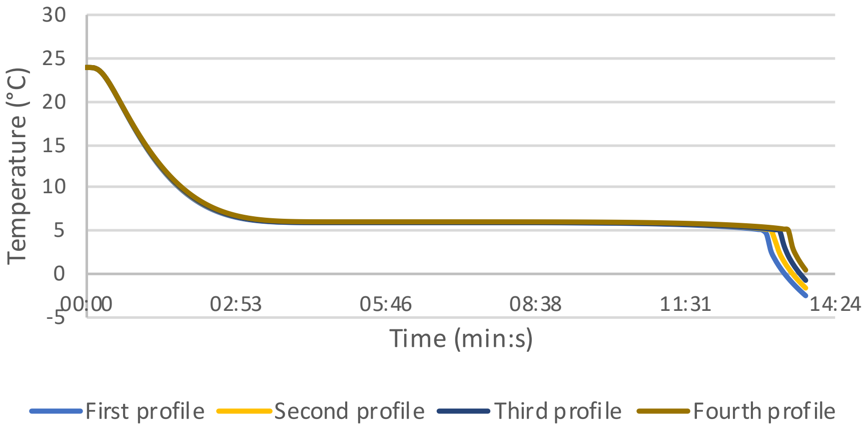

Figure 5.12: Maximum PCM temperatures of the four profiles.

channel. Secondly, the solidification occurs homogeneously throughout the thermal battery in the numerical calculations. This is appointed to the fact that the aluminium mass of the profiles is not included in the model. The sensible heat cannot be ignored in the beginning of the charging process as discussed in Section 5.2.2. Including this extra sensible heat should result in a higher temperature decrease of the HTF at the beginning of the charging process. The temperature gradient between the HTF and the PCM would be lower in the downstream profiles. The accompanied decrease in heat transfer rate would result in a longer charging process for the downstream channels, which offers better resembles with the experimental results.

5.4 Metal foam enhanced PCM

One of the conclusions of the literature survey and the sensitivity analysis done in Section 4.2.2 and 4.3.6 is that increasing the thermal conductivity of the PCM has a significant positive effect on the solidification time. A higher thermal conductivity increases the effectivity of the heat exchanger. Metal foam can be used as a thermal conductivity enhancer, due to its high thermal conductivity. Introducing an extra material in the PCM channel however decreases the PCM mass per volume. Metal foam has a high porosity and will thus have a low effect on the PCM mass per volume. Metal foam is thus considered a valid thermal conductivity enhancer. Aluminium open cell metal foam produced by Alhedron with a porosity of 93% is used.

The metal foam enhanced PCM is modelled using a one-temperature model [43]. The metal foam and PCM in each CV are considered as a homogeneous material with the same temperature. To be able to do this an effective conductivity needs to be calculated. Several correlations are discussed in Section 2.2.4. The correlation of Boomsma and Poulikakos [45] is used. This results in an effective thermal conductivity of 4.18 W/mK. The used parameters of foam and PCM are found in Table 5.3.

Table 5.3: Parameters used to calculate the effective thermal conductivity of PCM and metal foam with the correlation of Boomsma and Poulikakos [45].

Property	Symbol	Metal foam	PCM
Thermal conductivity [W/mK]	k	205	0.2
Porosity [-]	γ	0.93	-

As a first step, a numerical comparison of the solidification time with and without metal foam is done. A fixed mass flow rate and HTF inlet temperature are used in the simulations. The PCM temperatures with and without foam are plotted in Figure 5.13a and 5.13b, respectively. It can be seen that the solidification time of the metal foam enhanced PCM is two minutes. The thermal battery without foam needs twelve minutes to freeze. Introducing the metal foam decreases the solidification time by a factor six. This was expected since the thermal conductivity is 4.18 W/mK instead of 0.2 W/mK and the conductive resistance of the solid PCM is the dominant heat transfer resistance during most of the phase change.

The increased thermal conductivity also has an influence on the temperature evolution throughout the PCM, as seen in Figure 5.13a. The solidification temperature of 6 °C is reached more rapidly and almost simultaneously for all the PCM CVs. The solid layer then grows with an approximately constant propagation rate during the solidification process. This is not the case for the thermal battery without metal foam, as explained in Section 5.3. It is also clear that the

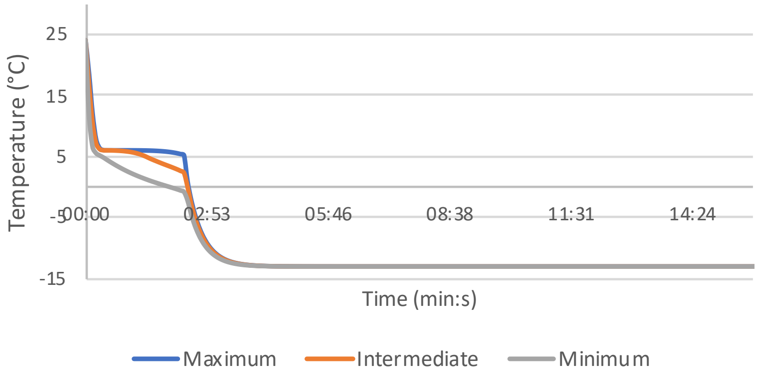

(a) Metal foam enhanced PCM.

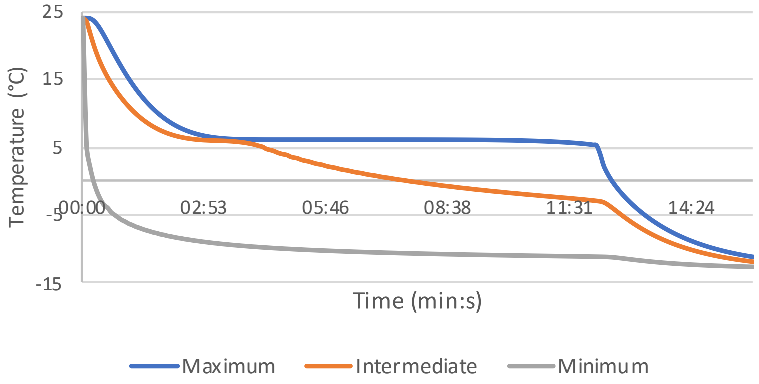

(b) PCM without metal foam.

Figure 5.13: Numerical comparison PCM temperatures with and without metal foam.

temperature differences within the metal foam enhanced PCM are smaller. The sensible energy storage in the solid PCM also occurs faster. It is clear that the thermal conductivity has a significant effect on the solidification process and the temperatures.

The simulations are compared with the experimental results, as was done for the PCM without metal foam in Section 5.2.1 and 5.3.1. The calculated HTF outlet temperatures are compared with the experimental temperatures in Figure 5.14. Approximately the same trend is observed. There is a temperature peak at the beginning of the charging process because of the higher PCM temperatures.

This peak however occurs earlier and is smaller for the simulations. The delay is appointed to the fact that there is a lag in measurements, there is chilled HTF in the returning hose and that the pump does not immediately operates at full capacity (Section 5.1). The smaller peak values are due to the exclusion of the aluminium mass in the enthalpy model. Its sensitive energy cannot be neglected during the early stages of charging. This phenomenon was explained in Section 5.2.2 for the results without foam.

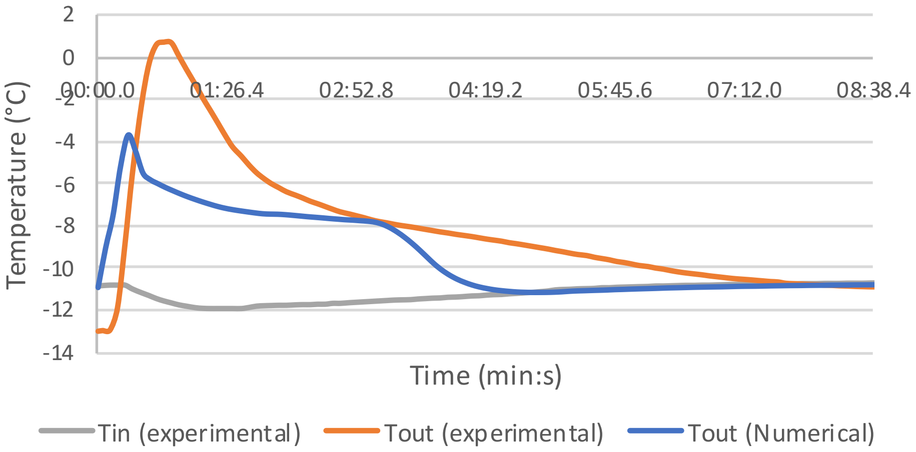

Figure 5.14: Comparison of numerical HTF outlet temperature for a metal foam enhanced PCM with experimental results.

The HTF temperature then gradually decreases as the PCM is cooled down. A plateau is present in the numerical calculations. This is because the difference between the minimum and maximum PCM temperature is small (Figure 5.13a). This is probably not the case in the experiments. From a certain point, the numerical results quickly approaches the inlet temperature. This is because the PCM is completely solidified and only extra sensible heat is stored. This effect is more pronounced in the metal foam enhanced PCM due to the higher effective thermal conductivity. This trend is however not observed in the experimental results (Figure 5.14). This indicates that the solidification process is completed earlier in the numerical results. This was not the case for the PCM without metal foam. A closer look needs to be taken at the temperatures in the PCM with metal foam.

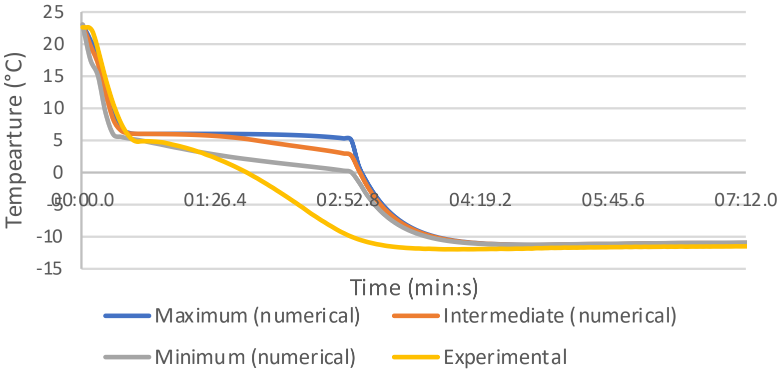

(a) First profile.

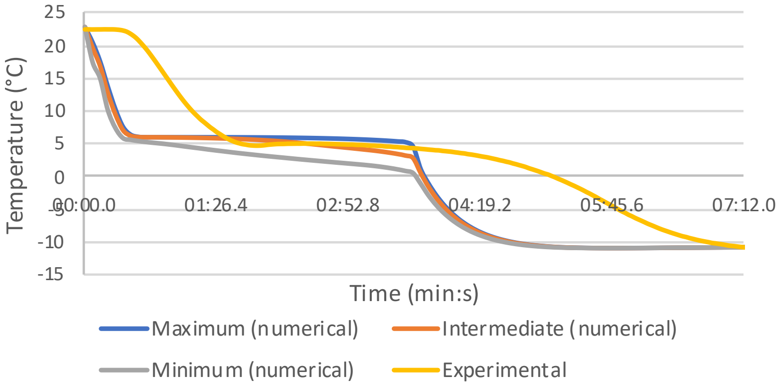

(b) Fourth profile.

Figure 5.15: Comparison of the numerical foam enhanced temperatures at three locations in the first profile with the experimental results.

The maximum, minimum and intermediate PCM temperatures are compared with the experimental results. The actual mass flow rate and HTF inlet temperature are used, since they have an effect on the phase change process, as discussed in Section 5.2.1. The results for the first and fourth profile are illustrated in Figure 5.15. From Figure 5.15a, it can be concluded that the experimental PCM is solidified more rapidly than in the numerical calculations. This is the same as for the PCM without metal foam in Section 5.3.1. If the temperature profiles of the fourth profile are analysed (Figure 5.15b), it can be seen that the simulated PCM achieves the mushy zone earlier. The aluminium is not modelled, which results in an almost homogeneous phase change front propagation in the four profiles during the simulations (Section 5.3.2). This explains the delayed initial temperature drop in the experiments. The solidification process at nearly constant temperature is approximately equal. This could mean that using an effective conductivity in a one-temperature model is a good representation of reality, if the aluminium mass is included. The HTF temperature should be closer to the experimental one and thus resulting a delayed charging process in the downstream profiles. However, the data of the first channel will probably not be fitted.

As explained in Section 5.3.1, the thermowell affects the phase change front in the PCM channel (Figure 5.10a) and results in an uncertainty on the experiments. This makes it hard to validate the models with the PCM temperatures. If a second look is taken at the outlet temperature profiles in Figure 5.14, it is clear that the metal foam enhanced PCM thermal battery is not represented correctly by the numerical calculations. The aluminium mass of the profiles is for example not included.

Another influence that is not incorporated is the thermal contact resistance between the HTF wall and the metal foam. The latter was placed in the PCM channel without bonding method. The contact between wall and foam is thus not perfect. This should result in a significant contact resistance, which lowers the heat transfer between HTF and PCM. This extra thermal contact resistance should also be included to have a better representation of the real charging process. This influence could be incorporated by adding an extra thermal resistance $R_{contact}$ in the calculation of the heat transfer rate between the HTF control volumes and the first adjacent PCM control volume (Section 4.3.1). The new Q_{htf} would then be calculated with following equation using the the PCM and HTF temperatures $T_{pcm,1}$ and T_{htf}.

$$Q_{htf} = \frac{T_{pcm,1} - T_{htf}}{R_{conv} + R_{pcm} + R_{contact}} \tag{5.5}$$

An extra contact resistance $R_{contact}$ is placed in series with the convective of the HTF R_{conv} and the conductive resistance of the PCM R_{pcm}. The heat transfer rate between HTF and PCM will thus decrease resulting in a slower charging process. This should be a better representation of the real charging process in the thermal battery.

Validation and comparison of the one-temperature model used to simulate the metal foam enhanced PCM leads to two proposed model improvements. The aluminium mass of the profiles should be included since its sensible heat cannot be neglected in the early stages of charging (Section 5.2.2). The contact resistance between HTF wall and the metal foam should also incorporated by adding an extra thermal resistance $R_{contact}$.

Chapter 6

Conclusions

The main subject of this master dissertation was to model the charging process in a cold storage with metal foam enhanced phase change material. Two thermal batteries [50] were modelled. One battery battery had metal foam placed inside the PCM container and a second one had only a PCM.

In a first model, only the latent heat of the PCM was modelled (Section 4.2). This was done by deriving a model similar to the Stefan problem [18]. The heat transfer rate between the HTF and the PCM was calculated by using the effectiveness-NTU model of heat exchangers (Appendix B). The charging process is simplified in this model. Only the phase change process at a fixed temperature is modelled. The main conclusion of this model is that the conduction in the solid PCM is the dominant heat transfer mode . It was also concluded that its dominance increases during the solidification due to the growing distance to the phase change front (Figure 4.2).

A second model was then implemented which incorporates the sensible heat and the solidification range of the PCM. This was done with the help of the enthalpy model [26]. The liquid fraction update in the solidification range, which is the most crucial part of the model was done with the method of Voller and Swaminathan [32].

The results of the model were discussed by comparing them with experimental data [50]. The battery without metal foam was first compared. It was concluded the sensible heat of the aluminium profiles has a significant effect during the early stages of charging, especially before solidification (Section 5.2.2). Including this aluminium sensible heat should offer a better resemblance with the experimental results.

The metal foam enhanced PCM was simulated with a one-temperature model [43]. A local thermal equilibrium is assumed between the PCM and the metal foam. An effective thermal conductivity can then be calculated with the correlation of Boomsma and Poulikakos [45]. This increased thermal conductivity resulted in a decreased charging time from twelve to two minutes. The metal foam enhanced PCM thus comes with an increased effectivity of the thermal battery.

The experiments on the metal foam enhanced PCM however show a lower improvement than predicted by the model (Figure 5.15). The lower performance can be attributed to the fact that the metal foam pieces were placed in the PCM channels without the use of a bonding method. A thermal contact resistance will thus be present between the container wall and the metal foam. This extra thermal resistance should be included to have a better representation of the real charging process.

Two main model improvements are proposed for future work. As a first, the aluminium profiles should be included in the modelled geometry to incorporate its sensitive heat. Secondly, the thermal contact resistance between the container wall and the metal foam should be added for the metal foam enhanced PCM.

Bibliography

[1] Improving cold storage equipment in europe - intelligent energy europe - european commission. `https://ec.europa.eu/energy/intelligent/projects/en/projects/ice-e#results`. Accessed: 2018-05-20.

[2] SA Tassou, G De-Lille, and YT Ge. Food transport refrigeration–approaches to reduce energy consumption and environmental impacts of road transport. *Applied Thermal Engineering*, 29(8-9):1467–1477, 2009.

[3] George A Lane. *Solar heat storage: latent heat materials.* CRC Press, Boco Raton, FL, 1983.

[4] H. Mehling and L.F. Cabeza. *Heat and Cold Storage with PCM. An Up to Date Introduction into Basics and Applications.* Springers-Verlag, Berlin Heidelberg, 2008.

[5] Atul Sharma, V.V. Tyagi, C.R. Chen, and D. Buddhi. Review on thermal energy storage with phase change materials and applications. *Renewable and Sustainable Energy Reviews*, 13(2):318 – 345, 2009.

[6] A. Abhat. Low temperature latent heat thermal energy storage: Heat storage materials. *Solar Energy*, 30(4):313 – 332, 1983.

[7] K.K. Pillai and B.J. Brinkworth. The storage of low grade thermal energy using phase change materials. *Applied Energy*, 2(3):205 – 216, 1976.

[8] Ahmet Sari. Eutectic mixtures of some fatty acids for low temperature solar heating applications: Thermal properties and thermal reliability. *Applied Thermal Engineering*, 25(14):2100 – 2107, 2005.

[9] L.F. Cabeza, A. Castell, C. Barreneche, A. de Gracia, and A.I. Fernández. Materials used as pcm in thermal energy storage in buildings: A review. *Renewable and Sustainable Energy Reviews*, 15(3):1675 – 1695, 2011.

[10] Mohammed M Farid, Amar M Khudhair, Siddique Ali K Razack, and Said Al-Hallaj. A review on phase change energy storage: materials and applications. *Energy Conversion and Management*, 45(9):1597 – 1615, 2004.

[11] Hee W Ryu, Sung W Woo, Byung C Shin, and Sang D Kim. Prevention of supercooling and stabilization of inorganic salt hydrates as latent heat storage materials. *Solar Energy Materials and Solar Cells*, 27(2):161 – 172, 1992. Special Issue on Heat Storage Materials.

[12] S.M. Hasnain. Review on sustainable thermal energy storage technologies, part i: heat storage materials and techniques. *Energy Conversion and Management*, 39(11):1127 – 1138, 1998.

[13] S. Jegadheeswaran and Sanjay D. Pohekar. Performance enhancement in latent heat thermal storage system: A review. *Renewable and Sustainable Energy Reviews*, 13(9):2225 – 2244, 2009.

[14] Francis Agyenim, Philip Eames, and Mervyn Smyth. Experimental study on the melting and solidification behaviour of a medium temperature phase change storage material (erythritol) system augmented with fins to power a libr/h2o absorption cooling system. *Renewable Energy*, 36(1):108 – 117, 2011.

[15] Koichi Nakaso, Hirofumi Teshima, Akito Yoshimura, Seiichi Nogami, Yuichi Hamada, and Jun Fukai. Extension of heat transfer area using carbon fiber cloths in latent heat thermal energy storage tanks. *Chemical Engineering and Processing: Process Intensification*, 47(5):879 – 885, 2008.

[16] Jianqing Chen, Donghui Yang, Jinghua Jiang, Aibin Ma, and Dan Song. Research progress of phase change materials (pcms) embedded with metal foam (a review). *Procedia Materials Science*, 4(Supplement C):389 – 394, 2014. 8th International Conference on Porous Metals and Metallic Foams.

[17] Shuli Liu, Yongcai Li, and Yaqin Zhang. Mathematical solutions and numerical models employed for the investigations of pcms phase transformations. *Renewable and Sustainable energy reviews*, 33:659–674, 2014.

[18] Jožef Stefan. Uber einige probleme der theorie der warmeletung. *Sitzer. Wien. Akad. Math. Naturw.*, 98:473–484, 1889.

[19] Yvan Dutil, Daniel R Rousse, Nizar Ben Salah, Stéphane Lassue, and Laurent Zalewski. A review on phase-change materials: mathematical modeling and simulations. *Renewable and sustainable Energy reviews*, 15(1):112–130, 2011.

[20] Wikipedia contributors. Ntu method — wikipedia, the free encyclopedia, 2017. [Online; accessed 3-January-2018].

[21] M. Belusko, E. Halawa, and F. Bruno. Characterising pcm thermal storage systems using the effectiveness-ntu approach. *International Journal of Heat and Mass Transfer*, 55(13):3359 – 3365, 2012.

[22] Ahmet Sari and Kamil Kaygusuz. Thermal performance of palmitic acid as a phase change energy storage material. *Energy Conversion and Management*, 43(6):863 – 876, 2002.

[23] N.H.S. Tay, M. Belusko, and F. Bruno. An effectiveness-ntu technique for characterising tube-in-tank phase change thermal energy storage systems. *Applied Energy*, 91(1):309 – 319, 2012.

[24] E. Halawa and W. Saman. Thermal performance analysis of a phase change thermal storage unit for space heating. *Renewable Energy*, 36(1):259 – 264, 2011.

[25] M.W. Browne and P.K. Bansal. An elemental ntu-? model for vapour-compression liquid chillers. *International Journal of Refrigeration*, 24(7):612 – 627, 2001.

[26] VR Voller, CR Swaminathan, and Brian G Thomas. Fixed grid techniques for phase change problems: a review. *International Journal for Numerical Methods in Engineering*, 30(4):875–898, 1990.

[27] Pierre Tittelein, Stéphane Gibout, Erwin Franquet, Kevyn Johannes, Laurent Zalewski, Frédéric Kuznik, Jean-Pierre Dumas, Stéphane Lassue, Jean-Pierre Bédécarrats, and Damien David. Simulation of the thermal and energy behaviour of a composite material containing encapsulated-pcm: Influence of the thermodynamical modelling. *Applied Energy*, 140:269 – 274, 2015.

[28] Abduljalil A. Al-Abidi, Sohif Mat, K. Sopian, M.Y. Sulaiman, and Abdulrahman Th Mohammad. Numerical study of pcm solidification in a triplex tube heat exchanger with internal and external fins. *International Journal of Heat and Mass Transfer*, 61:684 – 695, 2013.

[29] Saeed Tiari, Songgang Qiu, and Mahboobe Mahdavi. Numerical study of finned heat pipe-assisted thermal energy storage system with high temperature phase change material. *Energy Conversion and Management*, 89:833 – 842, 2015.

[30] Sohif Mat, Abduljalil A. Al-Abidi, K. Sopian, M.Y. Sulaiman, and Abdulrahman Th Mohammad. Enhance heat transfer for pcm melting in triplex tube with internal–external fins. *Energy Conversion and Management*, 74:223 – 236, 2013.

[31] Selvan Bellan, José Gonzalez-Aguilar, Manuel Romero, Muhammad M. Rahman, D. Yogi Goswami, Elias K. Stefanakos, and David Couling. Numerical analysis of charging and discharging performance of a thermal energy storage system with encapsulated phase change material. *Applied Thermal Engineering*, 71(1):481 – 500, 2014.

[32] VR Voller and CR Swaminathan. General source-based method for solidification phase change. *Numerical Heat Transfer, Part B Fundamentals*, 19(2):175–189, 1991.

[33] Piia Lamberg, Reijo Lehtiniemi, and Anna-Maria Henell. Numerical and experimental investigation of melting and freezing processes in phase change material storage. *International Journal of Thermal Sciences*, 43(3):277 – 287, 2004.

[34] Patrick Brousseau and Marcel Lacroix. Numerical simulation of a multilayer latent heat thermal energy storage system. *International Journal of Energy Research*, 22(1):1–15, 1998.

[35] Hamid Ait Adine and Hamid El Qarnia. Numerical analysis of the thermal behaviour of a shell-and-tube heat storage unit using phase change materials. *Applied Mathematical Modelling*, 33(4):2132 – 2144, 2009.

[36] Wei-Wei Wang, Kun Zhang, Liang-Bi Wang, and Ya-Ling He. Numerical study of the heat charging and discharging characteristics of a shell-and-tube phase change heat storage unit. *Applied Thermal Engineering*, 58(1):542 – 553, 2013.

[37] M. Lacroix. Numerical simulation of a shell-and-tube latent heat thermal energy storage unit. *Solar Energy*, 50(4):357 – 367, 1993.

[38] Mohammed M Farid and Atsushi Kanzawa. Thermal performance of a heat storage module using pcms with different melting temperatures: mathematical modeling. *Journal of solar energy engineering*, 111(2):152–157, 1989.

[39] Y.B. Tao and Y.L. He. Numerical study on thermal energy storage performance of phase change material under non-steady-state inlet boundary. *Applied Energy*, 88(11):4172 – 4179, 2011.

[40] Hamid El Qarnia. Numerical analysis of a coupled solar collector latent heat storage unit using various phase change materials for heating the water. *Energy Conversion and Management*, 50(2):247 – 254, 2009.

[41] P. Lamberg and K. Sirén. Analytical model for melting in a semi-infinite pcm storage with an internal fin. *Heat and Mass Transfer*, 39(2):167–176, Jan 2003.

[42] P.G. Kroeger and S. Ostrach. The solution of a two-dimensional freezing problem including convection effects in the liquid region. *International Journal of Heat and Mass Transfer*, 17(10):1191 – 1207, 1974.

[43] Xin Hu and Soumya S. Patnaik. Modeling phase change material in microfoam under constant temperature condition. *International Journal of Heat and Mass Transfer*, 68(Supplement C):677 – 682, 2014.

[44] R. C. Progelhof, J. L. Throne, and R. R. Ruetsch. Methods for predicting the thermal conductivity of composite systems: A review. *Polymer Engineering & Science*, 16(9):615 – 625, 1976.

[45] K. Boomsma and D. Poulikakos. On the effective thermal conductivity of a three-dimensionally structured fluid-saturated metal foam. *International Journal of Heat and Mass Transfer*, 44(4):827 – 836, 2001.

[46] Y. Tian and C.Y. Zhao. A numerical investigation of heat transfer in phase change materials (pcms) embedded in porous metals. *Energy*, 36(9):5539 – 5546, 2011.

[47] P. Zhang, Z.N. Meng, H. Zhu, Y.L. Wang, and S.P. Peng. Melting heat transfer characteristics of a composite phase change material fabricated by paraffin and metal foam. *Applied Energy*, 185:1971 – 1983, 2017. Clean, Efficient and Affordable Energy for a Sustainable Future.

[48] Shankar Krishnan, Jayathi Y. Murthy, and Suresh V. Garimella. A two-temperature model for solid-liquid phase change in metal foams. *Journal of Heat Transfer*, 127(9):995, 2005.

[49] Noriaki Wakao and Seiichirō Kagei. *Heat and mass transfer in packed beds*, volume 1. Taylor & Francis, 1982.

[50] Michiel Corryn. Charging and discharging behavior of a thermal storage for passive cold chain transport based on phase change material enhanced with metal foam. Master's thesis, Ghent University, June 2017.

[51] V. Gnielinski. On heat transfer in tubes. *International Journal of Heat and Mass Transfer*, 63:134 – 140, 2013.

[52] S. V. Patankar. *Numerical heat transfer and fluid flow.* Hemisphere Publishing Corp., Washington, DC, 1980.

Appendix A

Calculation of the convection coefficient

The heat transfer fluid extracts energy from the PCM during the charging process through convective heat transfer with the PCM container wall. First the type of HTF flow occurring in the channel is determined by calculating the Reynolds number Re. It is calculated by using following equation.

$$Re = \frac{\rho_{htf} v D_h}{\mu_{htf}} \tag{A.1}$$

The density ρ_{htf} and the dynamic viscosity μ_{htf} of the HTF can be found in appendix C. The speed v of the fluid in one channel is calculated using the mass flow $\dot{m}$, the number of channels n_{htf}, the height h_{htf} and the width w_{htf} of the channel.

$$v = \frac{\dot{m}}{\rho_{htf}\, h_{htf}\, w_{htf}\, n_{htf}} \tag{A.2}$$

The characteristic length D_h of the channels is determined by the heat exchanging area A and the wetted perimeter P.

$$D_h = \frac{4A}{P} = \frac{4\, h_{htf}\, w_{htf}}{2\,(h_{htf} + w_{htf})} \tag{A.3}$$

The mass flow rate of the cooling liquid is not constant with time. The maximum mass flow rate is 1.037 kg/s. This leads to a maximum of the Reynolds number of

1126 which indicates a laminar flow in the HTF channels for all mass flow rates. The Nusselt number Nu is then calculated with the correlation of Gnielinski [51] for a constant temperature (no influence of free convection).

$$Nu_{m,T} = \{Nu_{m,T,1}^3 + 0.7^3 + [Nu_{m,T,2} - 0.7]^3 + Nu_{m,T,3}^3\}^{1/3} \tag{A.4a}$$

$$Nu_{m,T,1} = 3.66 \tag{A.4b}$$

$$1.615\sqrt[3]{Re\,Pr\,D_h/L} \tag{A.4c}$$

$$Nu_{m,T,3} = \left(\frac{2}{1+22Pr}\right)^{1/6} (Re\,Pr\,D_h/L_{htf})^{1/2} \tag{A.4d}$$

The Prandtl number Pr is a function of the dynamic viscosity μ_{htf}, the specific heat capacity c_{htf} and thermal conductivity k_{htf}.

$$Pr = \frac{\mu_{htf}\, c_{htf}}{k_{htf}} \tag{A.5}$$

The convection coefficient h_{conv} can then be calculated with the Nusselt number Nu, the thermal conductivity of the HTF k_{htf} and the characteristic length D_h of the channel.

$$h_{conv} = \frac{Nu\, k_{htf}}{D_h} \tag{A.6}$$

The thermo-physical properties of the HTF (Temper -30) are assumed independent of temperature and thus constant. They are evaluated at -10 °C and the values can be found in Table A.1. The geometrical dimensions of the HTF channels are also found in Table A.1.

Table A.1: Thermo-physical properties of the HTF and dimensions of the channel used to calculate the convection coefficient.

Property	Symbol	Value
Specific heat [kJ/kgK]	c_{htf}	3.04
Density liquid [kg/m^3]	ρ_{htf}	1187
Dynamic viscosity [mPas]	μ_{htf}	6.14
Thermal conductivity [W/mK]	k_{htf}	0.45
Length channels [mm]	L	806
Height channels [mm]	h_{htf}	50
Width HTF channels [mm]	w_{htf}	8.3

Appendix B

Effectiveness-NTU method

The effectiveness-NTU method is used to calculate the heat transfer in heat exchangers. A thermal battery can be modelled as a heat exchanger with the PCM acting as a fixed heat source at its phase change temperature T_{pcm}. The ratio of the actual heat transfer q to the maximum theoretical one q_{max} is called the effectiveness ε of the heat exchanger. The transfer rates are assumed constant in the heat exchanger. It is a performance parameter of the heat exchanger.

$$\varepsilon = \frac{q}{q_{max}} \tag{B.1}$$

The maximum heat transfer rate q_{max} occurs for the maximum temperature difference between the inlet and outlet of the thermal battery. This is the case when the outlet temperature T_{out} is equal to the phase change temperature T_{pcm}. q_{max} is calculated with following equation.

$$q_{max} = \frac{\dot{m}_{htf}}{2} c_{htf} (T_{in} - T_{pcm}) \tag{B.2}$$

It is a function of the maximum temperature difference, the mass flow trough one HTF channel $\dot{m}_{htf}$ and the specific heat capacity of the HTF. The factor 1/2 stems from the symmetry assumption explained in Section 4.1.

The effectiveness can also be calculated with the number of transfer units NTU between the HTF and the phase change front. A simplified correlation can be used when the ratio of heat capacity rates C_{max}/C_{min} is infinite. The heat capacity rates is the mass flow rate $\dot{m}$ multiplied by the specific heat capacity c. This results in following equation.

$$\varepsilon = 1 - e^{NTU} \tag{B.3}$$

The NTU is determined by the mass flow rate $\dot{m}_{htf}$, the specific heat capacity and the total thermal resistance between the HTF and the phase change front. This gives following equation which is time dependent due to the moving phase change front.

$$NTU = \frac{1}{R_{tot}\frac{\dot{m}_{htf}}{2}c_{htf}} \tag{B.4}$$

Under the assumption of a constant specific heat capacity, the effectiveness is expressed with following equations.

$$\varepsilon = \frac{T_{in} - T_{out}}{T_{in} - T_{pcm}} \tag{B.5}$$

This offers the possibility to calculate the outlet temperature T_{out} of the thermal battery.

Appendix C

Datasheets

The technical specifications of the PCM (RT5HC by Rubitherm) and the HTF (Temper -30 by Climalife) are listed hereunder.

Data sheet

RT5HC

RUBITHERM® RT is a pure PCM, this heat storage material utilising the processes of phase change between solid and liquid (melting and congealing) to store and release large quantities of thermal energy at nearly constant temperature. The RUBITHERM® phase change materials (PCM's) provide a very effective means for storing heat and cold, even when limited volumes and low differences in operating temperature are applicable.

We look forward to discussing your particular questions, needs and interests with you.

Properties:
- high thermal energy storage capacity
- heat storage and release take place at relatively constant temperatures
- no supercooling effect, chemically inert
- long life product, with stable performance through the phase change cycles
- melting temperature range between -4 °C and 100 °C

The most important data:

	Typical Values	
Melting area	**5-6** main peak: 6	**[°C]**
Congealing area	**6-5** main peak: 5	**[°C]**
Heat storage capacity ± 7,5%	**250**	**[kJ/kg]***
Combination of latent and sensible heat in a temperatur range of -2 °C to 13 °C.	**70**	**[Wh/kg]***
Specific heat capacity	**2**	**[kJ/kg·K]**
Density solid at -15°C	**0,88**	**[kg/l]**
Density liquid at 20 °C	**0,76**	**[kg/l]**
Heat conductivity (both phases)	**0,2**	**[W/(m·K)]**
Volume expansion	**13**	**[%]**
Flash point	**115**	**[°C]**
Max. operation temperature	**30**	**[°C]**

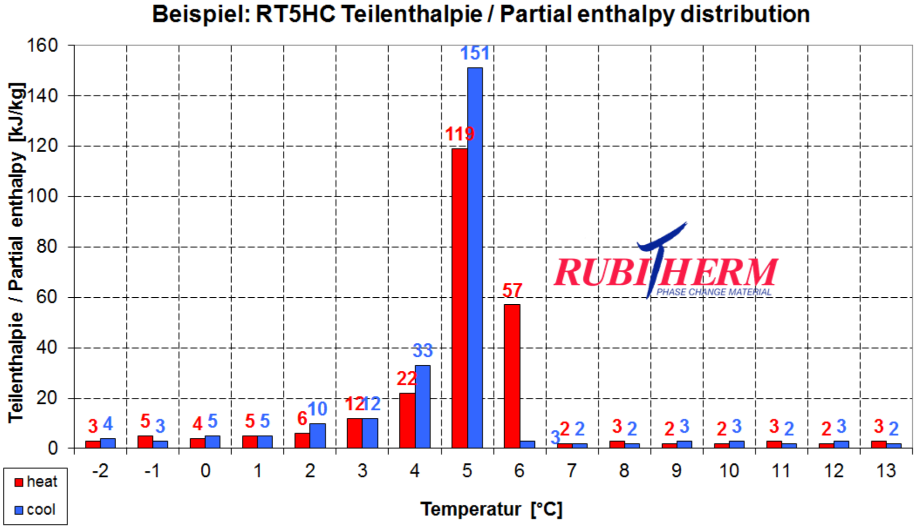

**Measured with 3-layer-calorimeter.*

Rubitherm Technologies GmbH
Sperenberger Str. 5a
D-12277 Berlin
Tel: +49 30 720004-62
Fax: +49 30 720004-99
E-Mail: info@rubitherm.com
Internet: www.rubitherm.com

The product information given is a non-binding planning aid, subject to technical changes without notice. Version: 31.05.2016

Ref. : CA.24 /05.14/V5/ EN

TEMPER®

Non-contractual photo.

TEMPER® is a ready-to-use heat transfer fluid based on Potassium acetate and potassium formate in a water solution. It is non-toxic and non-polluting and contains innovative corrosion inhibitors to protect the system.

TEMPER® may be used as heat transfer fluid in both static and mobile installations.

At low temperatures, it is an advantageous alternative to glycol mixtures in indirect systems (secondary circuits).

It may be used in various applications for refrigeration, freezing, the food industry, large distribution (supermarkets), ice rinks, artificial snow slopes, pharmaceutical industry and shipping.

It may also be used as a heat transfer fluid at higher temperature in air conditioning systems, heating pumps, solar or heat recovery installations.

TEMPER® is a ready-to-use solution and should not be diluted.

Colourless liquid (lightly yellowish), **TEMPER®** contains neither amines nor nitrates.

Available in 5 versions (mixtures) where the description indicates the freezing point :

TEMPER® –10 °C
TEMPER® –20 °C
TEMPER® –30 °C

TEMPER® –40 °C
TEMPER® –55 °C

At its freezing point, **TEMPER®** becomes granular, but does not lead to an increase in volume. The effect of volume variation is therefore kept to a strict minimum.

TEMPER® has increased thermal capacity and is characterised by excellent thermal conductivity in comparison with products with a propylene glycol base.

The viscosity is lower than glycols, which is advantageous for pump and pipe sizing. The investment costs for the installation and running the system are therefore lower.

TEMPER® has good biodegradable characteristics and is neither flammable or explosive.

In sealed packaging and closed systems, **TEMPER®** is stable and, in principle, its shelf life is unlimited.

The special additives present in **TEMPER®** ensure optimum corrosion protection and lubricating properties.

PHYSICAL PROPERTIES OF TEMPER®

1.1. Main Specifications

Specifications	TEMPER® –10	TEMPER® –20	TEMPER® –30	TEMPER® –40	TEMPER® –55
Appearance	Lightly yellow liquid				
Boiling point (°C)	109				
pH at 20°C	8,5 ± 0,5				
Freezing point (°C)	-10	-20	-30	-40	-55
Density at 20°C (kg/dm^3)	1.079–1.092	1.138–1.146	1.173–1.183	1.204–1.213	1.239–1.242
Dynamic viscosity at 20°C (mPa.s)	1.45	1.80	2.10	2.71	2.96
Kinematic viscosity at 20°C (mm^2/s)	1.33	1.58	1.79	2.24	2.39
Mass heat at 20°C (kJ/(kg.K))	3.57	3.31	3.12	3.01	2.88
Thermal conductivity at 20°C (w/(m.K))	0.54	0.51	0.49	0.47	0.45

1.2. Tables of Properties

Volume mass (kg/m^3)

TEMPER®	-10	-20	-30	-40	-55
Temperature (°C)					
- 55	FROST ZONE				1269
- 50					1268
- 40				1227	1266
- 30			1192	1225	1262
- 20		1151	1190	1222	1259
- 10	1092	1149	1187	1218	1254
0	1090	1147	1184	1215	1250
10	1088	1145	1181	1211	1245
20	1086	1142	1177	1207	1240
30	1084	1139	1174	1203	1235

* library data

Mass Heat (kJ/(kg.K))

TEMPER®	-10	-20	-30	-40	-55
Temperature (°C)					
- 55	FROST ZONE				2.64
- 50					2.66
- 40				2.83	2.71
- 30			2.96	2.88	2.75
- 20		3.20	3.00	2.92	2.78
- 10	3.52	3.23	3.04	2.95	2.81
0	3.54	3.26	3.08	2.98	2.84
10	3.56	3.29	3.10	3.00	2.86
20	3.58	3.32	3.12	3.01	2.88
30	3.59	3.34	3.14	3.01	2.88

* library data

Kinematic Viscosity (cSt)

TEMPER®	-10	-20	-30	-40	-55
Temperature (°C)					
- 55	FROST ZONE				290.47
- 50					158.87
- 40				41.99	54.47
- 30			14.53	19.56	23.63
- 20		7.05	8.49	10.37	12.75
- 10	3.77	4.48	5.17	6.27	7.87
0	2.57	2.97	3.34	4.20	5.18
10	1.79	2.09	2.34	3.01	3.50
20	1.33	1.58	1.79	2.24	2.39
30	1.07	1.28	1.48	1.70	1.64

* library data

Dynamic Viscosity (mPa.s)

TEMPER®	-10	-20	-30	-40	-55
Temperature (°C)					
- 55	FROST ZONE				368.63
- 50					201.47
- 40				51.53	68.94
- 30			17.32	23.96	29.84
- 20		8.11	10.10	12.67	16.05
- 10	4.12	5.14	6.14	7.64	9.88
0	2.80	3.41	3.96	5.1	6.48
10	1.95	2.40	2.76	3.65	4.36
20	1.45	1.80	2.10	2.71	2.96
30	1.16	1.46	1.74	2.05	2.02

* library data

Thermal Conductivity (W/(m.K))

TEMPER®	-10	-20	-30	-40	-55
Temperature (°C)	FROST ZONE				
- 55					0.38
- 50					0.39
- 40				0.40	0.39
- 30			0.42	0.41	0.40
- 20		0.45	0.44	0.42	0.41
- 10	0.50	0.47	0.45	0.43	0.42
0	0.51	0.48	0.46	0.44	0.43
10	0.53	0.49	0.47	0.45	0.44
20	0.54	0.51	0.49	0.47	0.45
30	0.56	0.52	0.50	0.48	0.46

* library data

1.3. Corrosion protection of TEMPER®

Galvanic corrosion arises because of differences of electric potential between metals in the circuit. The traditional heat transfer fluid corrosion inhibitors form a uniform mechanical film on the inside of all components which provides protection against corrosion (figure 1).

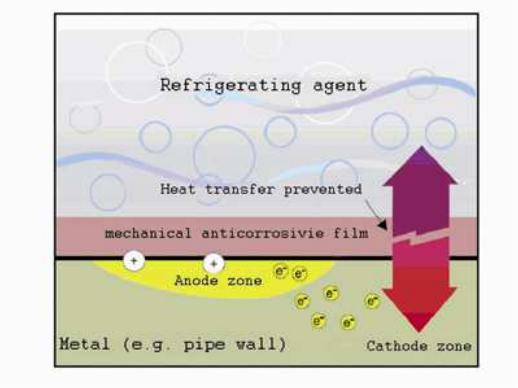

Figure 1

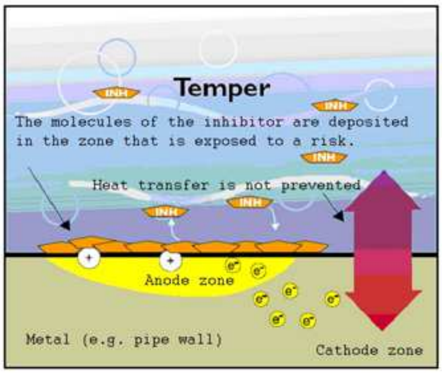

Figure 2

Temper® contains special corrosion inhibitors which do not form a general protective film, but act only where there are differences in electrical potential.

The molecules of the inhibitors are only deposited in the areas where there is a risk of corrosion, and form an extremely thin layer which makes practically no difference to the thermal transfer.

For this reason the corrosion inhibitors of **Temper®** do not tend to wear out.

Once the corrosion risk is blocked and compensated, the molecules of the inhibitors are free in the **Temper®** and can once again be deposited in other places where there is a difference in electricity potential (see figure 2).

2. RECOMMENDATIONS FOR USE AND APPLYING TEMPER®

2.1. Cleaning the installation and application

It is strongly recommended to clean the installation thoroughly before filling with **Temper®.**

If there are deposits, and especially of metal oxides, we recommend cleaning with Dispersant D.

It should be done in the following manner:

- circulate water in the system for 1 to 2 hours, then drain the installation quickly and fully to the lowest point.

- prepare and add "Dispersant D*" solution at 20 g/litre of water in the installation

- let the product circulate for at least 2 hours and then drain the installation quickly to the lowest point;

- carefully and adequately rinse with water until it is clear and the pH is approximately 7 (± 0.5).

- The system must then be dried quickly (by emptying or with nitrogen) and then filled from the lowest point.

Depending on the state of the circuit, it may be necessary to clean several times.

It is important to drain and carefully rinse with water after every time it has been cleaned.

Please note: If there are deposits on the installation and it is seriously oxidised with scale, it is advisable to first treat the circulation with a solution of "Desoxydant P*" at approximately 100 g/l of water at 50°C for 2 hours.

After it has been emptied, follow the treatment with "Dispersant D*" in the abovementioned manner.

In principle, a current installation containing other heat transfer fluids may be switched to **Temper®**.

One generally achieves a net power increase, thanks to the improved properties of the Temper® thermal transfer.

Before changing to **Temper®**, it is essential to check the compatibility of the pumps, valves, materials and accessories of the installation and change where necessary.

The system must then be treated with a cleaning product strong enough to eliminate the old corrosion inhibitors and then flushed with neutral pH distilled water.

The sieves and filters (recommended mesh 0.6-0.8 mm) must be cleaned/replaced.

Temper® may then be put into the installation to be used again.

2.2. Principles of use

Temper® should only be used in sealed systems under pressure.

If it is used in an open system, evaporation will lead to a change of the composition/concentration of Temper®, which will lead to the solution thickening, as well as crystallisation and oxidisation of metal parts.

An air purger system must be installed in the system.

Materials / Valves

Commonly used materials, such as copper, brass, stainless steel, cast iron and plastic materials, (ABS, PE) approved for the planned temperatures, may be used with **Temper®**.

It must not be used with galvanised steel, zinc or metal with soft solder.

Filters

Use filters with mesh of 0.6 to 0.8 mm for optimum filtration.

Pumps

Inform the pump manufacturer that you have chosen **Temper®** as the heat transfer fluid. Choose the approved materials for the seals and pump housing.

If there is a leak of **Temper®** on the seals, it is essential to clean the surfaces on which the **Temper®** has been spilt with water as quickly as possible and to remove all traces of it.

It is possible to use pumps without seals.

Seal materials /gaskets

On flange connections, it is advisable to use EPDM rubber that can withstand the temperatures of the application.

On traditional threaded connections, it is possible to use a paste called Uni-Pack or Locher type. Please ask your supplier for more details.

Fibre joints or gaskets, hemp joints, Teflon and Viton may not be used with **Temper®**.

Isolation

It is advisable not to insulate flanges and connections to be able to control possible leaks linked to metal expansion.

***** *The data stated in paragraph 1 of this document are merely indicative and do not constitute a sales specification.***

Appendix D

Python code

This appendix contains the Python code of the implemented models. These include the effectiveness-NTU and enthalpy approach of the phase change process occurring in the thermal battery.

D.1 Effectiveness-NTU model

```
# -*- coding: utf-8 -*-
"""
modelling of thermal battery with effectiveness-NTU method

@author: André Paulsen
"""
from math import exp
from scipy.integrate import ode
'''Thermo-physical and geometrical properties'''
pcm = {'cp': 2000.,
       'k': 0.2,
       'rho_solid': 880.,
       'rho_liquid': 760.,
       'T_in': 5.5,
       'latent_heat': 220.0*1000}
htf = {'cp': 3040.,
       'k': 0.45,
       'rho_liquid': 1187.,
       'mhu': 6.14/1000,
       'T_in': -13}
channel = {'h': 50.0/1000,
           'w_pcm': 10.0/1000,
           'w_htf': 8.3/1000,
           'L': 806.0/1000,
           'num_htf': 6,
           'm': 1.3,
           'num_part': 1,
           'num_profiles': 4}
channel['A_total'] = channel['h'] * channel['L']
channel['A'] = channel['h'] * channel['L'] / channel['num_part']
# calculation Re, Pr, Nu (ON 1 FULL CHANNEL)


def u(m, rho, h, w, num):
    return m / (rho * h * w * num)


u = u(channel['m'], htf['rho_liquid'], channel['h'], channel['w_htf'],
      channel['num_htf'])
D_h = 4 * channel['h'] * channel['w_htf'] / (2 * channel['h'])
Re = htf['rho_liquid'] * u * D_h / htf['mhu']
Pr = htf['mhu'] * htf['cp'] / htf['k']


def Nu_lam_T(Re, Pr, d, L):
    Nu1 = 3.66
    Nu2 = 1.615 * (Re * Pr * d/L)**(1/3)
    Nu3 = (2 / (1 + 22*Pr))**(1/6) * (Re * Pr * d/L)**(1/2)
    return (Nu1**3 + 0.7**3 + (Nu2 - 0.7)**3 + Nu3**3)**(1/3)
```

```
def Nu_lam_Q(Re, Pr, d, L):
    Nu1 = 4.354
    Nu2 = 1.953 * (Re * Pr * d/L)**(1/3)
    Nu3 = 0.924 * (Pr)**(1/3) * (Re * d/L)**(1/2)
    return (Nu1**3 + 0.6**3 + (Nu2 - 0.6)**3 + Nu3**3)**(1/3)


def h_lam(Nu, k, d):
    return Nu * k / d


Nu_lam = Nu_lam_T(Re, Pr, D_h, channel['L'])
h_lami = Nu_lam * htf['k'] / D_h

m_channel = channel['m']/channel['num_htf']  # mass flow per channel
m_symm = m_channel/2  # to apply symmetry assumption


def R_tot(h, d):
    '''Definition total thermal resistance'''
    return d / (pcm['k'] * channel['A']) + 1 / (h * channel['A'])


def ntu(R, m, cp):
    '''Definition NTU'''
    return 1/(R * m * cp)


def eff(ntu):
    '''Definition effectiveness with infinite c_p,pcm'''
    return 1 - exp(-ntu)


def Tout(Tin, eff):
    '''Definition outlet temperature HTF'''
    return Tin - eff * (Tin - pcm['T_in'])


'''Calculation of dpcm, Q and Tout with constant time step with ODE solver'''


def dd_dt(t, d):
    R = R_tot(h_lami, d)
    NTU = ntu(R, m_symm, htf['cp'])
    effectiveness = eff(NTU)
    Q_max = m_symm * htf['cp'] * (pcm['T_in'] - Tin)
    Q = effectiveness * Q_max
    return Q / (pcm['latent_heat'] * pcm['rho_liquid'] * channel['A'])
```

```
d = ode(dd_dt).set_integrator('vode', method='bdf')

steps_max = 10000  # maximum number of steps
for j in range(0, channel['num_profiles']):
    '''calculate the 4 different profiles'''
    for i in range(0, channel['num_part']):
        '''calculate d_pcm and Tout for 1 part of channel untill completelly
        frozen then move on to next part untill end of the channel'''
        t0, d0, dt = 0., 0., .1
        d.set_initial_value([d0], t0)
        t, d_pcm = [], []
        T_out = []  # values are resetted
        t.append(t0), d_pcm.append(d0)
        k = 1  # reset time counter
        if i == 0 and j == 0:
            '''calculation of first part channel '''
            Tin = htf['T_in']
            T_out.append(Tout(
                    Tin, eff(ntu(R_tot(h_lami, d0), m_symm, htf['cp']))))
            while d.successful() and d_pcm[k-1] <= channel['w_pcm']/2 \
                    and k < steps_max:
                d.integrate(d.t+dt)
                t.append(d.t)
                d_pcm.append(d.y[0])
                T_out.append(Tout(Tin, eff(
                        ntu(R_tot(h_lami, d_pcm[k]), m_symm, htf['cp']))))
                k += 1

            Tin_next = []
            for T in T_out:
                Tin_next.append(T)
        else:
            '''calculation of all the other parts of the channel'''
            Tin = Tin_next[0]
            T_out.append(
                    Tout(Tin, eff(ntu(R_tot(h_lami, d0), m_symm, htf['cp']))))
            while d.successful() and d_pcm[k-1] <= channel['w_pcm']/2 \
                    and k < steps_max:
                if k < len(Tin_next):
                    Tin = Tin_next[k]
                else:
                    Tin = Tin_next[-1]
                d.integrate(d.t+dt)
                t.append(d.t)
                d_pcm.append(d.y[0])
                T_out.append(Tout(Tin, eff(
                        ntu(R_tot(h_lami, d_pcm[k]), m_symm, htf['cp']))))
                k += 1
```

```
            Tin_next = []
            for T in T_out:
                Tin_next.append(T)

        if j == channel['num_profiles'] - 1:
            T_out2 = []
            ii = 0
            for T in T_out:
                if (ii * dt) % 5 == 0:
                    T_out2.append(T_out[ii])
                ii += 1

'''calculation freezing time and final T_out'''
t_freezing_s = max(t)
t_freezing_min = t_freezing_s / 60
T_final = T_out[-1]
R_conv = R_tot(h_lami, 0)
R_pcm = []
iii = 0
for d in d_pcm:
    if (iii * dt) % 5 == 0:
        R_pcm.append(R_tot(h_lami, d_pcm[iii]))
    iii += 1
```

D.2 Enthalpy model

```
#!/usr/bin/env python3
# -*- coding: utf-8 -*-
"""
modelling of thermal battery with enthalpy method

@author: André Paulsen
"""
import numpy as np
import math

with open('T_in_temper_foam_70.csv', encoding='utf_8') as T_in:
    #  reader = csv.reader(Tin)
    T_temper = []
    for row in T_in:
        T_temper.append(float(row))

with open('massflow_foam.csv', encoding='utf_8') as m_in:
    #  reader = csv.reader(Tin)
    m_tot = []
    for row in m_in:
        m_tot.append(float(row))

'''THERMO-PHYSICAL AND GEOMETRICAL PROPERTIES'''
pcm = {'cp': 2000.,  # both phases
       'k': 4.18,  # both phases, boomsma (4.18)
       'rho_s': 880.,
       'rho_l': 760.,
       'rho_m': (880 + 760)/2,  # 'both' phases
       'latent_heat': 220*1000,  # 250-15*2 (sensible weg), J/kg
       'T_s': 5. + 273.15,  # K
       'T_l': 6. + 273.15,
       'T_initial': 22.87 + 273.15,  # foam: 22.87
       'f_initial': 1
       }
htf = {'cp': 3040.,
       'k': 0.45,
       'rho_l': 1187.,
       'mu': 6.14/1000,  # all at -10°C
       'T_in': 273.15 - 13
       }
channel = {'h': 50./1000,
           'w_pcm': 10./1000,
           'w_htf': 8.3/1000,
           'w_alu': 2./1000,
           'L': 806.0/1000,
           'k_alu': 205.,
           'num_htf': 6,  # number of HTF channels
           'm': 1.037,  # mass flow all channels
           'time_step': .5,  # dt in seconds
           'num_cv': 10,  # number of CV in axial direction
```

```
           'num_cv_pcm': 50,  # number of CV PCM
           'num_profiles': 4  # number of profiles
           }
channel['A_tot'] = channel['h'] * channel['L']  # surface 1 complete channel
channel['A'] = channel['A_tot'] / channel['num_cv']  # surface 1 control volume
channel['A_flow'] = channel['h'] * channel['w_htf']
channel['v'] = channel['m'] / (htf['rho_l'] * channel['A_flow']) \
               / channel['num_htf']
channel['m_symm'] = channel['m'] / channel['num_htf'] / 2
channel['m_htf'] = channel['m'] / channel['num_htf']
htf['Pr'] = htf['cp'] * htf['mu'] / htf['k']
channel['D_h'] = 2 * channel['w_htf'] * channel['h'] /\
               (channel['w_htf'] + channel['h'])
htf['Re'] = htf['rho_l'] * channel['v'] * channel['D_h'] / htf['mu']

'''FUNCTIONS'''


def F(T):
    '''linear function of liquid fraction f(T)
        , with under- and overshoot'''
    if T < pcm['T_s']:
        return 0
    elif T > pcm['T_l']:
        return 1
    else:
        return (T-pcm['T_s']) / (pcm['T_l']-pcm['T_s'])


def dF_dT(T):
    '''derivative of liquid fraction function'''
    if T < pcm['T_s']:
        return 0
    elif T > pcm['T_l']:
        return 0
    else:
        return 1 / (pcm['T_l']-pcm['T_s'])


def dF_dT_f(f):
    '''derivative liquid fraction function evaluated for f'''
    if f <= 0:
        return 0
    elif f >= 1:
        return 0
    else:
        return 1 / (pcm['T_l']-pcm['T_s'])


def F_inv(f):
```

```
    '''inverse function of liquid fraction'''
    if f < 0:
        return pcm['T_s']
    elif f > 1:
        return pcm['T_l']
    else:
        return f * (pcm['T_l']-pcm['T_s']) + pcm['T_s']


def dH(T):
    '''difference solid and liquid enthalpies (H_l - H_s)
        now constant because of constant thermo-physical properties'''
    return pcm['rho_l'] * pcm['latent_heat']


def S_p(T_m, f_m, Vp):
    '''linear term source term (S = S_p*T + S_c)
       dF_dT is evaluated at iteration level m
       dx is volume associated with the control volume'''
    dF = dF_dT_f(f_m)
    return -dH(T_m) * dF * Vp


def S_c(f_old, f_m, T_m, V_p):
    '''constant term source term (S = S_p*T + S_c)
       dF_dT and F_inv are evaluated at iteration level m
       T_m alleen maar nodig voor dH, maar toch constant nu'''
    dH_p = dH(T_m)
    dF = dF_dT_f(f_m)
    return ((dH_p * (f_old - f_m) * V_p) +
            (dH_p * dF * F_inv(f_m) * V_p)
            )


def Nu_lam_T(Re, Pr, d, L):
    Nu1 = 3.66
    Nu2 = 1.615 * (Re * Pr * d/L)**(1/3)
    Nu3 = (2 / (1 + 22*Pr))**(1/6) * (Re * Pr * d/L)**(1/2)
    return (Nu1**3 + 0.7**3 + (Nu2 - 0.7)**3 + Nu3**3)**(1/3)


def h_lam(Nu, k, d):
    return Nu * k / d


def a_nb():
    '''discretisation coefficient of neighbour point T_nb'''
    return (pcm['k'] * dy * channel['h']) / dx
```

```
def b_p(rho):
    '''discretisation coefficient of old value PCM: T^old'''
    return rho * pcm['cp'] * dx * dy * channel['h'] / dt


def a_p(rho):
    '''discretisation coefficient of node point T_p'''
    return 2 * a_nb() + b_p(rho)


def b_phtf():
    V_htf = channel['w_htf']/2 * channel['h'] * dy
    return V_htf * htf['rho_l'] * htf['cp'] / dt


def a_nbhtf():
    return channel['m_htf']/2 * htf['cp']


def a_nbpcm():
    '''discretisation coefficient first PCM CV neighbour
        Q = (T_pcm - T_htf)/(R_pcm + R_conv +(R_alu))'''
    A_R = dy * channel['h']
    R_pcm = dx/(2 * pcm['k'] * A_R)
    R_conv = 1/(h_conv * A_R)
    R_alu = 0
    # R_alu = channel['w_alu']/(channel['k_alu'] * A_R)
    return (R_pcm + R_conv + R_alu) ** (-1)


def a_phtf():
    return b_phtf() + a_nbhtf() + a_nbpcm()


def a_p1(rho):
    return b_p(rho) + a_nb() + a_nbpcm()


def TDMAsolver(a, b, c, d):
    '''method to solve tridiagonal system of equations'''
    # b: diag, a: upper diag, c: lower diag, d: right hand side
    nf = len(d)  # number of equations
    ac, bc, cc, dc = map(np.array, (a, b, c, d))  # copy arrays
    for it in range(1, nf):
        mc = ac[it-1]/bc[it-1]
        bc[it] = bc[it] - mc*cc[it-1]
        dc[it] = dc[it] - mc*dc[it-1]

    xc = bc
    xc[-1] = dc[-1]/bc[-1]
```

```
    for il in range(nf-2, -1, -1):
        xc[il] = (dc[il]-cc[il]*xc[il+1])/bc[il]

    return xc


'''START OF CALCULATIONS'''
'''time and space steps'''
n = channel['num_cv_pcm'] + 1  # extra CV of T_htf
o = channel['num_cv'] * channel['num_profiles']
dx = (channel['w_pcm']/2) / (channel['num_cv_pcm'])
dy = channel['L'] / channel['num_cv']
dt = channel['time_step']
Vp = dx * dy * channel['h'] / dt
t = 0  # start time steps HIER NU AANGEPAST
tt = 1500
Vpcm = dx * dy * channel['h']
Vhtf = channel['w_htf']/2 * dy * channel['h']

'''Setting the initial values and boudary conditions'''
T_old_prov = np.ones((n, o)) * pcm['T_initial']
T_old_prov[0] = T_temper[0]  # HTF temperature all at -15°C
T_old = T_old_prov.transpose()
f_old = pcm['f_initial'] * np.ones((o, n))  # completely liquid
f_old[0] = 1  # HTF completely liquid all the time

'''Storing matrices: spatial'''
T_store = np.zeros((o, n))
f_store = np.zeros((o, n))
phase = np.zeros((o, n))

'''Temperature of sensor'''
middle = math.floor(channel['num_cv']/2)
middle_pcm = math.floor(channel['num_cv_pcm']/2)

T_out2 = [T_temper[0] - 273.15]
T_1min = [pcm['T_initial'] - 273.15]
T_1_1op4 = [pcm['T_initial'] - 273.15]
T_1mid = [pcm['T_initial'] - 273.15]
T_1_3op4 = [pcm['T_initial'] - 273.15]
T_1max = [pcm['T_initial'] - 273.15]
T_2min = [pcm['T_initial'] - 273.15]
T_2mid = [pcm['T_initial'] - 273.15]
T_2max = [pcm['T_initial'] - 273.15]
T_3min = [pcm['T_initial'] - 273.15]
T_3mid = [pcm['T_initial'] - 273.15]
T_3max = [pcm['T_initial'] - 273.15]
T_4min = [pcm['T_initial'] - 273.15]
T_4mid = [pcm['T_initial'] - 273.15]
```

```
T_4max = [pcm['T_initial'] - 273.15]
T_out = [T_temper[0] - 273.15]  # temperature for returning temper
T_incheck = []
m_incheck = []
h_convcheck = []

'''start time loop'''
frozen = 1
state = 10
# while frozen > 0:
# while state > 1:
for t in range(0, int(tt/channel['time_step'])):
    dHhtfdt = 0
    dHpcmdt = 0
    dHtotdt = 0
    if (t*channel['time_step']) % 5 == 0 and (t * channel['time_step']) / 5\
            < len(m_tot):
        channel['m'] = m_tot[int(t*channel['time_step']/5)]
        channel['v'] = channel['m'] / (htf['rho_l'] * channel['A_flow']) \
            / channel['num_htf']
        channel['m_symm'] = channel['m'] / channel['num_htf'] / 2
        channel['m_htf'] = channel['m'] / channel['num_htf']
        htf['Re'] = htf['rho_l'] * channel['v'] * channel['D_h'] / htf['mu']
        '''calculation convection coefficient'''
        Nu = Nu_lam_T(htf['Re'], htf['Pr'], channel['D_h'], channel['L'])
        h_conv = h_lam(Nu, htf['k'], channel['D_h'])  # def voor direct in fct
    m_incheck.append(channel['m_htf'])
    h_convcheck.append(h_conv)

    '''start y-direction loop'''
    for j in range(0, o):
        error_f = 100
        error_f_rel = 100
        error_T = 100
        error_T_rel = 100
        i = 0  # number of iterations per time step (i <= m+1)

        '''temperature of upstream HTF CV (T_htf_i-1)'''
        if j == 0:
            if (t*channel['time_step']) % 5 == 0:
                if (t * channel['time_step']) / 5 < len(T_temper):
                    Tin = T_temper[int(t*channel['time_step']/5)]
                else:
                    Tin = T_temper[-1]
            T_htf_prev = Tin
            T_incheck.append(T_htf_prev)
        else:
            T_htf_prev = T_old[j-1][0]  # eerste kolom, j-1 rij

        '''start x-direction loop'''
```

```
while error_f > 10 ** (-4) or error_T_rel > 10 ** (-4):

    dF = np.zeros(n)
    Sp = np.zeros(n)
    Sc = np.zeros(n)

    if i == 0:  # iteration level 0 (start iteration)
        '''FIRST STEP: start by setting f0 = fold'''
        f_m = f_old[j]
        T_m = T_old[j]  # only to calculate dF/dT, Sp and Sc
    else:
        T_m = T_m1
        f_m = f_m1
    '''SECOND STEP: solving system of equations'''
    ''' calculate dF/dT, Sp and Sc (evaluated at previous time step'''

    for k in range(1, n):
        dF[k] = dF_dT_f(f_m[k])
        Sp[k] = S_p(T_m[k], f_m[k], Vp)
        Sc[k] = S_c(f_old[j][k], f_m[k], T_m[k], Vp)

    '''construction of matrices: a, b, c and d'''
    '''left hand side'''
    # diagonal: ap constant, Sp not constant
    ap = np.ones(n) * a_p(pcm['rho_m'])
    ap[0] = a_phtf()
    ap[1] = a_p1(pcm['rho_m'])
    ap[-1] -= a_nb()  # symmetry BC (b_p + a_nb)
    b = ap - Sp
    # upper diagonal
    a = -a_nb() * np.ones(n-1)
    a[0] = -a_nbpcm()  # DUS DIE NIEUWE TERM
    # lower diagonal
    c = -a_nb() * np.ones(n-1)
    c[0] = -a_nbpcm()
    '''right hand side'''
    # b_p * T_old + Sc
    d = np.ones(n) * b_p(pcm['rho_m'])
    for k in range(1, n):
        d[k] = d[k] * T_old[j][k] + Sc[k]

    d[0] = b_phtf()*T_old[j][0] + a_nbhtf()*T_htf_prev

    '''SOLVING TDMA'''
    T_m1 = TDMAsolver(a, b, c, d)  # solution next iteration level

    error_T = np.amax(np.absolute(T_m - T_m1))
    error_T_rel = np.amax(np.absolute((T_m-T_m1)/T_m))

    '''LIQUID FRACTION UPDATE: fm1 = fm + dF/dT(Tm1 - Finv(fm))'''
```

```
        f_m1 = np.ones(n)  # resetting f_m1
        for k in range(1, n):
            if f_m[k] == 1:
                A = 1  # linear term
                unrelax = 0.75  # underrelaxation
                delta = (ap[k] * (T_m1[k] - F_inv(f_m[k])) /
                         (dx * dH(T_m1[k]) + ap[k] * A)
                         )  # F^(-1)(f=1) = T_l (uit definitie)
                f_m1[k] = f_m[k] + unrelax * delta
            else:
                f_m1[k] = f_m[k] + dF[k] * \
                        (T_m1[k] - F_inv(f_m[k]))
            # overshoot/undershoot correction
            if f_m1[k] > 1:
                f_m1[k] = 1
            elif f_m1[k] < 0:
                f_m1[k] = 0

        error_f = np.amax(np.absolute(f_m1 - f_m))

        i += 1  # step counter

        '''end of while loop'''
    '''Conservation of energy'''
    for eee in range(0, n):
        if eee == 0:
            dHtotdt += Vhtf*htf['rho_l']*htf['cp'] * (T_m1[eee] -
                                                  T_old[j][eee]) / dt
        else:
            dHtotdt += Vpcm * (pcm['rho_m'] *
                               pcm['cp'] * (T_m1[eee] - T_old[j][eee]) +
                               pcm['rho_l'] * pcm['latent_heat'] *
                               (f_m1[eee] - f_old[j][eee])
                               ) / dt

    T_old[j] = T_m1  # convergence: T_old, f_old stored for next time step
    f_old[j] = f_m1

    for e in range(0, n):
        T_store[j][e] = T_old[j][e]
        f_store[j][e] = f_old[j][e]

    '''end x-direction loop'''

'''end of y-direction loop = 1 time step'''

state = np.absolute(T_store[-1][0] - T_store[-1][-1])
frozen = np.amax(np.delete(f_store.transpose(), 0, 0))
if frozen == 0:
    t_freezing = t * channel['time_step']
```

```
    t += 1
    T_out.append(T_store[-1][0] - 273.15)

    '''Temperature sensors'''

    if (t * channel['time_step']) % 5 == 0:
        T_out2.append(T_store[-1][0] - 273.15)
        T_1min.append(T_store[middle][1] - 273.15)
        T_1_1op4.append(T_store[middle][5] - 273.15)
        T_1mid.append(T_store[middle][middle_pcm] - 273.15)
        T_1_3op4.append(T_store[middle][15] - 273.15)
        T_1max.append(T_store[middle][-1] - 273.15)
        T_2min.append(T_store[middle + channel['num_cv']][1] - 273.15)
        T_2mid.append(T_store[middle + channel['num_cv']][middle_pcm]
                    - 273.15)
        T_2max.append(T_store[middle + channel['num_cv']][-1] - 273.15)
        T_3min.append(T_store[middle + 2*channel['num_cv']][1] - 273.15)
        T_3mid.append(T_store[middle + 2*channel['num_cv']][middle_pcm]
                    - 273.15)
        T_3max.append(T_store[middle + 2*channel['num_cv']][-1] - 273.15)
        T_4min.append(T_store[middle + 3*channel['num_cv']][1] - 273.15)
        T_4mid.append(T_store[middle + 3*channel['num_cv']][middle_pcm]
                    - 273.15)
        T_4max.append(T_store[middle + 3*channel['num_cv']][-1] - 273.15)

'''end of time loop (all time steps)'''

dEdt = channel['m_htf']/2 * htf['cp'] * (T_incheck[-1] - (T_out[-1] + 273.15))
E_cons_tot = dEdt - dHtotdt

results = {'T_final (°C)': T_store.transpose(),
           'f (-)': f_store.transpose(),
           'T_max (°C)': np.amax(T_store),
           'T_min (°C)': np.amin(T_store),
           'T_return (°C)': T_out,
           'T1min (°C)': T_1min,
           'T1mid (°C)': T_1mid,
           'T1max (°C)': T_1max,
           'T2min (°C)': T_2min,
           'T2mid (°C)': T_2mid,
           'T2max (°C)': T_2max,
           'T3min (°C)': T_3min,
           'T3mid (°C)': T_3mid,
           'T3max (°C)': T_3max,
           'T4min (°C)': T_4min,
           'T4mid (°C)': T_4mid,
           'T4max (°C)': T_4max,
           'Tout': T_out2
           }
```